Array Signal Processing for Accurate Medical Ultrasound Measurements

by

Shigeaki Okumura

Contents

List of Tables

List of Figures

Acknowledgments

This thesis and related works from Toru Sato Laboratory, Graduate School of Informatics, Kyoto University, could not have been possible without the kind support and help of many people, whom I would like to deeply acknowledge here.

First, I would like to express my gratitude to Professor Toru Sato, my supervisor, for his kind advice, continuous support, and consistent guidance. It would have been impossible to accomplish this work without his outstanding insight, constructive suggestions, and extensive knowledge. I am highly honored to be able to learn the professional awareness of an engineer and scientist from him.

I would like to express my sincere appreciation to Dr. Hirofumi Taki. He is currently CEO of MaRI Co. Ltd. and part-time lecturer at Tohoku University. He invited me to the medical ultrasound field. He gave me appropriate advice, fruitful suggestions, and kind encouragement. I am honored to be able to study under him. I could never have finished this work without his support and instruction. I believe that his start-up company, MaRI Co. Ltd, will be successful in becoming a great company that supports all people who have sleeping issues.

I am deeply thankful to the committee members of this thesis, Professors Tetsuya Matsuda and Mamoru Yamamoto, for their kind suggestions and insightful comments. They kindly spared their precious time despite their busy schedule.

Part of this work was done during my stay at Université Paris-Est, France. I would like to thank Associate Professor Vu-Hieu Nguyen, at Université Paris-Est, for his technical help in the numerical simulation and insightful feedback on my work. I also express my gratitude to Dr. Guillaume Haïat at CNRS and Professor Salah Naili at Université Paris-Est for their fruitful comments, discussion and kind support in Paris.

I also would like to express my gratitude to members of the bone quantitative ultrasound community in Japan; Professor Mami Matsukawa at Doshisha University, Associate Professor Atsushi Hosokawa at National Institute of Technology, Akashi College, Associate Professor Yoshiki Nagatani at Kobe City College of Technology, and students at Professor Matsukawa's laboratory. My special thanks go to my friends who participated in discussion many times with me: Dr. Kailiang Xu with ESPCI Paris, Assistant Professor Shohei Mori with Tohoku University, Mr. Kazuki Tamura with Chiba University, and Ms. Kazuyo Ito also with Chiba University.

I would also like to extend my sincere appreciation to the staff at Toru Sato Laboratory. I am deeply grateful to Associate Professor Seiji Norimatsu for his constructive advice and criticism. His kindness and attentive comments were very precious to me and my work. I wish to extend my gratitude to Associate Professor Takuya Sakamoto, now at University of Hyogo for fruitful discussion and tentative coaching. I have learned a lot from his excellent research papers. I am grateful to Associate Professor Kenshi Saho, now at Toyama Prefectural University. I have learned the basics of engineering and presentations. I would like to extend my gratitude to Assistant Professor Taishi Hashimoto for his dedicated coaching on programming, computers, and network maintenance. My special thanks go to Secretary Shoko Horibe for her careful support and great coffee.

This work was partly supported by a JSPS Grant-in-Aid for JSPS Research Fellow (Grant No. 15J05687).

Last but not least, my heartfelt appreciation goes to my family for their thorough support, patience, encouragement, and understanding.

Preface

Medical ultrasound devices are widely used in clinical situations. Compared with X-ray and magnetic resonance imaging-based tests, the medical ultrasound test has less hardware costs, is non-invasive, and offers real-time imaging and superior portability. However, the resolution and reliability of the technique are limited. Improvements to the accuracy and the resolution are strongly desired, as they may improve the accuracy of medical diagnoses. The medical ultrasound probe normally consists of multiple ultrasound elements, and therefore, investigation of the array signal processing technique should be a key to overcoming the shortages of the medical ultrasound test.

The two-dimensional medical ultrasound image is called the B-mode image. B-mode imaging consists of multiple one-dimensional signal intensity profiles, which are displayed as brightness of the image. A non-adaptive time-delay process which makes focal points is widely used in the clinical devices. However, the lateral resolution of the non-adaptive process is determined by the aperture size of the probe. Although several adaptive beamforming techniques have been proposed to further improve the lateral resolution, these adaptive beamforming techniques have a high computational cost because of the difference between the theoretical model of the adaptive beamforming and the actual conditions. A narrow-band signal is used as the theoretical model for the adaptive beamforming; however, in B-mode imaging a wide-band signal is used. Reduction of the computational complexity is a critical problem, because the real time imaging aspect is one of the strong points of the medical ultrasound test.

In addition to B-mode imaging, ultrasonic array probes are also used in the quantitative ultrasound (QUS) devices used to evaluate the quality of bone. The QUS methods have been developed for screening and early-stage detection of osteoporosis, which is known as a serious disease of aged people. The QUS method for bone evaluation was first proposed in the 1980s. Compared with traditional medical ultrasound imaging devices, this field is a newer area of research. Bone mineral density (BMD) is currently used as the medical index for making diagnoses, and at present, BMD is measured by X-ray devices. Thus, for the same reason as for B-mode imaging, the development of QUS devices is also desired. Furthermore, QUS devices can estimate the information that cannot be estimated by X-ray-based methods.

The propagation of the ultrasound wave is determined by the elastic and geometrical

conditions of the medium. Therefore, the ultrasonic signal that propagates along the bone contains information on the bone properties, such as the elastic stiffness, thickness, porosity, and mineralization. Up until now, bone QUS devices have not been very widely used in the clinical situation, but the technique has strong potential to be a gold standard for bone quality diagnosis, and development of the bone QUS technique is important.

An array probe is used in the cortical bone assessment, with the method being referred to as axial transmission. Because the cortical bone, which exists at the outer part of the bone, supports the body load, the accurate assessment is required to maintain the quality of patients' lives. In the most axial transmission technique, the ultrasonic guided waves propagating along the cortical bone are analyzed. The cortical bone is locally recognized as a transversely isotropic plate, and thus the ultrasonic guided waves propagate. The wavenumbers and phase velocities of the guided waves reflect the properties of the propagation medium, and estimation of the wavenumber and phase velocity leads to the characterization of the cortical bone.

The wavenumber and phase velocity is estimated according to the difference of the phase and amplitude of the received signals at multiple elements. The basic methodology is the same as that used in the adaptive beamforming technique utilized in B-mode imaging. However, the conditions and requirements are different. In the wavenumber analysis, the narrow band signal theory is satisfied, which is not the case in B-mode imaging. Additionally, in B-mode imaging the intensity profile is required to make an image. However, for the axial transmission technique, the values of the wavenumber and phase velocity are required, not the profile.

In this thesis, we first propose a low-computational-complexity adaptive beamforming technique for B-mode imaging with a linear array, by focusing on the difference between the narrow-band and wide-band based adaptive beamforming methods. We second apply an adaptive beamforming technique for the axial transmission technique and propose a technique that can directly estimate the values of the wavenumber and phase velocities. We next propose a new algorithm for the axial transmission technique with a low computational complexity. This method is then investigated by a bone-mimicking transversely isotropic plate. We finally propose a low-cost technique that characterizes a homogeneous isotropic plate with just one transmitter and two receivers as a pilot study for the axial transmission technique.

List of acronyms and abbreviations

Following acronyms and abbreviations are used in this thesis.

1D	one dimensional
2D	two dimensional
A	anti-symmetric
AH	asymptotic homogenization
AIB	apparent integrated backscatter
AT	axial transmission
BMD	bone mineral density
BS	beam-space
BUA	broadband ultrasound attenuation
CPU	central processing unit
cSOS	cortical speed of sound
DAS	delay-and-sum
dB	decibel
DL	diagonal loading
DOA	direction of arrival
DXA	dual X-ray absorptiometry
ES	element-space
ESPRIT	estimation of signal parameters via rotational invariance technique
FAS	first arriving signal
FDTD	finite-difference time-domain
FFT	fast Fourier transform
fps	frames/sec
GPU	graphics processing unit
LLMS	linear least-mean-squares
MDL	minimum description length
MRI	magnetic resonance imaging
Np	neper
QUS	quantitative ultrasound
RAS	ultrasound spectroscopy

RF	radio frequency
RMSE	root mean square error
ROI	region of interest
S	symmetric
SNR	signal-to-noise ratio
SOS	speed of sound
S-SVD	sparse SVD
STA	synthetic aperture
SVD	singular-value decomposition

List of common symbols

Following symbols are commonly used in this thesis. Each chapter also introduces their meaning at the first usage. Some symbols have more than one usage; their meaning is clear from the context.

$(\cdot)^*$	complex conjugate
$(\cdot)^{\mathrm{T}}$	matrix transposition
$(\cdot)^{\mathrm{H}}$	matrix conjugate transposition (Hermitian matrix)
α	attenuation coefficient
Δl	element pitch
$\varepsilon_{\{*,*\}}$	strain along $\{*,*\}$ direction
η	diagonal loading factor
θ	angle
κ	viscosity
λ	wavelength
λ_{e}	eigenvalue
λ_{L}	Lamé's constant
μ_{L}	Lamé's constant
ξ	Poisson ratio
ρ	density
$\sigma_{\{*,*\}}$	stress along $\{*,*\}$ direction
Φ	scalar potential
$a_n(\theta)$	steering value
$\mathbf{a}(\theta)$	steering vector
c	propagation speed, phase velocity
c_{S}	shear wave velocity
c_{L}	longitudinal wave velocity
$C_{\{*,*\}}$	elastic stiffness coefficient
d	thickness
E	Young's modulus
f	frequency
f_0	center frequency

f_{d}	Doppler frequency
f_{r}	reference frequency
$H(f)$	transfer function
$\mathbf{H}$	vector potential
$H_{x,y,z}$	vector potential along x, y, z direction respectively
$\mathbf{I}$	identity matrix
j	pure imaginary unit
k	wavenumber
M	number of signals
N	number of receivers
N_{sub}	sub-array size
N_{ave}	number of spatial averaging
N_{tr}	number of transmitters
r	depth, range
$\mathbf{r}$	vector that represents the position
$\mathbf{R}$	covariance matrix
$\mathbf{R}_{\mathrm{A}}$	covariance matrix after spatial averaging
$\mathbf{R}_{\mathrm{AD}}$	covariance matrix after spatial averaging and time-delay process
$s(t)$	signal
$\mathbf{s}$	signal vector
$S(f)$	signal in frequency domain
$S_0(f)$	transmitted signal in frequency domain
$S_{\mathrm{r}}(f)$	reference signal in frequency domain
$\mathbf{S}(f)$	signal vector in frequency domain
t	time
$\mathbf{u}$	particle displacement vector
$u_{x,y,z}$	displacement along x, y, z direction, respectively
v	Doppler velocity
v_x	Doppler velocity along x direction
v_z	Doppler velocity along z direction
x	axis
y	axis
z	axis

Chapter 1

General Introduction

1.1 Introduction

Ultrasonic waves are elastic waves of a frequency that exceeds the audible frequency range of human hearing. Ultrasonic waves propagate in body soft tissue with a speed of around 1500 m/s (Cobbold, 2006; Laugier and Haïat, 2011). Because this speed is very much slower than light, an ultrasound system can easily measure the distance to a target and its speed in the body using a much simpler system compared to the radio wave and light such as radar or laser based systems. Moreover, the penetration of ultrasound from the body surface to deep inside the body is easier. Hence, it is possible to focus waves with shorter wavelengths in the body; in other words, the resolution is higher. For these reasons, medical ultrasound technology has been widely used in clinical situations for diagnostic purposes to examine internal body structures.

Generally, ultrasonic waves of low frequency (about 20 kHz to 2 MHz) (Daffertshofer et al., 2005; Schoellhammer et al., 2015) are used for treatments. Waves of frequencies ranging from 1 to 40 MHz are used in diagnostics, whereas high frequency waves (more than 50 MHz) are used in ultrasonic microscopes (Ito et al., 2017; Yoshida et al., 2016). The frequency is determined according to required target depth and the resolution. For example, 5-MHz waves are used for fetal imaging because the amniotic fluid surrounding the fetus is a low-attenuation propagation medium and high-resolution images are required (Deng et al., 2001). In contrast, for quantitative ultrasound (QUS) technology for the bone assessment, lower frequencies (around 1 MHz) are used because bone is both a dispersive and an absorbing medium (Laugier, 2008; Laugier and Haïat, 2011).

For medical imaging, not only ultrasound is used but also X-rays (Hu et al., 2001; Rabin et al., 2006) and magnetic field oscillating at radio frequency (RF pulses) are used (Connell et al., 2015; Sun et al., 2016). While X-ray and magnetic resonance imaging (MRI) techniques that use the RF pulses produce high-resolution images, they are not suitable for daily diagnostics because of their large size, high costs, lengthy imaging

times, and invasiveness. Medical ultrasound tests are noninvasive and are performed in real-time with simple portable devices. From this perspective, ultrasound is superior to X-ray and MRI. Furthermore, with ultrasonic waves, we can not only visualize internal body structures but also evaluate physical properties of the target such as elasticity (Raum et al., 2014; Shiina et al., 2015).

Ultrasound easily undergoes refractive scattering and interference that generate artifacts. Therefore, the quality of imaging and diagnostics is highly dependent on the ability of the operator. To solve this problem, various signal processing methods and measurement algorithms have been proposed in recent years. In consequence, clearer ultrasound images produced at higher frame rates are possible particularly with the improvements in speeds of central processing unit (CPU) and graphics processing unit (GPU) (Moghimirad et al., 2016; Tanter and Fink, 2014). In this section, we introduce some basics of medical ultrasound technology and signal processing methods and techniques that have been developed recently.

1.2 Basics of medical ultrasound imager

1.2.1 Pulse echo method

First, we describe the fundamentals of the pulse echo method and the theory underlying ultrasound imaging. The pulse echo method uses a wide-band signal to determine the distance from a transmitter and a receiver to a target. The transmitted signal is reflected at the boundaries of objects with different acoustic impedances.

When we use a single ultrasonic element as a transmitter and receiver, the delay time t_0 is given by

$$t_0 = 2r_0/c, \tag{1.1}$$

where c is the speed of propagation and r_0 is the distance from the element to the target.

The depth (range or fast time) resolution is determined by the bandwidth of the transmitted pulse. The lateral resolution, Δr_{xf}, which is normal to the range direction, is determined by the aperture size of the probe, $N\Delta l$, when we use a linear array probe which composed of N elements with the pitch of Δl; for far fields its approximate form is

$$\Delta r_{xf} \approx \frac{r_f \lambda}{N\Delta l}, \tag{1.2}$$

where λ is the wavelength of the signal and r_f the focal depth. Hence, for a probe of fixed aperture, the resolution decreases with depth (Van Trees, 2002). Therefore, depending

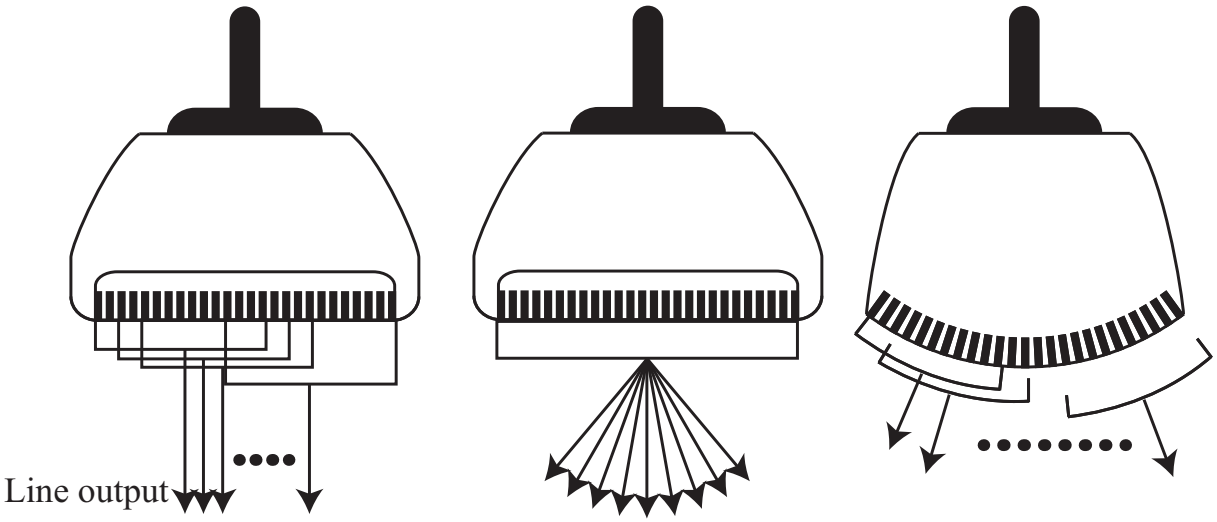

Figure 1.1: Probe types and scanning methods: (a) linear array probe with line scanning method, (b) linear array probe with a sector scanning method, and (c) convex array probe with a off-set sector scanning method.

on the measurement depth, aperture size can be varied in some medical ultrasound imagers.

1.2.2 Basics of medical ultrasound 2D imaging system

By arranging multiple one-dimensional (1D) intensity profiles acquired by the pulse-echo and focusing methods that form focal points by using time-delay processes, a two-dimensional (2D) ultrasound image is generated. The intensities of the multiple 1D intensity profiles are displayed as brightness in an image. To create the 2D image, an ultrasonic array probe is normally used. An ultrasonic array probe consists of multiple small ultrasonic elements used as both transmitters and receivers. Multiple 1D intensity profiles are called scanning lines. There are various types of probes and scanning methods (Fig. 1.1) (Cobbold, 2006).

Fig. 1.1 presents the schematics of two probe types (linear and convex arrays) and two scanning methods (line and sector scanning) that are widely used in 2D medical ultrasound imaging.

With linear scanning using the linear array, multiple scanning lines are generated by electronically changing the group of ultrasonic elements that are used as transmitters and receivers. For sector scanning, all elements are used simultaneously, and imaging

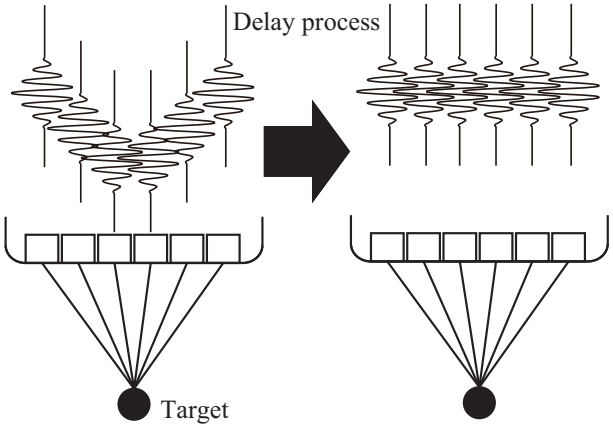

Figure 1.2: Schematic presentation of delay-and-sum technique.

is performed by changing the focal positions. Since all elements are used for imaging simultaneously, no electronic switching is required. The same resolution can be achieved using a smaller aperture size than for a linear scan. Hence, sector scanning is used in clinical applications when a small size probe is required to avoid obstacles that prevent ultrasound signals from penetrating, for example, the ribs in cardiac imaging.

For the convex array, the ultrasonic elements are arranged on a convex surface of a certain curvature. It can scan a wider imaging region than a linear array. Therefore, it is used in the diagnostics of abdominal organs, which requires a wide imaging area, even of organs that lie deeper within the body.

Delay and sum technique

Here, we describe a beamforming technique to establish the focal point. Classical non-adaptive beamforming is called the delay-and-sum (DAS) method. The schematic presentation of the DAS method is shown in Fig. 1.2. This method establishes the focal point by applying a theoretically determined time-delay value to the transmitters and receivers (Cobbold, 2006).

Let us define vectors $\mathbf{r}_{\mathrm{e},i}$ and $\mathbf{r}_{\mathrm{f}}$ representing the positions of the i-th elements and focal point, respectively. The associated time delay t_i required to determine the focal point is given by

$$t_i = \frac{|\mathbf{r}_{\mathrm{f}} - \mathbf{r}_{\mathrm{e},i}| - |\mathbf{r}_{\mathrm{f}}|}{c}. \tag{1.3}$$

To generate a plane wave with the designated angle θ as for a sector scan with a linear

array probe, the time delay given at the time of transmission is

$$t_i = \frac{(i-1)\Delta l \sin\theta}{c}. \tag{1.4}$$

To improve the resolution, a dynamic focusing method has been proposed. When the focal point is set at a single point, the resolution improves only near the focal point; in other places, the resolution is low. By employing multiple focal points and adding the received signals obtained by them, it is possible to improve the resolution over a longer depth range. Nevertheless, when multiple-point focusing occurs mechanically with transmission and reception events, the frame rate decreases proportionally with the number of focal points. To avoid this drawback, digital beamforming is employed at signal reception(Jensen et al., 2006).

Synthetic aperture imaging

So far, we have described the methods of transmission and reception associated with a fixed-size array. The synthetic aperture (STA) method is one for which the transmitter and the receiver are driven separately and improves image resolution through the use of images generated by various combinations of transmitters and receivers (Jensen et al., 2006, 2016b). From the conceptual diagram of the STA method (Fig. 1.3) (Jensen et al., 2006, 2016b), the transmitters are driven one by one, and reflected signals are recorded by all receivers. As the beam width of a single transmitter is wide, the resolution of each image with a single transmitter is low. By adding the generated low-resolution image, it is possible to generate a high-resolution image.

The signal processing used in the STA method is expressed as

$$s_{\mathrm{f}}^{\mathrm{R}}(\mathbf{r}) = \sum_{j=1}^{N}\sum_{i=1}^{N_{\mathrm{tr}}} s^{\mathrm{R}}(t(i,j),i,j), \tag{1.5}$$

$$t(i,j) = \frac{|\mathbf{r}-\mathbf{r}_{\mathrm{e}}(i)| + |\mathbf{r}-\mathbf{r}_{\mathrm{r}}(j)|}{c}, \tag{1.6}$$

where $s^{\mathrm{R}}(t,i,j)$ is the received signal at the i-th transmitter and the j-th receiver, $s_{\mathrm{f}}^{\mathrm{R}}(\mathbf{r})$ is the output of the STA method, N and N_{tr} are the number of receivers and transmitters, respectively, $\mathbf{r}$ is the vector indicating the measurement position, and $\mathbf{r}_{\mathrm{e}}$ and $\mathbf{r}_{\mathrm{r}}$ are the positions of the transmitter and receiver, respectively.

Eq. (1.5) shows that the result produced by the STA method is equivalent to the result when we perform dynamic focusing on all imaging points at transmission and reception.

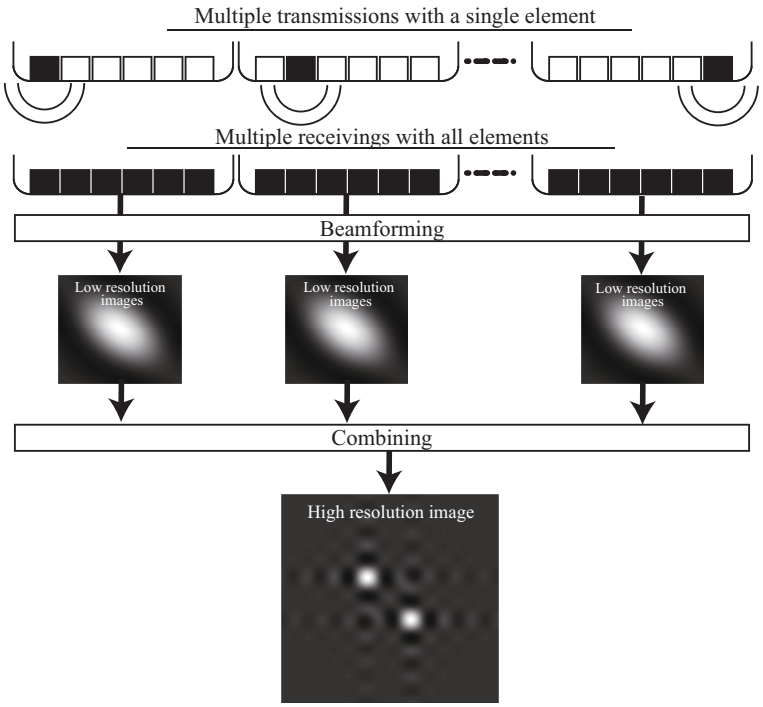

Figure 1.3: Schematic of synthetic aperture imaging.

In other words, this STA result has the highest resolution when we use the non-adaptive DAS method (Jensen et al., 2006). In addition, adaptive beamforming can be applied to STA to improve the resolution.

One problem with the STA method is penetration. Specifically, transmission is performed with a single element. This makes it difficult to image deep regions within the body. To solve this problem, a method that simultaneously excites multiple transmitters (Moghimirad et al., 2016) or uses a chirp signal as a transmitted signal have been proposed (O'Donnell, 1992). Another problem is the computational complexity. However, with recent improvements in computing speeds of CPUs and GPUs, the implementation of the STA method has become possible in commercial imagers. Note that reducing the computational complexity remains an obstacle in making low-cost measurement systems. Moghimirad et al. (2016) proposed a method that creates a virtual source using multiple transmitters and replaces the time delay at transmission and reception by a 2D fast Fourier transform (FFT) analysis. The amount of calculations was reduced by 1/20 without any deterioration in resolution.

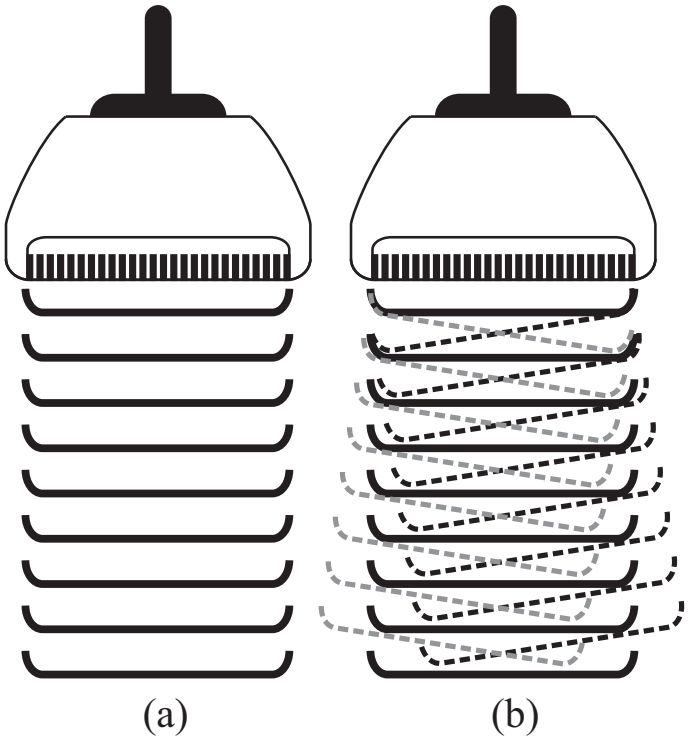

Figure 1.4: Comparison of transmission schemes: (a) plane-wave transmission with a single-angle compound, (b) plane-wave transmission with multiple-angle compound.

Plane wave imaging

In recent years, ultrafast imaging using plane-wave transmission has been proposed and attracts strong attention (Tanter and Fink, 2014). Ultrafast imaging refers to an imaging method with a fast frame rate. Fig. 1.4 shows an overview of plane-wave transmission. The plane-wave transmission technique involves transmitting a plane-wave signal over a wide imaging area simultaneously and employs on reception the digital beamforming technique. Thus the technique does not require time for changing the transmitter and receiver groups and can increase the frame rate. When we consider the DAS image generated by a linear array probe using a linear scanning method and consisting of 128 lines and 4 dynamic focusing points, the frame rate is about 25 frames/sec (fps) (Tanter and Fink, 2014). Single angle plane-wave imaging such as Fig. 1.4(a) achieves about 18000 fps because the plane-wave transmission technique does not require time to switch the transmitter group to change the focal position(Tanter and Fink, 2014). However, the resolution is low.

To improve the resolution, a compound method that adds the generated images with different transmitting angles has been widely used (Fig. 1.4(b)) (Tanter and Fink, 2014). Because the compound method increases the resolution by summing up the images with different transmission angles, the frame rate decreases. The frame rate is about 1000 fps with 17 angles and about 350 fps with 40 angles. Plane-wave imaging can be applied not only to B-mode imaging but also to Doppler velocity estimations of blood flow (Hasegawa and Kanai, 2008) and elastography, which measures tissue quality (Shiina et al., 2015).

1.2.3 Doppler velocity measurement

Ultrasonic Doppler diagnostics is a technology by which blood flow velocity can be estimated as well as the velocities of displaced tissue, which enables a non-invasive evaluation of tissue quality. The continuous-wave Doppler method was developed initially and used in the clinical situation (Berger et al., 1985; Currie et al., 1985). However, the method does not provide any depth (range) resolution. In contrast, the pulse-wave Doppler method has depth resolution and is now used widely. Color and power Doppler methods that display simultaneously real-time 2D images and Doppler information have been developed and are widely employed in commercial devices (Chang et al., 2009; Kasai et al., 1985).

If we assume the target moves with velocity v as shown in Fig. 1.5, the frequency of the received signal is expressed as

$$f = \frac{c+v_z}{c-v_z} f_0 \tag{1.7}$$

$$\approx \left\{ \frac{1+2v_z}{c} \right\} f_0, \tag{1.8}$$

where f_0 and f are the central frequency and received signal frequency and v_z is the velocity of the target projected along the direction of gaze (Jensen et al., 2016a). The approximation, $v_z \ll c$, is used in the latter equation. The Doppler shift f_d is defined as $f_\mathrm{d} = f - f_0$.

As shown in Eq. (1.7), when we measure the Doppler velocity from one location with a simple algorithm, only the velocity along the direction of gaze can be obtained. However, the measurement of multi-directional blood flow is important in medical diagnostics. We next introduce methods to estimate blood flow velocities along more than one direction.

Multi-beam method

If we consider blood flowing at an angle θ_b and measure the Doppler velocity with a transmission beam angle of θ_t and reception beam angle of θ_r, the Doppler shift is obtained from

$$f_\mathrm{d} = \frac{|v|\cos(\theta_\mathrm{t} - \theta_\mathrm{b}) + |v|\cos(\theta_\mathrm{r} - \theta_\mathrm{b})}{c} f_0, \tag{1.9}$$

which can be rearranged to give

$$v_z(\cos\theta_\mathrm{t} + \cos\theta_\mathrm{r}) + v_x(\sin\theta_\mathrm{t} + \sin\theta_\mathrm{r}) = c f_\mathrm{d}/f_0, \tag{1.10}$$

where $v_x = |v|\sin\theta_\mathrm{b}$ and $v_z = |v|\cos\theta_\mathrm{b}$ (Jensen et al., 2016a).

To measure the 2D blood flow velocity, at least two beams are required; see Fig. 1.5(a). When we measure the Doppler velocity with multiple beams with multiple angles, the Doppler velocities and shifts are related by

$$\frac{c}{f_0}\begin{bmatrix} f_\mathrm{d11} \\ f_\mathrm{d21} \\ \vdots \\ f_{\mathrm{d}N_\mathrm{bt}N_\mathrm{br}} \end{bmatrix} = \begin{bmatrix} \cos\theta_\mathrm{t1} + \cos\theta_\mathrm{r1} & \sin\theta_\mathrm{t1} + \sin\theta_\mathrm{r1} \\ \cos\theta_\mathrm{t2} + \cos\theta_\mathrm{r1} & \sin\theta_\mathrm{t2} + \sin\theta_\mathrm{r1} \\ \vdots & \vdots \\ \cos\theta_{\mathrm{t}N_\mathrm{bt}} + \cos\theta_{\mathrm{r}N_\mathrm{br}} & \sin\theta_{\mathrm{t}N_\mathrm{bt}} + \sin\theta_{\mathrm{r}N_\mathrm{br}} \end{bmatrix} \begin{bmatrix} v_z \\ v_x \end{bmatrix}, \tag{1.11}$$

where $\theta_{\mathrm{t,r}i}$ is an i-th transmission and reception beam angle, $f_{\mathrm{d}ij}$ denotes the Doppler velocity of the i-th transmitting and j-th receiving beam angle combination, N_bt and N_br are the number of beam angles corresponding to transmission and reception, respectively.

In the matrix form, Eq. (1.11) becomes

$$\mathbf{u}_\mathrm{v} = \mathbf{A}_\mathrm{v}\mathbf{v}_\mathrm{v}. \tag{1.12}$$

Therefore, the 2D velocities can be estimated by solving the least squares problem,

$$\mathbf{v}_\mathrm{v} = (\mathbf{A}_\mathrm{v}^\mathrm{T}\mathbf{A}_\mathrm{v})^{-1}\mathbf{A}_\mathrm{v}^\mathrm{T}\mathbf{u}_\mathrm{v}. \tag{1.13}$$

Transverse oscillation

The transverse oscillation method estimates the Doppler velocity along the transverse direction (x direction) by generating the transversely oscillated field (Jensen, 2001; Jensen and Munk, 1998). The field is generated by combining two ultrasound fields formed by the two apodization settings. The apodization technique employs weighting functions

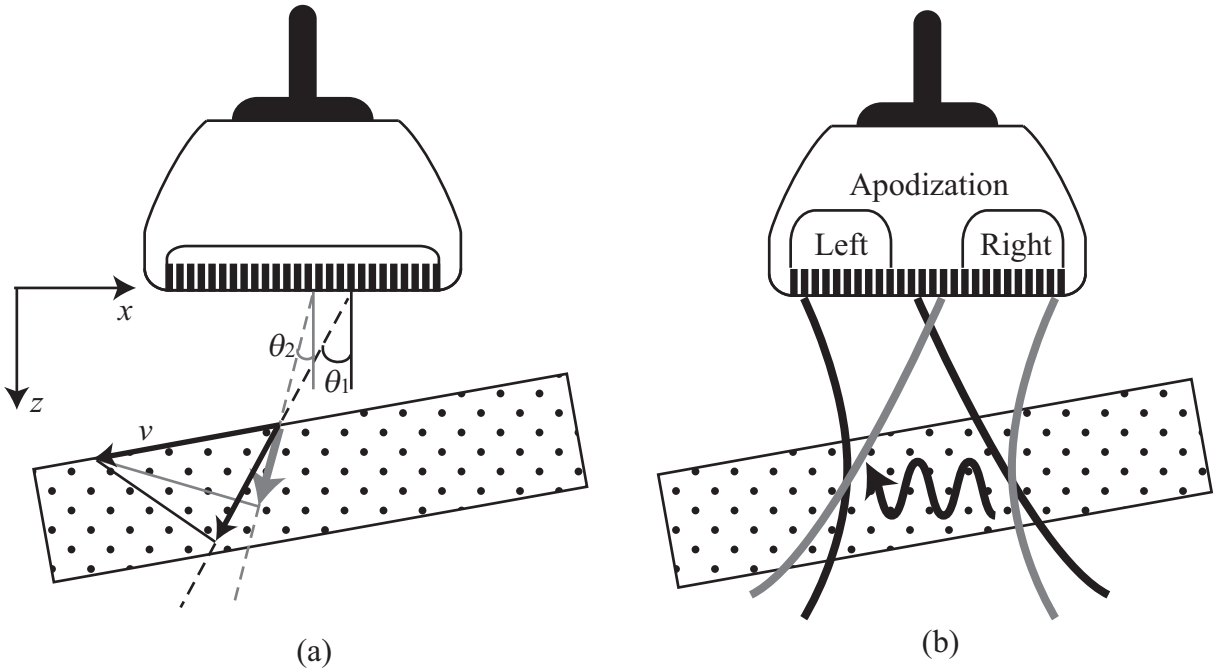

Figure 1.5: Schematics for 2D Doppler velocity estimation: (a) multi-beam method, (b) transverse oscillation method.

such as the Gaussian function at transmission or reception and controls the beam pattern. Normally, the function increases at the central part of the aperture and decreases at the edge. The relationship between the oscillation field and the apodization function at the focal point is given by the Fourier transform (Udesen and Jensen, 2006). Therefore, if we do not employ the apodization function, the field is a sinc function with many sidelobes. This is the reason why the apodization function normally decreases at the edge.

The transverse oscillation method forms a transversely oscillated field to estimate the blood flow velocity along x direction; see Fig. 1.5. The transverse oscillation method forms an oscillation field, $F_{\mathrm{v}}(x)$, such as

$$F_{\mathrm{v}}(x) = \cos(2\pi x/\lambda_x)\mathrm{rect}(L_{\mathrm{v}}), \tag{1.14}$$

where $\mathrm{rect}(L_{\mathrm{v}})$ is a rectangular window with a lateral length L_{v}, and λ_x is a spatial wavelength along the transverse direction. The inverse Fourier transform of Eq. (1.14) consists of two sinc functions with a certain distance. The employment of the field given in Eq. (1.14) is similar to the quadrature detection and sampling with an interval λ_x along the transverse direction.

For simplicity, if we can acquire the two ideal fields, $\cos(2\pi x/\lambda_x)$ and $\sin(2\pi x/\lambda_x)$, the received signals with blood flow velocities of v_x and v_z are given by

$$F_{\mathrm{c}}(n_{\mathrm{T}}) = \cos(\theta_x(n_{\mathrm{T}}))\exp(\mathrm{j}\theta_z), \tag{1.15}$$

$$F_{\mathrm{s}}(n_{\mathrm{T}}) = \sin(\theta_x(n_{\mathrm{T}}))\exp(\mathrm{j}\theta_z), \tag{1.16}$$

where n_{T} is the number of pulse repetitions, θ_x and θ_z are the phase components that are determined by the velocity, $\theta_x(n_{\mathrm{T}}) = 2\pi v_x n_{\mathrm{T}} T/\lambda_x$, and $\theta_z(n_{\mathrm{T}}) = 2\pi v_z n_{\mathrm{T}} T/\lambda_z$. Note that we omit the component that is related to the amplitude.

The differences in the phases with respect to the pulse repetitions are given by

$$\Delta\theta_{x,z} = 2\pi v_{x,z} n_{\mathrm{T}} T/\lambda_{x,z}. \tag{1.17}$$

Using Eqs. (1.15) and (1.16), we obtain the following signals:

$$F_1(n_{\mathrm{T}}) = F_{\mathrm{c}}(n_{\mathrm{T}}) + \mathrm{j}F_{\mathrm{s}}(n_{\mathrm{T}}) = \exp\{\mathrm{j}(\theta_z(n_{\mathrm{T}}) + \theta_x)\}, \tag{1.18}$$

$$F_2(n_{\mathrm{T}}) = F_{\mathrm{c}}(n_{\mathrm{T}}) - \mathrm{j}F_{\mathrm{s}}(n_{\mathrm{T}}) = \exp\{\mathrm{j}(\theta_z(n_{\mathrm{T}}) - \theta_x)\}, \tag{1.19}$$

the phase differences being

$$\Delta\theta_z(n_{\mathrm{T}}) + \Delta\theta_x(n_{\mathrm{T}}) = \angle\{F_1^*(n_{\mathrm{T}})F_1(n_{\mathrm{T}}+1)\}, \tag{1.20}$$

$$\Delta\theta_z(n_{\mathrm{T}}) - \Delta\theta_x(n_{\mathrm{T}}) = \angle\{F_2^*(n_{\mathrm{T}})F_2(n_{\mathrm{T}}+1)\}, \tag{1.21}$$

where $(\cdot)^*$ denotes the complex conjugate. Therefore, with these two equations, the velocities of the two directions can be estimated. This method can be used in combination with plane-wave imaging, which has been verified in in-vivo measurements and can accurately estimate the velocity (Lenge et al., 2015).

Speckle tracking

In blood flow, red blood cells scatter the transmitted signals. These cells can be recognized as point targets that are randomly and densely distributed. The intensity of the reflected signals from the blood cells is weak and these weak signals interfere with each other. Indeed, they form a B-mode image with a unique interference pattern called speckle (Yamaguchi et al., 2000).

The speckle reflects the distribution of scatters. Therefore, if we assume that the distribution of the blood cells does not change significantly within a short duration, we can estimate the blood flow velocity by tracking the speckle of the image (Hein and O'Brien, 1993; Yeung et al., 1998). When speckle tracking is employed to estimate the blood flow velocity, an ultrasound contrasting agent is sometimes used and injected into the blood to improve the signal-to-noise ratio (SNR) (Abe et al., 2013).

1.3 Quantitative ultrasound technology for bone assessment

So far, we introduced the theories for the medical ultrasound imaging. In this section, we introduce the QUS technologies for bone quality assessment. Osteoporosis is defined as follows (International Osteoporosis Foundation, 2002):

> Osteoporosis is a disease in which the density and quality of bone are reduced, leading to weakness of the skeleton and increased risk of fracture, particularly of the spine, wrist, hip, pelvis and upper arm.

Recently, the population has begun to age rapidly and the number of osteoporosis patients is thus also likely to increase. A technique that can detect osteoporosis in its early stages and can also assess the risk of bone fracture is therefore highly desirable.

In clinical scenarios, osteoporosis diagnosis is performed on the basis of the bone mineral density (BMD). The BMD is generally estimated using dual X-ray absorptiometry (DXA) (Simonelli et al., 2008). DXA is the gold standard method for BMD estimation; however, the DXA method is not suitable for screening use because of its invasiveness in terms of X-ray emissions. Additionally, the BMD does not represent all the physical parameters of bone. For example, bone fractures can occur in patients with good BMDs (Schuit et al., 2004). In particular, X-ray-based methods cannot estimate certain important physical and elastic parameters of bone such as the longitudinal and shear wave velocities. Therefore, for accurate osteoporosis diagnosis, evaluation methods for bone quality estimation have recently attracted considerable attention. The "bone quality" properties include (Laugier and Haïat, 2011; Pothuaud et al., 2000):

> The bone geometry, the cortical properties, the trabecular micro-architecture, the bone tissue mineralization, the quality of the collagen and hydroxyapatite crystals, and the presence of microcracks in the bone.

QUS methods have been developed to estimate bone quality. QUS methods are superior to X-ray based techniques because they offer equipment portability, a non-invasive

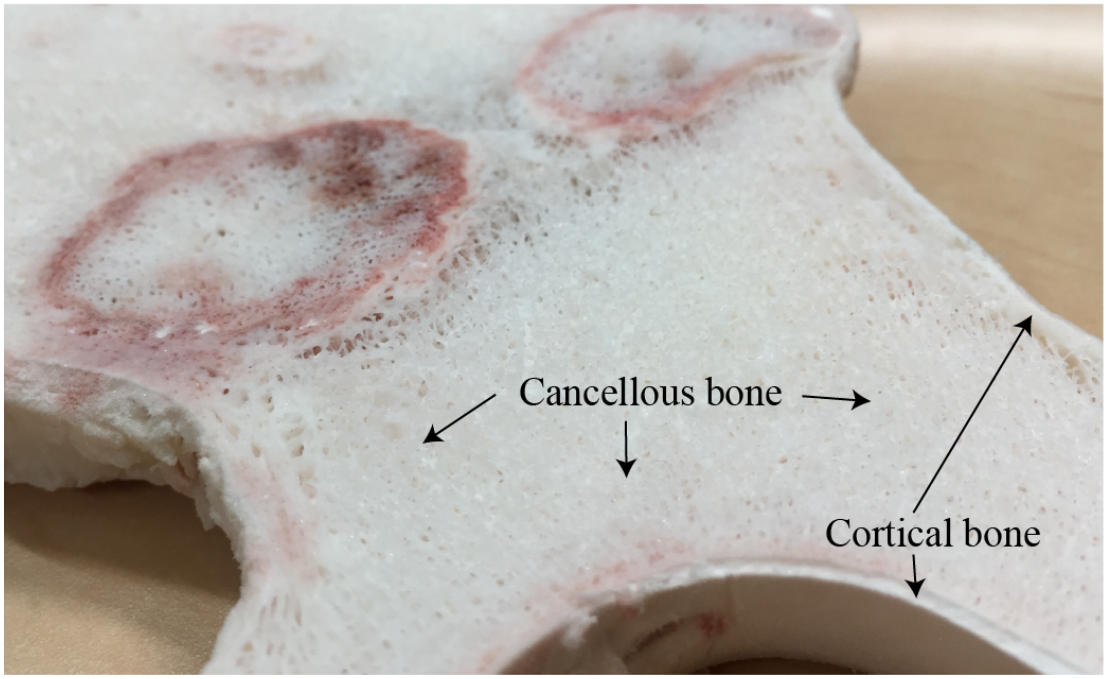

Figure 1.6: Photograph showing cortical and cancellous bone tissues.

measurement capability, and low cost. Langton et al. (1984) proposed a technique that measures the frequency-dependent attenuation of an ultrasonic signal after it propagates through a patient's heel. Many studies have shown that this method outputs results that are strongly correlated with those of DXA and clinically investigated (Marín et al., 2006). Unfortunately, QUS method is not widely used in clinical applications at present. However, the method has strong potential to provide an alternative and improved method for assessment of osteoporosis.

1.3.1 Overview of bone structure

From the macro (mm) scale viewpoint, bone is composed of two different types of bone tissue, which are called cancellous bone and cortical bone (Laugier and Haïat, 2011). Fig. 1.6 shows a photograph of a section of a bovine femur. Cancellous bone exists

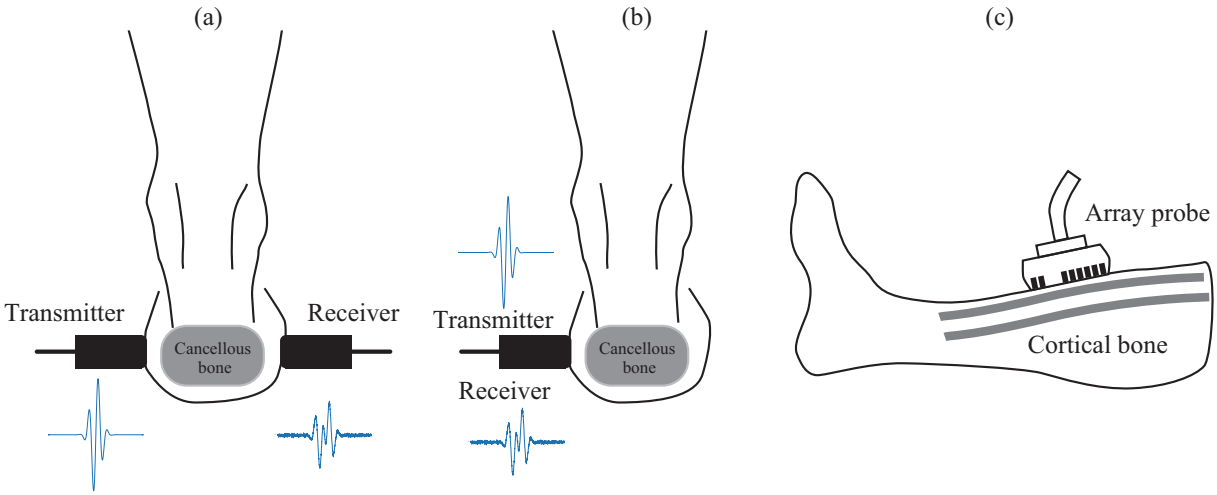

Figure 1.7: Schematic illustrations of available QUS methods. (a) Transverse transmission method. (b) Backscatter method. (c) Axial transmission method.

in the inner part of the bone and is constructed from the thin cylinder and plate-like bones, which are called trabecular bones. These trabecular bones form honeycomb-like structures and the cancellous bone is highly porous. The vacancies in the trabecular bone are filled by the bone marrow. Because of its high porosity, cancellous bone is both light in weight and flexible. Quantitative evaluation of the cancellous bone is crucial for early stage diagnosis of osteoporosis because this bone type is susceptible to the structural changes that reflect the presence of osteoporosis.

Cortical bone is the hard type of bone tissue that exists at the outer surface of the bone. It has a dense structure and its porosity is lower than that of cancellous bone. The cortical bone structure supports the body load and plays an important role in body parts that require both strength and stiffness, such as arm and leg. When a bone fracture is caused by osteoporosis in the cortical bone, the quality of the patient's life decreases acutely and the patient is likely to become bedridden. In addition, studies have been reported that show the importance of cortical bone assessment (Kanis et al., 2001; Raum et al., 2014; Riggs et al., 1981).

1.3.2 Transverse transmission

Fig. 1.7 shows a schematic illustration of the currently available QUS methods. These methods are introduced in more detail in the following sections.

Attenuation

First, we would like to explain the units used for the attenuation. The decibel (dB) and the neper (Np) are widely used to express attenuation numerically (Rose, 1999). The received signal, $S(f)$, that has passed through the absorbing medium is expressed as follows:

$$S(f) = S_0(f)\exp(-\alpha(f)d), \tag{1.22}$$

where $S_0(f)$ is the transmitted signal, $\alpha(f)$ is the frequency-dependent attenuation coefficient, and d is the propagation distance.

The units Np and dB are defined using the following equations:

$$\alpha_{\mathrm{np}} = \ln(S(f)/S_0(f)), \tag{1.23}$$

$$\alpha_{\mathrm{dB}} = 20\log(S(f)/S_0(f)), \tag{1.24}$$

where α_{np} and α_{dB} are the attenuation coefficients in Np and dB, respectively.

The following relationship therefore exists between the dB and the Np.

$$\alpha_{\mathrm{dB}} = \frac{20}{\ln(10)}\alpha_{\mathrm{np}} \tag{1.25}$$

$$\approx 8.68\alpha_{\mathrm{np}}. \tag{1.26}$$

BUA and SOS

The broadband ultrasound attenuation (BUA) and the speed of sound (SOS) are the initial indexes that were developed for use with the QUS method. The BUA was proposed by Langton et al. (1984). The method transmits a wide-band ultrasonic wave and analyzes the signal after it has passed through a patient's heel, as shown in Fig. 1.7(a). The attenuation is calculated using the signal intensity in the frequency domain, as follows:

$$\alpha(f)d = 8.68\ln\frac{S_{\mathrm{r}}(f)}{S(f)}, \tag{1.27}$$

where S_{r} is the signal that has passed through a reference material with known attenuation and d is the thickness of the bone. Note that when the existence of the soft tissue is ignored, the bone thickness at the heel is easy to measure because it is equivalent to the distance from the transmitter to the receiver.

The BUA is then calculated by applying a linear regression fitting process in the lower frequency range, e.g., from 0.2 to 0.6 MHz. This lower frequency range is selected

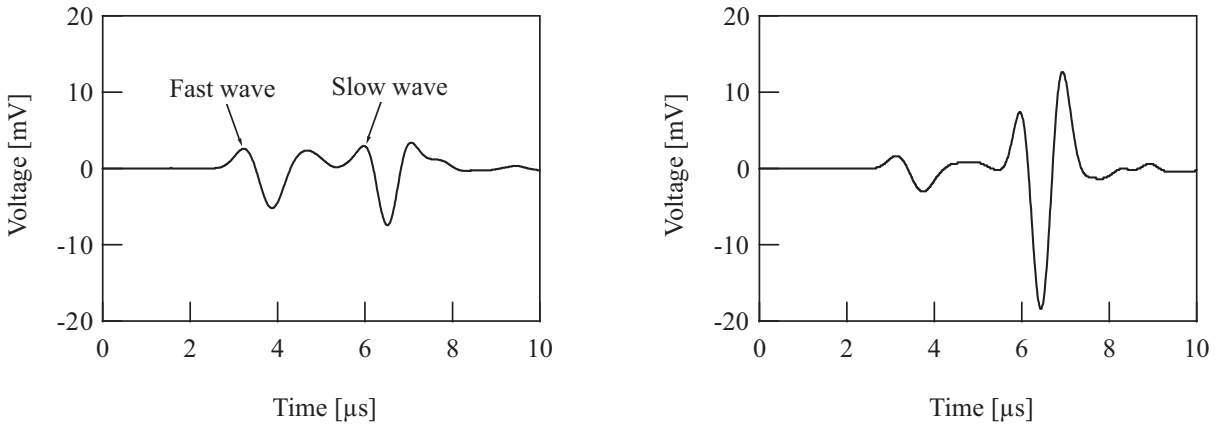

Figure 1.8: Fast and slow waves: (a) with high-density bone, and (b) with low-density bone. (Reproduction from Otani (2005); Copyright (2005), The Japan Society of Applied Physics.)

because the signals in the high-frequency range are strongly attenuated and the SNR is not sufficient for estimation of bone quality. There are many different sources of attenuation, such as refraction and reflection, but this method averages and takes all of these attenuation sources into account.

The SOS is a measure of the velocity of an ultrasonic wave that has passed through bone. Because we already know the thickness of the bone, estimation of the SOS is performed by detecting the peak position of the received waveform. This technique has been implemented in commercial medical equipment. When these QUS measurement methods have been used to analyze cancellous bone, they have shown high correlation with the results of BMD-based in several studies (Haïat et al., 2005; Rossman et al., 1989).

1.3.3 Fast and slow waves

Overview of the fast and slow wave phenomena

The above method recognizes the received ultrasonic wave that has passed along the bone as a single wave, despite the fact that there are multiple propagation media available, including tissue, skin, bone marrow, cortical bone, and cancellous bone. Techniques that focus on the differences between these propagation media have also been proposed.

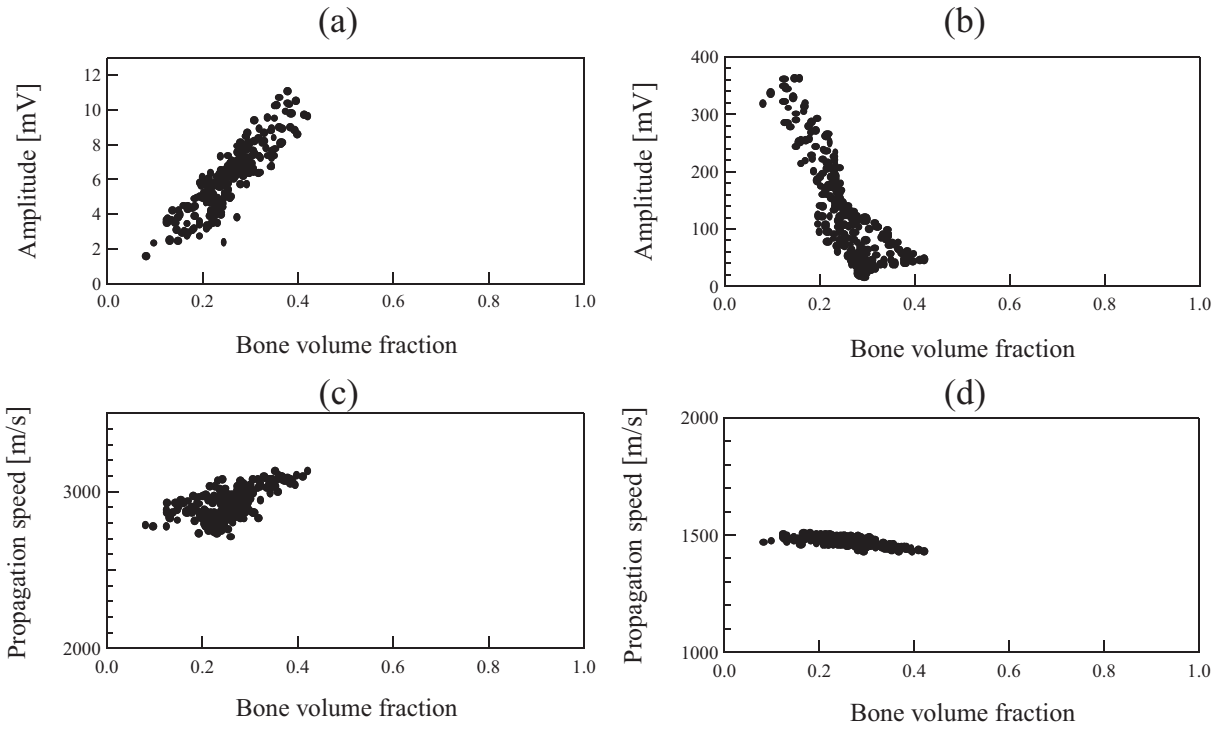

Figure 1.9: Relationships between the amplitudes and propagation speeds of the slow and fast waves. Amplitudes of (a) fast and (b) slow waves. Propagation speeds of (c) fast and (d) slow waves. (Reproduction from Otani (2005); Copyright (2005), The Japan Society of Applied Physics.)

Hosokawa and Otani (1997) reported experimental observation of the two-wave (fast and slow wave) propagation phenomenon when an ultrasonic signal propagated along the cancellous bone, as shown in Fig. 1.8 (Otani, 2005). This phenomenon was predicted theoretically using Biot's theory (Biot, 1956a,b, 1962).

When a signal propagates along cancellous bone, there should be two types of propagation medium: the bone marrow and the trabecular bone. The propagation speeds of ultrasonic waves in the bone marrow and the trabecular bone are approximately 1450 and 3000–4000 m/s, respectively (Laugier and Haïat, 2011). The propagation speed in bone marrow is similar to that in the surrounding tissue and that in water. The speed difference between the two media is large and thus causes the two-wave propagation phenomena. The propagation speeds of the slow and fast waves should correspond with the speeds in the bone marrow and the trabecular bone, respectively.

Fig. 1.9 (Otani, 2005) shows the correlation between the parameters of the two-wave phenomenon and the bone volume fraction (bone volume/total volume, or BV/TV).

Otani (2005) showed that the amplitude and velocity of the fast wave show positive and high correlation, while the amplitude of the slow wave has a negative correlation. As shown in Fig. 1.9(d), the slow wave velocity does not show this correlation because the velocity of the slow wave corresponds to that in the bone marrow and it is not dependent on either the patient or the measurement point. In other words, Fig. 1.9(d) shows the strong possibility that the slow wave propagation medium is the bone marrow.

A medical device that uses this phenomenon was developed and has been used in clinical scenarios (Mano et al., 2006). The practical device measures the two waves that propagate along the patient's forearm.

Characterization of the fast and slow waves

As shown in Fig. 1.8, the separation of the two waves is important for accurate bone quality estimation. However, when the fast and slow waves overlap strongly, it is difficult to estimate the wave velocities and amplitudes. Therefore, separation techniques that use the following theoretical model have been proposed and investigated.

The theoretical model of the fast and slow waves is given by the following (Nelson et al., 2011; Wear, 2014):

$$S(f) = S_0(f)\left[H_1(f) + H_2(f)\right], \tag{1.28}$$

where H_1 and H_2 are the transfer functions of the fast and slow waves, respectively. These transfer functions are expressed as:

$$H_i(f) = A_i^{\mathrm{r}} \exp\left[-\alpha_i f d + \mathrm{j}\left\{\frac{2\pi f d}{c_i(f)} - \frac{2\pi f d}{c_{\mathrm{W}}}\right\}\right], \tag{1.29}$$

$$\frac{1}{c_i(f)} - \frac{1}{c_i(f_{\mathrm{r}})} = -\frac{\alpha_i}{\pi^2}\ln\left(\frac{f}{f_{\mathrm{r}}}\right), \tag{1.30}$$

where $i = 1$ and 2 indicate the fast and slow waves, respectively. A_i^{r} is the signal amplitude parameter, α_i is the slope of the attenuation, d is the bone specimen thickness, c_i is the phase velocity, c_{W} is the speed of sound in water, and f_{r} is a reference frequency.

A separation method that uses an adaptive beamforming technique has been developed recently (Taki et al., 2017, 2015a). This method uses a fitting procedure with the modified theoretical model.

$$S(f) = S_0(f)\left[H_1(f)\exp(-\mathrm{j}\theta_1^{\mathrm{r}}) + H_2(f)\exp(-\mathrm{j}\theta_2^{\mathrm{r}})\right], \tag{1.31}$$

where $\theta_{1,2}^{\mathrm{r}}$ is the phase rotation factor that is used to consider the effects of the finite aperture size of the transducer. When we receive an ultrasonic signal at a transducer

of finite size, the wavefront arrival time at the transducer has a distribution and the transducer sums these wavefronts.

The propagation process is analyzed in detail using finite-difference time-domain (FDTD) numerical simulations and experiments (Nagatani et al., 2008). The numerical simulation models are mainly constructed using the X-ray imaging method. Realistic simulation models can thus be constructed.

1.3.4 Backscatter method

In Sects. 1.3.2 and 1.3.3, we introduced the method that uses two transducers and analyzes signals that penetrate the bone. In this section, we introduce a method based on a single transducer, as shown in Fig. 1.7(b). This technique is called the backscatter method because it analyzes the signal that is backscattered from the bone(Hoffmeister et al., 2006).

Because the backscatter method uses only a single transducer, the method can easily measure the signals from several different parts of the body, such as the hip and the spine (Liu et al., 2015). Because the bones that exist around the hip and the spine are sensitive to osteoporosis, the position-free measurement capability of the method is strongly advantageous. In addition to this advantage, as well as the transverse transmission method, the backscatter method can not only measure the information related to the BMD but can also measure the physical information (Ta et al., 2008; Wear, 2008).

Many indices have been proposed to evaluate the received signal. In this thesis, we introduce the apparent integrated backscatter (AIB) as an index because it does not require any information other than the received signal and the reference signal that passed through the reference material. The AIB compares the signal spectrum before and after application of the time-gate window that removes the signal that was reflected at the bone surface (Roux et al., 2001). The AIB shows high correlation with the BMD and is related to the ultimate strength of the bone (Liu et al., 2015; Riekkinen et al., 2007). AIB is given as

$$\frac{\int_{f_1}^{f_2} \ln \frac{S_{\mathrm{SOI}}(f)}{S_{\mathrm{r}}(f)} df}{f_2 - f_1}, \tag{1.32}$$

where $f_{1,2}$ is the frequency range used for the estimation process, and S_{SOI} is the spectrum of the backscattered signal of interest.

To identify S_{SOI}, an appropriate time window design is required because the backscattered signal contains the reflected signals from both the surface of the bone and the cortical bone, where the latter has a higher intensity. The performance of the method is

dependent on the time-gating window design and a study of appropriate filter design has thus been reported (Liu et al., 2015).

1.3.5 Axial transmission technique

Thus far, we have introduced methods for analysis of the cancellous bone. In this section, we focus on the assessment of the cortical bone, which is one of the main topics of this thesis. The schematic illustration of the axial transmission (AT) technique is shown in Fig. 1.7(c). In the AT technique, a probe is attached to the surface of the body, e.g., on the arm or the leg, using impedance-matching gel and the ultrasonic guided waves that propagate within the cortical bone along the axial direction is analyzed.

A previously reported method measures the speed of the first arriving signal (FAS) (Sasso et al., 2008). Fig. 1.10 shows the guided waves that propagate along the plate and were received by multiple receivers at multiple locations. We used a numerical simulation to calculate these received signals (Nguyen and Naili, 2012, 2013). The solid arrow in Fig. 1.10 represents the FAS. The FAS is measured and analysis shows that its speed and amplitude will be effective when performing the osteoporosis assessment. However, it is not possible to measure all the elastic parameters of the propagating medium by measuring the FAS alone and the accuracy of this method is not sufficiently high. To enable estimation of more information about the bone quality, such as the elastic parameters, a technique that analyzes the multimodal ultrasonic guided waves has also been reported (Minonzio et al., 2010; Tran et al., 2014a,b; Xu et al., 2016a,b). For example, the phase velocity of the elastic homogeneous isotropic material is determined using shear wave velocity c_{S}, longitudinal wave velocity c_{L}, and thickness d. That of the transversely isotropic material is characterized by d, three elastic stiffness values and the density. Therefore, these techniques estimate the phase velocity or the wavenumber of the guided waves to determine the properties of the medium. The ultrasonic guided waves are described in detail below in Sect. 1.4.

The estimation of the stiffnesses is important because it related to the porosity of the bone. Granke et al. (2011) revealed the relationship between the elastic properties and the porosity of the cortical bone. They used resonant ultrasound spectroscopy (RUS) and estimated the elastic parameters of the medium accurately. Note, however, that RUS cannot be used in clinical situations or for in-vivo experiments because the technique requires a small cube-shaped target material and involves an invasive process. In Granke et al. (2011), an elastic model of asymptotic homogenization (AH) was used. Given the fact that the investigation was limited to elderly patients, they experimentally showed that the elastic stiffness values of the bone were strongly dependent on the porosity.

The technique that is used to analyze the guided waves uses the frequency range from

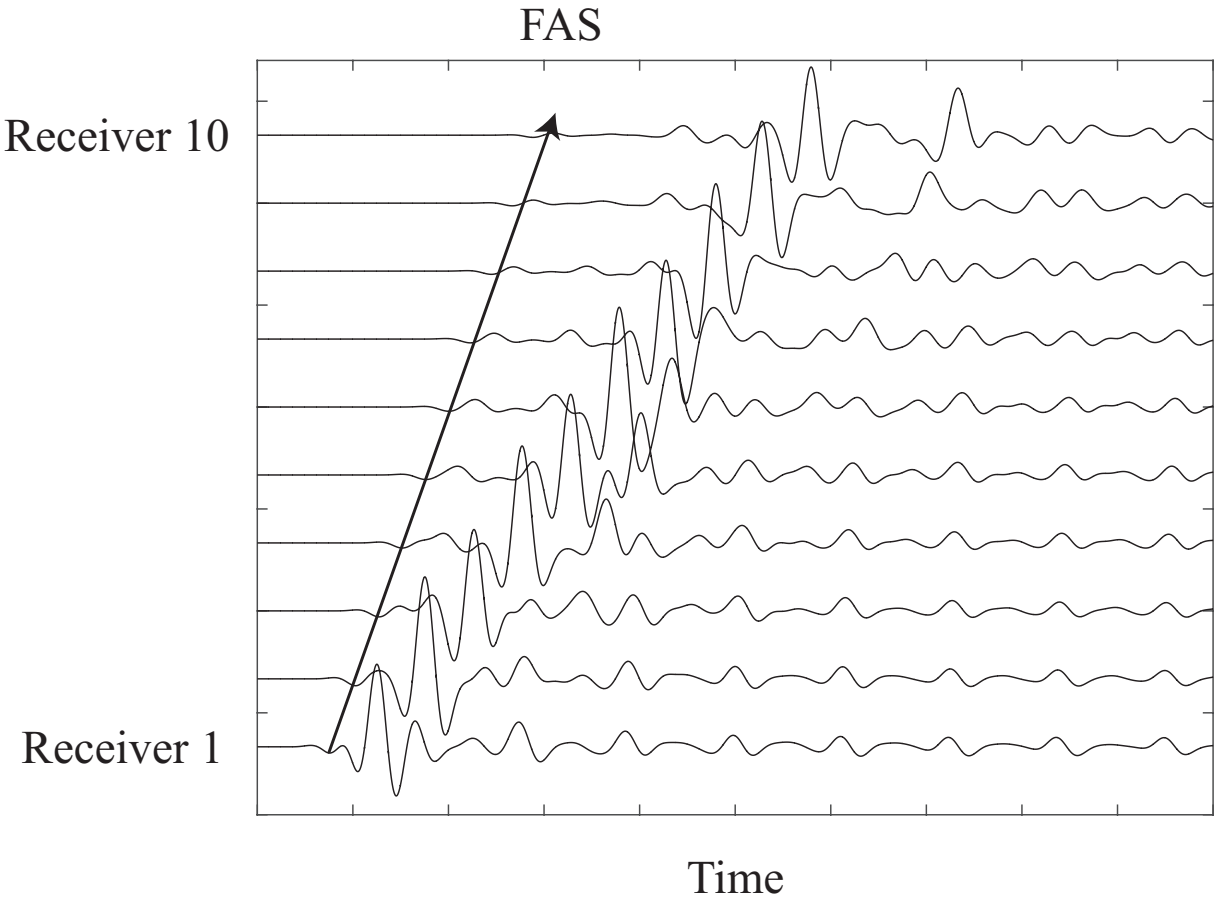

Figure 1.10: Guided waves and first arriving signals.

around 0 to 2.0 MHz, i.e. lower frequency range, because the bone is an absorbing material and shows an almost linear change in attenuation with frequency. In contrast, a method that operates at a center frequency of 3.0 MHz has also been proposed (Suetoshi et al., 2016). This technique does not use the ultrasonic guided waves that propagate inside the bone, but instead uses the leaky longitudinal wave that propagates along the bone's surface. In this scenario, the velocity of the leaky wave approaches that of the longitudinal wave (Rose, 1999). This velocity is called the cortical SOS (cSOS). The cSOS shows correlation with the cortical BMD and the porosity with an absolute value for the regression of more than 0.8 and is thus expected to be used as the new diagnosis index.

Most AT techniques estimate the bone quality based on the assumption that the probe is positioned parallel to the bone surface. However, in realistic situations, the probe tends to be tilted by the tissue. To compensate for the resulting slope, the techniques which use

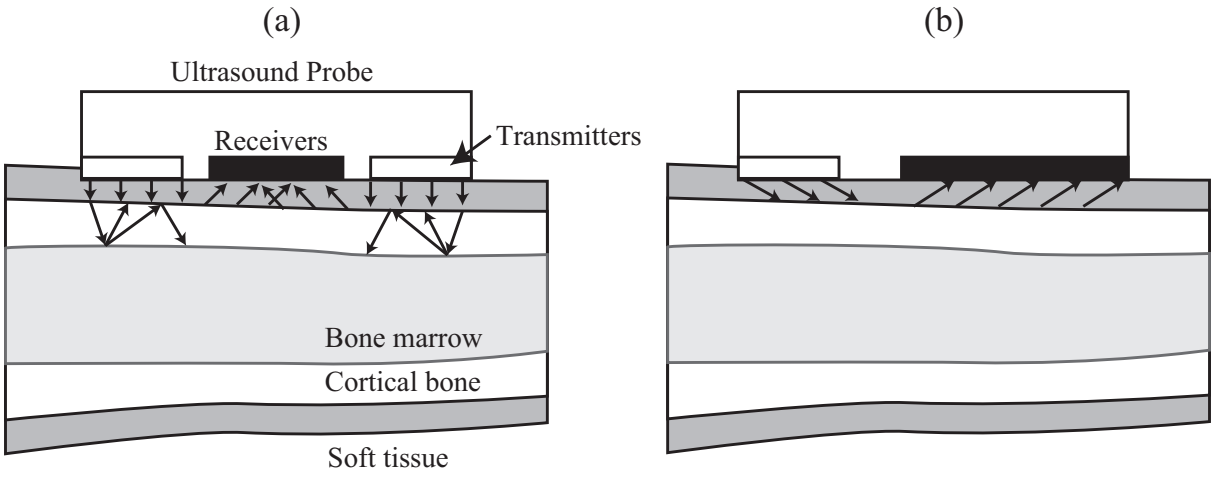

Figure 1.11: Measurement configuration for the AT technique. (a) Bi-directional transmission. (b) Slope compensation with beamforming.

two transmitter array sets and a single receiving array set, as shown in Fig. 1.11(a) have been proposed (Talmant et al., 2009); this method is called the bi-directional method that compensates the effect from tissues by comparing the received signals at two receiving linear arrays. The device that measures the cSOS uses a beamforming technique with the linear array transmitters to estimate and compensate for the slope, as shown in Fig. 1.11(b).

1.4 Ultrasonic guided waves

1.4.1 Theoretical background

Physics

To explain the behavior of the guided waves, we first introduce the basic theory of the physics (Rose, 1999). When we consider a homogeneous isotropic box, as shown in Fig. 1.12, and stretch this box with a stress of σ_{xx}, the strain along the x direction is given through use of the 1D Hooke's law, as follows:

$$\sigma_{xx} = E\varepsilon_{xx}, \tag{1.33}$$

where E is the Young's modulus (the modulus of longitudinal elasticity) and ε_{xx} is the strain along the x direction. The stress along the x direction also causes strain along the y and z directions and this effect is called the Poisson effect.

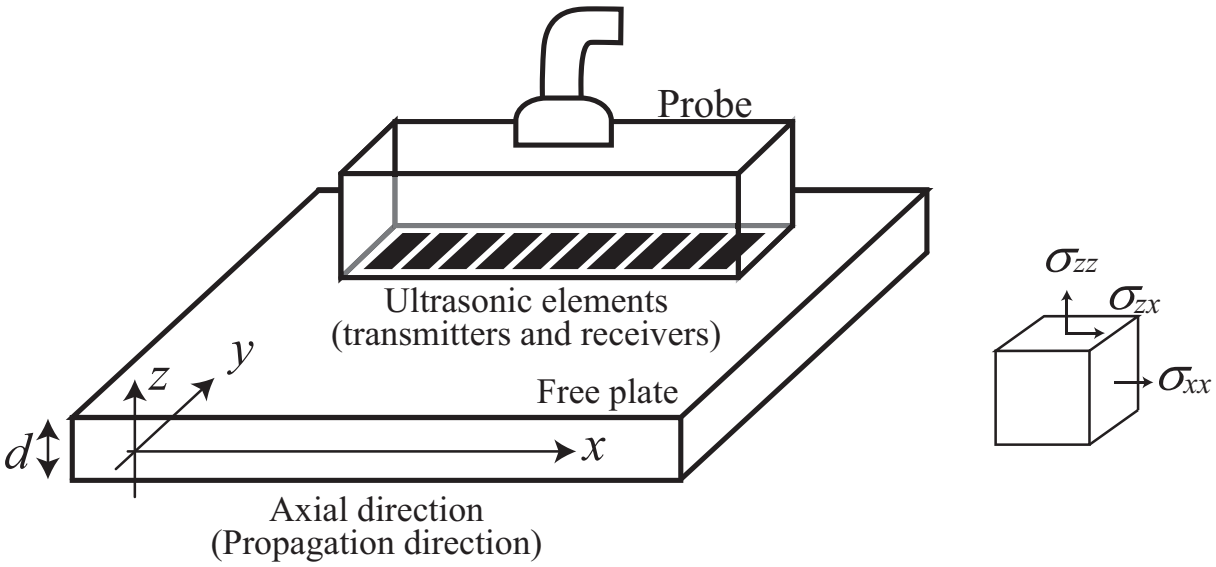

Figure 1.12: Plate model and axis.

When we consider the stresses of σ_{xx}, σ_{yy}, and σ_{zz}, the corresponding strains are given as follows:

$$\varepsilon_{xx} = \{\sigma_{xx} - \xi(\sigma_{yy} + \sigma_{zz})\}/E, \tag{1.34}$$
$$\varepsilon_{yy} = \{\sigma_{yy} - \xi(\sigma_{zz} + \sigma_{xx})\}/E, \tag{1.35}$$
$$\varepsilon_{zz} = \{\sigma_{zz} - \xi(\sigma_{xx} + \sigma_{yy})\}/E, \tag{1.36}$$

where ξ is the Poisson ratio.

The stresses are expressed as follows in a similar manner:

$$\sigma_{xx} = \frac{(1-\xi)\varepsilon_{xx} + \xi(\varepsilon_{yy} + \varepsilon_{zz})}{(1+\xi)(1-2\xi)}E, \tag{1.37}$$
$$\sigma_{yy} = \frac{(1-\xi)\varepsilon_{yy} + \xi(\varepsilon_{zz} + \varepsilon_{xx})}{(1+\xi)(1-2\xi)}E, \tag{1.38}$$
$$\sigma_{zz} = \frac{(1-\xi)\varepsilon_{zz} + \xi(\varepsilon_{xx} + \varepsilon_{yy})}{(1+\xi)(1-2\xi)}E, \tag{1.39}$$

Here, we define the stresses along the transverse (shear) direction, which are given by:

$$\sigma_{ij} = 2\mu_{\mathrm{L}}\varepsilon_{ij}, \tag{1.40}$$

where $i \neq j$ and μ_{L} is the shear modulus (which is also called the Lamé's constant, the modulus of transverse elasticity and the modulus of rigidity).

To expand this basic theory to a generalized material, the stiffness matrix is generally used. This matrix is given by:

$$\begin{bmatrix} \sigma_{xx} \\ \sigma_{yy} \\ \sigma_{zz} \\ \sigma_{yz} \\ \sigma_{zx} \\ \sigma_{xy} \end{bmatrix} = \begin{bmatrix} C_{11} & C_{12} & C_{13} & C_{14} & C_{15} & C_{16} \\ C_{21} & C_{22} & C_{23} & C_{24} & C_{25} & C_{26} \\ C_{31} & C_{32} & C_{33} & C_{34} & C_{35} & C_{36} \\ C_{41} & C_{42} & C_{43} & C_{44} & C_{45} & C_{46} \\ C_{51} & C_{52} & C_{53} & C_{54} & C_{55} & C_{56} \\ C_{61} & C_{62} & C_{63} & C_{64} & C_{65} & C_{66} \end{bmatrix} \begin{bmatrix} \varepsilon_{xx} \\ \varepsilon_{yy} \\ \varepsilon_{zz} \\ \varepsilon_{yz} \\ \varepsilon_{zx} \\ \varepsilon_{xy} \end{bmatrix}, \tag{1.41}$$

where $C_{\{*,*\}}$ is the elastic stiffness coefficient.

The stiffness matrices of a homogeneous isotropic material, such as a copper plate, and a transversely isotropic material, such as cortical bone, are given by:

$$\mathbf{C}_{\mathrm{h}} = \begin{bmatrix} C_{11} & C_{12} & C_{12} & 0 & 0 & 0 \\ & C_{11} & C_{12} & 0 & 0 & 0 \\ & & C_{11} & 0 & 0 & 0 \\ & & & C_{55} & 0 & 0 \\ & & & & C_{55} & 0 \\ & & & & & C_{55} \end{bmatrix} \tag{1.42}$$

$$= \begin{bmatrix} \lambda_{\mathrm{L}}+2\mu_{\mathrm{L}} & \lambda_{\mathrm{L}} & \lambda_{\mathrm{L}} & 0 & 0 & 0 \\ & \lambda_{\mathrm{L}}+2\mu_{\mathrm{L}} & \lambda_{\mathrm{L}} & 0 & 0 & 0 \\ & & \lambda_{\mathrm{L}}+2\mu_{\mathrm{L}} & 0 & 0 & 0 \\ & & & 2\mu_{\mathrm{L}} & 0 & 0 \\ & & & & 2\mu_{\mathrm{L}} & 0 \\ & & & & & 2\mu_{\mathrm{L}} \end{bmatrix}, \tag{1.43}$$

$$\mathbf{C}_{\mathrm{t}} = \begin{bmatrix} C_{11} & C_{12} & C_{13} & 0 & 0 & 0 \\ & C_{11} & C_{13} & 0 & 0 & 0 \\ & & C_{33} & 0 & 0 & 0 \\ & & & C_{55} & 0 & 0 \\ & & & & C_{55} & 0 \\ & & & & & \frac{C_{11}-C_{12}}{2} \end{bmatrix}, \tag{1.44}$$

where $\mathbf{C}_{\mathrm{h}}$ and $\mathbf{C}_{\mathrm{t}}$ are the stiffness matrices of the homogeneous isotropic and transversely isotropic materials, respectively, and λ_{L} is the Lamé's constant. In the homogeneous

isotropic material, λ_{L} and μ_{L} are expressed as follows:

$$\lambda_{\mathrm{L}} = \frac{2\mu_{\mathrm{L}}\xi}{1-2\xi} = \frac{E\xi}{(1+\xi)(1-2\xi)}, \tag{1.45}$$

$$\mu_{\mathrm{L}} = \frac{\lambda_{\mathrm{L}}(1-2\xi)}{2\xi} = \frac{E}{2(1+\xi)}. \tag{1.46}$$

Governing equations in a homogeneous isotropic medium

In this section, we introduce the theories of wave propagation in a homogeneous isotropic medium. The wave equation in the solid is given by Navier's equation, which is expressed as follows:

$$(\lambda_{\mathrm{L}}+\mu_{\mathrm{L}})\nabla(\nabla\cdot\mathbf{u})+\mu_{\mathrm{L}}\nabla^2\mathbf{u} = \rho\frac{\partial\mathbf{u}^2}{\partial t^2}, \tag{1.47}$$

where $\mathbf{u}$ is the particle displacement vector, and ρ is the density of the medium. The particle displacement vector $\mathbf{u}$ in the plate is given by the following equation when using the Helmholtz theorem:

$$\mathbf{u} = \nabla\Phi+\nabla\times\mathbf{H}, \tag{1.48}$$

where Φ is the scalar potential, and $\mathbf{H}$ is the vector potential. The potentials represented by Φ and $\mathbf{H}$ are called the longitudinal and shear wave potentials, respectively (Viktorov, 1967).

By substituting Eq. (1.48) into Eq. (1.47), we obtain the following equation.

$$\nabla\left[(\lambda_{\mathrm{L}}+2\mu_{\mathrm{L}})\nabla^2\Phi-\rho\frac{\partial^2\Phi}{\partial t^2}\right]+\nabla\times\left[\mu_{\mathrm{L}}\nabla^2\mathbf{H}-\rho\frac{\partial^2\mathbf{H}}{\partial t^2}\right]=0. \tag{1.49}$$

As the potential is virtual quantity, Eq. (1.49) does not have a unique solution. It is possible to postulate that they satisfy following relations:

$$\nabla^2\Phi = \frac{\rho}{(\lambda_{\mathrm{L}}+2\mu_{\mathrm{L}})}\frac{\partial^2\mathbf{u}}{\partial t^2}, \tag{1.50}$$

$$\nabla^2\mathbf{H} = \frac{\rho}{\mu_{\mathrm{L}}}\frac{\partial^2\mathbf{u}}{\partial t^2}. \tag{1.51}$$

When we respectively ignore the first and second terms on the right side of Eq. (1.48), we respectively obtain the following two equations:

$$\nabla^2\mathbf{u} = \frac{\rho}{\mu_{\mathrm{L}}}\frac{\partial^2\mathbf{u}}{\partial t^2}, \tag{1.52}$$

$$\nabla^2 \mathbf{u} = \frac{\rho}{(\lambda_{\mathrm{L}} + 2\mu_{\mathrm{L}})} \frac{\partial^2 \mathbf{u}}{\partial t^2}. \tag{1.53}$$

Eqs. (1.52) and (1.53) represent the propagation of the rotational and dilatational waves with velocities of $c_{\mathrm{S}} = \sqrt{\mu_{\mathrm{L}}/\rho} = \sqrt{C_{55}/\rho}$ and $c_{\mathrm{L}} = \sqrt{\lambda_{\mathrm{L}} + 2\mu_{\mathrm{L}}/\rho} = \sqrt{C_{11}/\rho}$, respectively. c_{S} and c_{L} are the shear (or transverse or secondary) wave and longitudinal (or primary or pressure) wave velocities, respectively.

1.4.2 Lamb wave

Lamb wave in a homogeneous isotropic free plate

When we consider an elastic homogeneous isotropic plate with a finite thickness d, as shown in Fig. 1.12, with the wave propagating along the x direction, the components of $\mathbf{u}$ along the x and z directions, u_x and u_z, are given by:

$$u_x = \frac{\partial \Phi}{\partial x} + \frac{\partial H_y}{\partial z}, \tag{1.54}$$

$$u_z = \frac{\partial \Phi}{\partial z} - \frac{\partial H_y}{\partial x}, \tag{1.55}$$

where H_y is the vector potential along the y direction, $u_y = 0$, and $\frac{\partial}{\partial y} = 0$.

The Lamb wave does not depend on the y axis. Therefore, the Lamb wave satisfies the following wave equation.

$$\frac{\partial^2 \Phi}{\partial x^2} + \frac{\partial^2 \Phi}{\partial z^2} - k_{\mathrm{L}}^2 \Phi = 0, \tag{1.56}$$

$$\frac{\partial^2 H_y}{\partial x^2} + \frac{\partial^2 H_y}{\partial z^2} - k_{\mathrm{S}}^2 H_y = 0, \tag{1.57}$$

where $k_{\mathrm{L}} = 2\pi f \sqrt{\rho/(\lambda_{\mathrm{L}} + 2\mu_{\mathrm{L}})} = 2\pi f / c_{\mathrm{L}}$, and $k_{\mathrm{S}} = 2\pi f \sqrt{\rho/\mu_{\mathrm{L}}} = 2\pi f / c_{\mathrm{S}}$.

To satisfy the above wave equation, we can express the solution in the following form:

$$\Phi = \{A_1^{\mathrm{c}} \cos(\sqrt{k_{\mathrm{L}}^2 - k^2} z) + A_2^{\mathrm{c}} \sin(\sqrt{k_{\mathrm{L}}^2 - k^2} z)\} \exp(\mathrm{j}kx), \tag{1.58}$$

$$H_y = \{A_3^{\mathrm{c}} \sin(\sqrt{k_{\mathrm{S}}^2 - k^2} z) + A_4^{\mathrm{c}} \cos(\sqrt{k_{\mathrm{S}}^2 - k^2} z)\} \exp(\mathrm{j}kx), \tag{1.59}$$

where A_1^{c}, A_2^{c}, A_3^{c}, and A_4^{c} are arbitrary constants and k is the wavenumber.

We then solve the equation using the boundary condition where the stress in the z direction at the surface and at the bottom of the plate ($z = \pm d/2$) is zero. Substituting Eqs. (1.54) and (1.55) into Eqs. (1.41) and (1.43) means that the stress is given by the following:

$$\begin{aligned} \sigma_{zz} &= \lambda_{\mathrm{L}} \left(\frac{\partial u_x}{\partial x} + \frac{\partial u_z}{\partial z} \right) + 2\mu_{\mathrm{L}} \frac{\partial u_z}{\partial z}, && (1.60) \\ &= \lambda_{\mathrm{L}} \left(\frac{\partial^2 \Phi}{\partial x^2} + \frac{\partial^2 \Phi}{\partial z^2} \right) + 2\mu_{\mathrm{L}} \left(\frac{\partial^2 \Phi}{\partial z^2} - \frac{\partial^2 H_y}{\partial x \partial z} \right) = 0, && (1.61) \end{aligned}$$

$$\begin{aligned} \sigma_{zx} &= \mu_{\mathrm{L}} \left(\frac{\partial u_x}{\partial z} + \frac{\partial u_z}{\partial x} \right), && (1.62) \\ &= \mu_{\mathrm{L}} \left(2\frac{\partial^2 \Phi}{\partial x \partial z} - \frac{\partial^2 H_y}{\partial x^2} + \frac{\partial^2 H_y}{\partial z^2} \right) = 0, && (1.63) \end{aligned}$$

where strain ε_{zx} is given by $\partial \sigma_z / \partial x$. The direction of $\sigma_{\{*,*\}}$ is shown in Fig. 1.12.

Here, we separately consider the first and second terms of Eqs. (1.58) and (1.59). When we consider the first terms of Eqs. (1.58) and (1.59), we obtain the following equation:

$$\Phi = A_1^{\mathrm{c}} \cos(\sqrt{k_{\mathrm{L}}^2 - k^2} z) \exp(\mathrm{j}kx), \tag{1.64}$$

$$H_y = A_3^{\mathrm{c}} \sin(\sqrt{k_{\mathrm{S}}^2 - k^2} z) \exp(\mathrm{j}kx). \tag{1.65}$$

We see that the displacement which is described by Eq. (1.64) is symmetrical with respect to $z = 0$. Therefore, this mode is called the symmetric (S) mode.

When we substitute Eqs. (1.58) and (1.59) into Eqs. (1.60) and (1.62) with the definition $k_{\mathrm{L}} = 2\pi f \sqrt{\rho/(\lambda_{\mathrm{L}} + 2\mu_{\mathrm{L}})}$, $k_{\mathrm{S}} = 2\pi f \sqrt{\rho/\mu_{\mathrm{L}}}$, i.e., $k_{\mathrm{S}}/k_{\mathrm{L}} = \sqrt{(\lambda_{\mathrm{L}} + 2\mu_{\mathrm{L}})/\mu_{\mathrm{L}}}$, following equations are obtained(Rose, 1999; Viktorov, 1967).

$$\begin{aligned} (k_{\mathrm{S}}^2 - 2k^2) \cos(\sqrt{k_{\mathrm{L}}^2 - k^2} d/2) A_1^{\mathrm{c}} + 2\mathrm{j}k\sqrt{k_{\mathrm{S}}^2 - k^2} \cos(\sqrt{k_{\mathrm{S}}^2 - k^2} d/2) A_3^{\mathrm{c}} &= 0, && (1.66) \\ 2\mathrm{j}k\sqrt{k_{\mathrm{L}}^2 - k^2} \sin(\sqrt{k_{\mathrm{L}}^2 - k^2} d/2) A_1^{\mathrm{c}} - (2k^2 - k_{\mathrm{S}}^2) \sin(\sqrt{k_{\mathrm{S}}^2 - k^2} d/2) A_3^{\mathrm{c}} &= 0, && (1.67) \end{aligned}$$

By using Eqs. (1.66) and (1.67), the following relationship is obtained.

$$(k_{\mathrm{S}}^2-2k^2)^2\cos\left(\frac{\sqrt{k_{\mathrm{L}}^2-k^2}d}{2}\right)\sin\left(\frac{\sqrt{k_{\mathrm{S}}^2-k^2}d}{2}\right) \tag{1.68}$$
$$-4k^2\sqrt{(k_{\mathrm{L}}^2-k^2)(k_{\mathrm{S}}^2-k^2)}\sin\left(\frac{\sqrt{k_{\mathrm{L}}^2-k^2}d}{2}\right)\cos\left(\frac{\sqrt{k_{\mathrm{S}}^2-k^2}d}{2}\right) = 0,$$

We can use the remaining components to obtain the equation for the anti-symmetric (A) mode in a similar manner. Finally, we obtain the following two equations.

$$\frac{\tan(k_\alpha d/2)}{\tan(k_\beta d/2)}+\frac{(k^2-k_\beta^2)^2}{4k_\alpha k_\beta k^2}=0 \quad (\text{S mode}), \tag{1.69}$$

$$\frac{\tan(k_\beta d/2)}{\tan(k_\alpha d/2)}+\frac{(k^2-k_\beta^2)^2}{4k_\alpha k_\beta k^2}=0 \quad (\text{A mode}), \tag{1.70}$$

where $k_\alpha^2=k_{\mathrm{L}}^2-k^2$, $k_\beta^2=k_{\mathrm{S}}^2-k^2$, and $k=(2\pi f)/c$. This relationship is called Rayleigh-Lamb equation.

When we focus on the equation for the S mode (Eq. (1.69)), the numerator of the second term is always positive and has a real value. Therefore, new roots ($k=0$) appear when $k_\alpha d/2=n\pi/2$ and $k_\beta d/2=2n\pi$ ($n=1,2,\cdots$), i.e., these new roots appear when $fd=nc_{\mathrm{S}}$ and $fd=nc_{\mathrm{L}}/2$. These frequencies are called critical frequencies. The corresponding quantities for the A mode can be calculated in the same manner.

As shown in Eqs. (1.69) and (1.70), the solutions to equations k and c at the measurement frequency f are dependent on c_{S}, c_{L}, and d. Therefore, estimation of k or c leads to the estimation of these three parameters.

An example of the phase velocities of the Lamb wave is shown in Fig. 1.13. A and S denote the antisymmetric and symmetric modes, respectively. The numbers denote the propagation orders.

Lamb wave in a viscoelastic plate

In this section, we consider a viscoelastic medium. There are two well-known models for viscoelastic medium: the Maxwell model and the Kelvin-Voight model. The schematic illustrations of these two models are shown in Fig. 1.14. Fig. 1.14(a) and (b) represents Maxwell and Kelvin-Voight model respectively. In the Kelvin-Voight model,

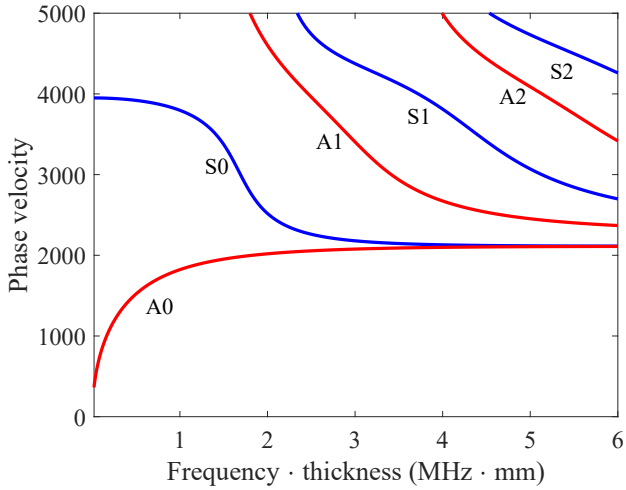

Figure 1.13: Theoretical phase velocities of the Lamb wave.

we consider a spring and a dashpot that are in parallel locations. On the other hand, in the Maxwell model, the dashpot and spring are serially connected. The time constants of these two models are different because the spring of the Maxwell model is directly affected by the stress, where that of the Kelvin-Voight model slowly responds to the stress.

In this thesis, we introduce the Kelvin-Voigt model. The stress at the spring, denoted by σ_1, is given by Hooke's Law as (Rose, 1999):

$$\sigma_1 = E\varepsilon. \tag{1.71}$$

Note that for simplicity here, we consider a 1D problem. At the dashpot, σ_2 is given by Newton's Law as:

$$\sigma_2 = \kappa \frac{d\varepsilon}{dt}, \tag{1.72}$$

where κ is the viscosity. Finally, the total stress is given by $\sigma = \sigma_1 + \sigma_2$. When we consider the wave propagation, σ and ε can then be rewritten as follows:

$$\varepsilon' = \varepsilon e^{j2\pi ft}, \tag{1.73}$$

$$\sigma' = \sigma e^{j2\pi ft}. \tag{1.74}$$

As a result, the total stress can also be rewritten as follows:

$$\begin{aligned} \sigma' &= (E + j2\pi f\kappa)\varepsilon & (1.75)\\ &= C^*\varepsilon, & (1.76) \end{aligned}$$

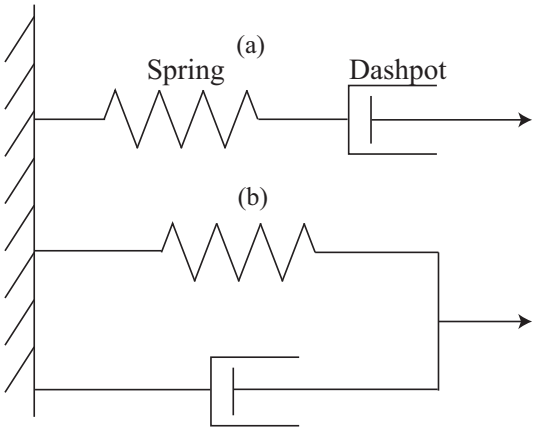

Figure 1.14: Schematic illustration of (a) the Maxwell and (b) the Kelvin-Voigt model.

where C^* represents a modified and complex stiffness. Therefore, when we consider an isotropic viscoelastic plate, the longitudinal and shear wave velocities are given by the following (Naili et al., 2010):

$$c^*_{\mathrm{S,L}} = \sqrt{\frac{C^*_{55,11}}{\rho}} \tag{1.77}$$

$$= \sqrt{\frac{C_{55,11} + \mathrm{j}2\pi f \kappa_{\mathrm{S,L}}}{\rho}}, \tag{1.78}$$

where $c^*_{\mathrm{S,L}}$ are the shear and longitudinal wave velocities with complex components, and $\kappa_{\mathrm{S,L}}$ are the viscosities in the shear and longitudinal directions. As shown in Eq. (1.78), the wave propagation in the viscoelastic medium can be expressed using the same form as that used for the elastic plate but with the complex components.

Along with the stiffness component and the velocities, the wavenumber also has a complex component in the viscoelastic medium.

$$k^* = k - \mathrm{j}\alpha(f), \tag{1.79}$$

where k^* is the modified wavenumber, and $\alpha(f)$ is the frequency-dependent attenuation. As shown in Eq. (1.79), the real and imaginary parts of the wavenumber represent the propagation and the power loss, respectively. Use of the modified wavenumber means that the phase velocity, $c^* = 2\pi f/k^*$, can be written as

$$c^*(f) = \left(\frac{1}{c(f)} - \mathrm{j}\frac{\alpha(f)}{2\pi f} \right)^{-1}. \tag{1.80}$$

When we consider the condition where $(2\pi f) \gg \alpha c$, the modified phase velocity can be rewritten as

$$c^*(f) \approx c + \mathrm{j}\frac{\alpha c^2}{2\pi f}. \tag{1.81}$$

By comparing Eq. (1.78) with Eq. (1.81), the viscosity and the attenuation factor along the shear and longitudinal directions, which are expressed using $\kappa_{\mathrm{S,L}}$ and $\alpha_{\mathrm{S,L}}$, are given by the following:

$$\kappa_{\mathrm{S,L}} = \frac{2\alpha_{\mathrm{S,L}}(f)c_{\mathrm{S,L}}^3\rho}{(2\pi f)^2}. \tag{1.82}$$

As shown in Eq. (1.81), the real part of the phase velocity of the Lamb wave is constant, with a small attenuation that satisfies the condition where $2\pi f \gg \alpha c$. The attenuation component of the Lamb wave is determined by solving the Rayleigh–Lamb equation with the complex wavenumber. Because the real part remains constant, we can solve the Rayleigh–Lamb equation separately. The solution for the Lamb wave in viscoelastic media is given as follows:

$$\frac{\tan(k_\alpha^* d/2)}{\tan(k_\beta^* d/2)} + \frac{(k^{*2} - k_\beta^{*2})^2}{4k_\alpha^* k_\beta^* k^{*2}} = 0 \quad \text{(S mode)}, \tag{1.83}$$

$$\frac{\tan(k_\beta^* d/2)}{\tan(k_\alpha^* d/2)} + \frac{(k^{*2} - k_\beta^{*2})^2}{4k_\alpha^* k_\beta^* k^{*2}} = 0 \quad \text{(A mode)}, \tag{1.84}$$

where $k_\beta^{*2} = (2\pi f)^2/c_{\mathrm{S}}^{*2} - k^{*2}$, $k_\alpha^{*2} = (2\pi f)^2/c_{\mathrm{L}}^{*2} - k^{*2}$, $k^* = (2\pi f)/c - \mathrm{j}\alpha(f)$, $c_{\mathrm{S}}^{*2} = c_{\mathrm{S}}^2 + \mathrm{j}(2\pi f)\kappa_{\mathrm{s}}/\rho$, and $c_{\mathrm{L}}^{*2} = c_{\mathrm{L}}^2 + \mathrm{j}2\pi f\kappa_{\mathrm{L}}/\rho$.

Coupling effects of fluids

When we consider bone with soft tissue, we need to consider the coupling effect between the two. When compared with the bone, the attenuation and elasticity properties of the soft tissue are both small and can be neglected; thus, in this section, we regard the soft tissue as water.

When we consider the existence of the water layer between the plate and the probe, the number of modes increases because the numbers of multiple reflections and multiple refractions also increase.

The theoretical model is given in Yapura and Kinra (1995). Fig. 1.15 shows a comparison between the phase velocities of the single elastic plate and the elastic plate with a water layer. The parameters used in the calculations are follows: $c_{\mathrm{L}} = 4650$ m/s,

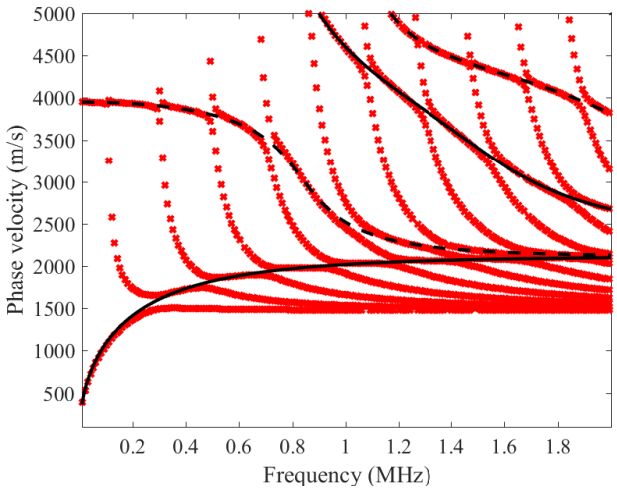

Figure 1.15: Coupling effects of the water. The red cross marks represent the phase velocity of the water with the plate. The black solid and dotted lines that respectively represent the A and S mode show the phase velocity of the single isotropic plate.

$c_S = 2260$ m/s, plate thickness $d = 2$ mm and the water layer thickness is 2 mm. The densities of the plate and the water are 8.94 and 1.0 g/cm^3, respectively.

As shown in Fig. 1.15, some modes have almost the same phase velocities as the single plate; however, several additional modes appear when the coupling effects are considered.

1.5 Theory of adaptive beamforming techniques

In this section, we introduce the conventional non-adaptive and adaptive beamforming techniques.

1.5.1 Signal model

When we consider M wide-band signals with multiple different directions of arrival (DOA), the received signal at the n-th linear array receiver with the receiver pitch of Δl

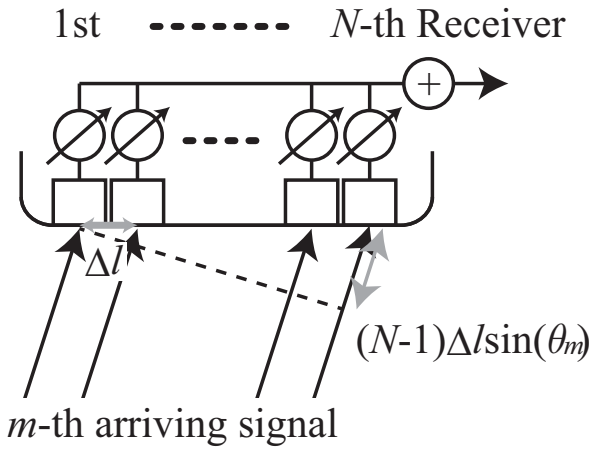

Figure 1.16: Signal model and adaptive signal processing.

is given in the time and frequency domains by:

$$s_n(t) = \sum_{m=1}^{M} s_1(t-(n-1)\Delta l \sin(\theta_m)/c), \tag{1.85}$$

$$S_n(f) = S_1(f) \sum_{m=1}^{M} \exp(-\mathrm{j}2\pi f(n-1)\Delta l \sin(\theta_m)/c), \tag{1.86}$$

where $s_n(t)$ and $S_n(f)$ are the respectively time and frequency domain signals at n-th receiver, θ_m is the direction of arrival of the m-th wave, see Fig. 1.16. Note that t again denotes the time along the range domain, i.e., the measurement depth, range, or distance, and r is given by $r = ct/2$.

When we assume that the signal is a narrow-band signal with a center frequency of f_0, the signal in the time domain can be re-defined as an analytic signal as:

$$s_n(t) = s_1(t) \sum_{m=1}^{M} \exp(-\mathrm{j}2\pi f_0(n-1)\Delta l \sin(\theta_m)/c), \tag{1.87}$$

$$= s_1(t) \sum_{m=1}^{M} a_n(\theta_m), \tag{1.88}$$

where a_n is the steering value at the n-th receiver.

1.5.2 Narrow band beamforming

Initially, we introduce the conventional narrow-band DAS beamforming technique. This is equivalent to a time-delay process that is used to form a focal point from a narrow-

band signal.

$$P_{\mathrm{DAS}}(\theta) = |\mathbf{a}^{\mathrm{H}}(\theta)\mathbf{s}|^2, \tag{1.89}$$

where $\mathbf{s} = [s_1 \cdots s_N]^{\mathrm{T}}$ is a signal vector, $\mathbf{a}(\theta) = [a_1(\theta) \cdots a_N(\theta)]^{\mathrm{T}}$ is a steering vector, and N is the number of receivers. Here, $(\cdot)^{\mathrm{H}}$ and $(\cdot)^{\mathrm{T}}$ denote the matrix conjugate transposition and matrix transposition, respectively.

Next, we introduce a classical adaptive beamforming technique called the Capon method (Capon, 1969). The Capon method is an adaptive signal processing method that suppresses the interference contribution by calculating an optimal weighting vector, as shown below. The schematic illustration is shown in Fig. 1.17(a).

$$\min_{\mathbf{W}}(P_{\mathrm{out}} = \frac{1}{2}\mathbf{W}^{\mathrm{H}}\mathbf{R}\mathbf{W}) \text{ subject to } \mathbf{a}^{\mathrm{T}}(\theta)\mathbf{W}^{*} = 1, \tag{1.90}$$

where $\mathbf{R}$ is a covariance matrix and $\mathbf{W}$ is a weighting vector. This problem can then be solved using the Lagrange multiplier methodology.

The estimated spectrum as shown in Fig. 1.17(b), denoted by $P(\theta)$, is given by:

$$P(\theta) = \frac{1}{\mathbf{a}^{\mathrm{H}}(\theta)\mathbf{R}^{-1}\mathbf{a}(\theta)}. \tag{1.91}$$

To enable use of the adaptive beamforming technique, it is necessary to estimate the covariance matrix. The conventional estimate of this matrix is expressed as follows:

$$\mathbf{R} = \mathrm{E}[\mathbf{s}\mathbf{s}^{\mathrm{H}}], \tag{1.92}$$

where E represents the averaging process for the ensemble average. To obtain the ensemble average, individual data samples are required. When the signals are incoherent, the ensemble average can be achieved by time-averaging of the snapshots under the assumption of ergodicity (Hashimoto et al., 2016).

1.5.3 Beamforming techniques for B-mode imaging

Comparison of radio wave imaging with ultrasound imaging

When we apply adaptive beamforming techniques that were originally designed for radio wave sensing applications to medical ultrasound signals, it is very important to consider the differences between the two signals.

First, the propagation speeds of the two waves are quite different. The speed of light (for the radio waves) is 299792458 m/s, whereas the speed of sound in water and in soft tissue is approximately 1500 m/s and the corresponding speed in bone is approximately

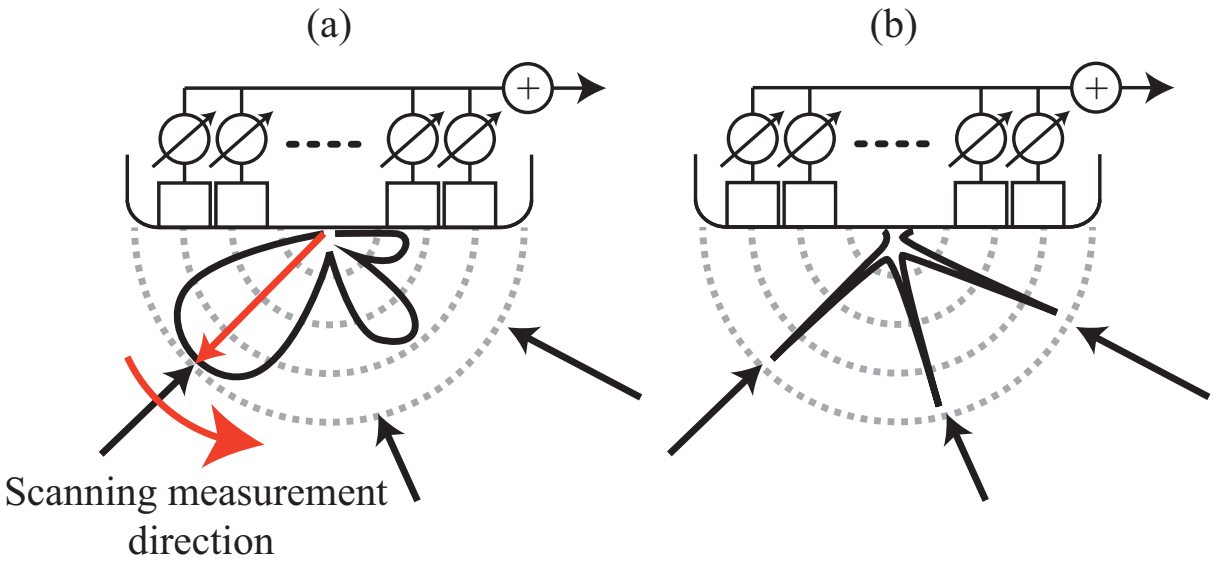

Figure 1.17: Schematic illustration of the Capon method. (a) Interference suppression using optimized weighting vector. (b) Estimated spectrum.

3000 m/s (Laugier and Haïat, 2011). Second, the fractional bandwidths that are used for these measurements are also different. The fractional bandwidth employed for the radio wave is usually less than 10% (Fukao et al., 1985; Sakamoto et al., 2016), whereas that employed for the medical ultrasound signal is normally more than 50% (Moghimirad et al., 2016). In medical 2D ultrasound imaging in particular, wider bands with bandwidths of more than 100% of the signal bandwidth are sometimes used to improve the range resolution. Finally, the signal type is different. In some applications of radio wave measurements such as wind velocity estimation, the desired and undesired signals are independent of the measurement time and are not correlated. Therefore, time-averaging for covariance matrix estimation is generally effective. In contrast, in most ultrasound imaging applications, the time-averaging process is not appropriate because the target is stable, high-frame-rate imaging is required, and/or the desired signals and undesired signals are strongly correlated. To estimate the covariance matrix accurately, spatial averaging, which is introduced below, is thus required in most ultrasound imaging applications apart from Doppler velocity measurements.

Covariance matrix estimation for coherent signals

In addition to ultrasound imaging, measurement of coherent signals is sometimes required in radio wave measurements, e.g., when the undesired signal is a multi-path ver-

sion of the desired signal, these signals are strongly correlated.

To overcome this problem, the sub-array (spatial) averaging technique has been proposed (Takao and Kikuma, 1987). The spatial averaging technique situates small sub-arrays within the larger array and averages the signals to suppress their correlations.

$$\mathbf{R}_{\mathrm{A}} = \frac{1}{N_{\mathrm{ave}}} \sum_{n=1}^{N_{\mathrm{ave}}} \mathbf{R}_n, \tag{1.93}$$

$$\mathbf{R}_n = \mathbf{s}_n \mathbf{s}_n^{\mathrm{H}}, \tag{1.94}$$

where $\mathbf{R}_{\mathrm{A}}$ is an averaged covariance matrix, $\mathbf{s}_n = [s_n \cdots s_{n+N_{\mathrm{sub}}-1}]$, N_{sub} is the sub-array size, and N_{ave} is the number of averaging steps. The number of receivers contained in the full-size array is $N = N_{\mathrm{sub}} + N_{\mathrm{ave}} - 1$.

This process can be used to estimate the covariance matrix accurately because we do not need to assume ergodicity in this case. However, we sacrifice the image resolution because the aperture size of the array is reduced from $N = N_{\mathrm{sub}} + N_{\mathrm{ave}} - 1$ to N_{sub} when using this process. The accuracy of the covariance matrix estimation is dependent on the number of averaging steps, and thus there is a trade-off between the image resolution determined using a sub-array of size N_{sub} and the accuracy of the covariance matrix estimation, which is determined by the number of averaging steps N_{ave}, see Fig. 1.18.

Wide-band Capon method

As shown in Eqs. (1.90) and (1.91), the original Capon method assumes that the signal is a narrow-band signal. The constraint condition used in the Capon method was designed for narrow-band signals and cannot constrain wide-band signals. Therefore, to approximate the narrow-band signal, a time-delay process is used (Synnevåg et al., 2009), see Fig. 1.19.

When the time-delay process that forms a focal point at the measurement point is used, the constraint vector does not include the phase rotation with the narrow-band assumption. The estimated spectrum at measurement point (x,z), $P(x,z)$, is then given by:

$$P(x,z) = \frac{1}{\mathbf{1}^{\mathrm{T}} \mathbf{R}_{\mathrm{AD}}^{-1}(x,z) \mathbf{1}}, \tag{1.95}$$

where $\mathbf{1} = [1 \cdots 1]$ and $\mathbf{R}_{\mathrm{AD}}(x,z)$ is the covariance matrix that is formed from the signal after the time-delay and spatial averaging process. Note that use of the time-delay process can also help to overcome the differences between the near-field calculations and the far-field calculations.

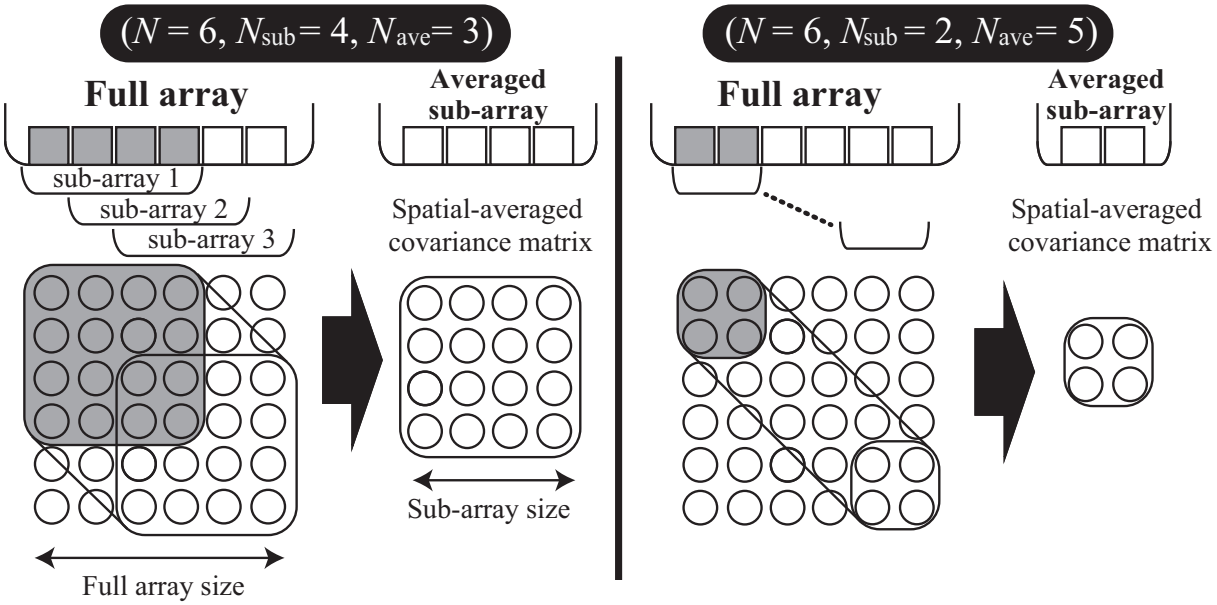

Figure 1.18: Schematic illustration of the spatial averaging technique with two examples. $(N, N_{\mathrm{sub}}, N_{\mathrm{ave}}) = (6,4,3)$ and $(N, N_{\mathrm{sub}}, N_{\mathrm{ave}}) = (6,2,5)$.

Fig. 1.20 shows a comparison of the DOA spectra of the narrow-band and wide-band Capon methods with conventional non-adaptive beamforming techniques. We assume that these signals arrived with DOAs of 0 and 20 degrees, respectively. In the narrow-band DAS technique, we compensate the phase rotation at the center frequency. The fractional bandwidths of the narrow and wide-band signals are 1% and 50%, respectively.

When we apply the adaptive and non-adaptive beamforming techniques to narrow-band signals, the adaptive beamforming technique can estimate the DOA accurately with high resolution. However, when we apply the conventional adaptive beamforming technique to a wide-band signal, the resolutions that can be determined decrease severely.

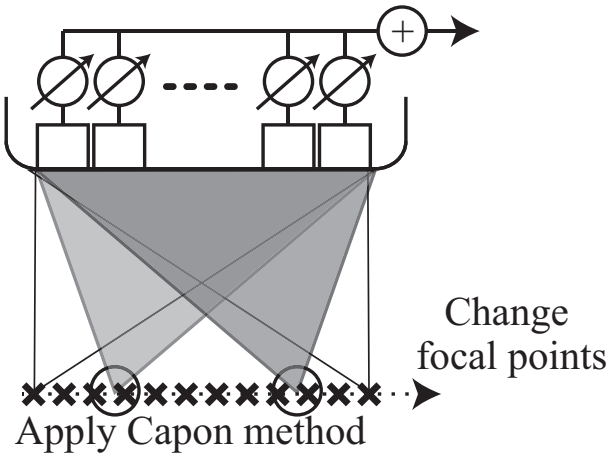

Figure 1.19: Schematic illustration of the Capon method for wide-band signals.

1.5.4 Beamforming techniques for axial transmission

In this subsection, we introduce the similarities between medical ultrasound imaging and the AT technique from a signal processing viewpoint. The signal model for the AT technique is given by:

$$S_n(f) = S_1(f) \sum_{m=1}^{M} \exp(-\mathrm{j}2\pi f(n-1)\Delta l / c_m(f)), \tag{1.96}$$

where c_m is the phase velocity of the m-th propagation wave, see Fig. 1.21. Comparison of Eqs. (1.85) and (1.96) shows that the forms of these equations are very similar. Therefore, to estimate the phase velocity or the wavenumber of the guided waves, we can use a straightforward beamforming technique.

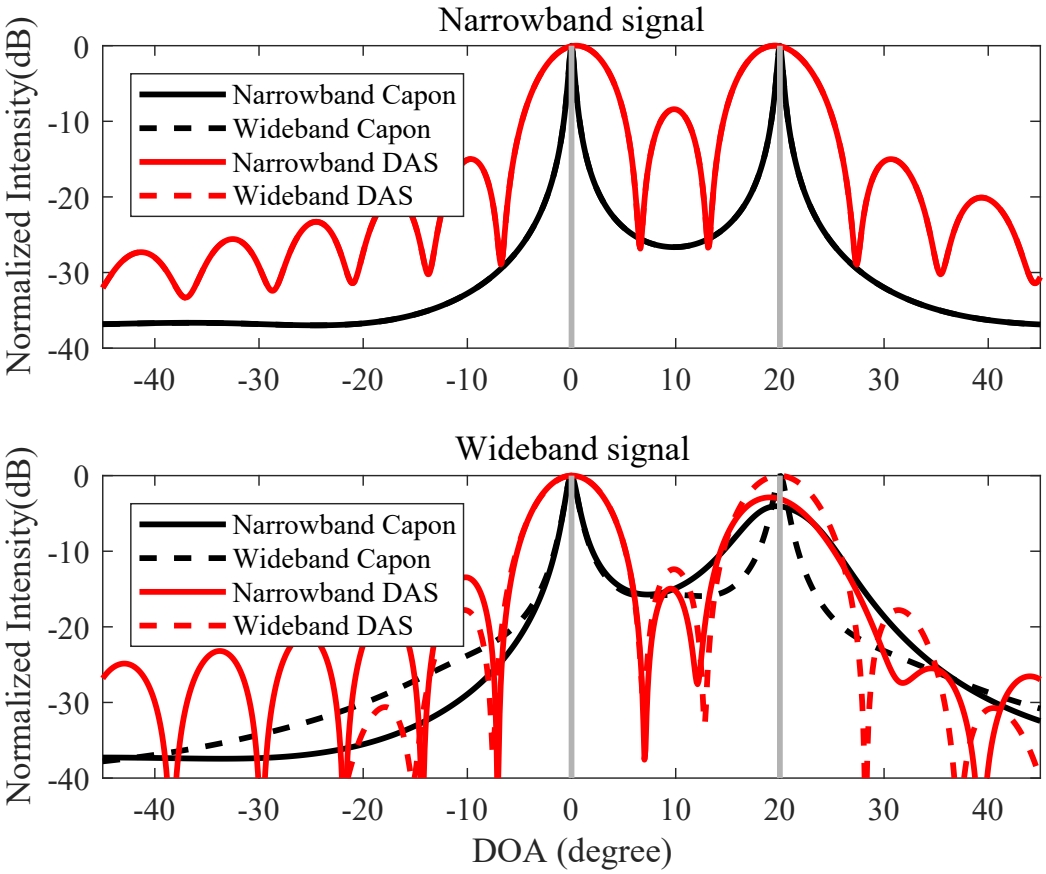

Figure 1.20: Performance dependences of beamforming techniques on the received signal bandwidth. The fractional bandwidths of the narrow and wide band signals are 1% and 50%, respectively.

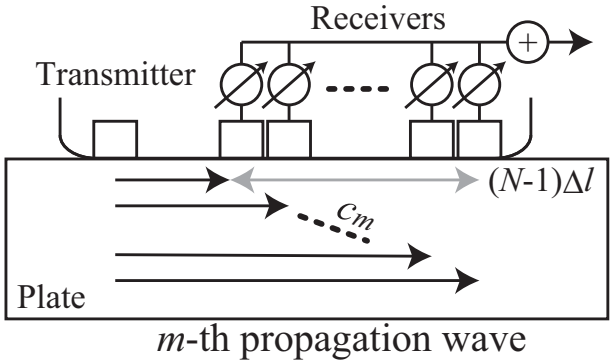

Figure 1.21: Schematic illustration of the adaptive beamforming technique for axial transmission technique.

Chapter 2

Computational complexity reduction techniques for real-time and high-resolution medical ultrasound imaging using the beam-space Capon method

2.1 Introduction

In Sect. 1.5.3, we introduced the wide-band Capon method. The Capon method is effective to improve the lateral (Synnevåg et al., 2009) and depth resolution (Taki et al., 2013, 2012). However, the computational complexity of the method for lateral resolution improvement is high and do not suitable for the real-time imaging.

The conventional Capon method for ultrasound imaging is based on element-space (ES) signal processing (Mehdizadeh et al., 2012; Synnevåg et al., 2009; Wang et al., 2005). As shown in Eq. (1.95), ES signal processing requires the inversion of large matrices, such as 64×64, many times, which severely increases the complexity. To reduce the complexity associated with calculating inverse matrices, the beam-space (BS) Capon method has been reported (Nilsen and Hafizovic, 2009; Okumura et al., 2015a,b).

The method uses a few orthogonal beams to reduce the matrix size. The BS Capon method reduces complexity compared with the original ES Capon method. However, further reduction is required for real-time imaging. Because ultrasound imaging typically employs wide-band signals, both ES and BS Capon methods employ a large number of time-delay processes to create focal points in the region of interest (ROI) and to estimate the covariance matrix. In addition, compared with the ES Capon method, the BS Capon method requires an additional calculation associated with the transforma-

tion from ES signal processing to BS signal processing (Nilsen and Hafizovic, 2009). To achieve real-time imaging, reductions are required in the number of the above-mentioned processes.

When the time-delay value to generate a focal point is small, the time-delay process can be approximated by multiplying a steering vector with a covariance matrix (Okumura et al., 2015a). Thus, we propose a method that reduces the number of processes by using this approximation. Additionally, an accurate estimation of the intensity is required in medical ultrasound imaging. The spatial averaging technique is widely employed to stabilize the estimation of the intensity when using the Capon method (Kimura et al., 2009; Takao and Kikuma, 1987; Taki et al., 2013, 2015b). A larger sub-array size N_{sub} achieves higher resolution and low stability, whereas a smaller N_{sub} achieves lower resolution and high stability. Therefore, we first employ a larger N_{sub} for high-resolution imaging and estimate the position at which the target should exist. Next, we use a smaller N_{sub} to compensate the intensity. In this work, to evaluate the proposed method, we conducted a numerical simulation and an experiment.

2.2 Materials and methods

2.2.1 Original beam-space Capon method for medical ultrasound imaging

We introduce the original BS Capon method for medical ultrasound imaging that is the basis of the proposed method (Nilsen and Hafizovic, 2009). The BS method first multiplies the Butler matrix, $\mathbf{B}$, to the signal vector after a time-delay process, $\mathbf{s}_{\mathrm{d}}(t)$, to form orthogonal beams. Because the spatial energy distribution of transmitted ultrasound is determined by the position of the transmitted beam, we can select a few useful beams that contain signals returned from the desired direction, see Fig. 2.1 (Nilsen and Hafizovic, 2009; Okumura et al., 2015a,b). When we use a N-element linear array with the element pitch of a half-wavelength at the center frequency, the received signal vector in the BS, $\mathbf{s}_{\mathrm{BS}}(t)$, is given by

$$\mathbf{s}_{\mathrm{BS}}(t) = \mathbf{B}\mathbf{s}_{\mathrm{d}}(t), \tag{2.1}$$

$$\mathbf{B} = [\mathbf{b}_{-(N_{\mathrm{b}}-1)/2} \cdots \mathbf{b}_0 \cdots \mathbf{b}_{(N_{\mathrm{b}}-1)/2}]^{\mathrm{T}}, \tag{2.2}$$

$$[\mathbf{b}_q]_p = \exp(\mathrm{j}2\pi pq/N)/\sqrt{N}, \tag{2.3}$$

where N_b is the number of the selected beams, p, q are the element indexes of the matrix, and $(\cdot)^\mathrm{T}$ denotes the transpose. In this chapter, we assume N is an even number and use $N_\mathrm{b} = 3$ to follow previous studies (Nilsen and Hafizovic, 2009; Okumura et al., 2015a,b).

The BS Capon method then computes the optimal weighting vector by solving

$$\min(P_\mathrm{out} = \mathbf{W}_\mathrm{BS}^\mathrm{H}\mathbf{R}_\mathrm{ABS}\mathbf{W}_\mathrm{BS}/2) \text{ subject to } \mathbf{W}_\mathrm{BS}^\mathrm{H}\mathbf{a}_\mathrm{B} = 1, \tag{2.4}$$

$$\mathbf{R}_\mathrm{ABS} = \mathbf{B}_\mathrm{s}\mathbf{R}_\mathrm{AD}\mathbf{B}_\mathrm{s}^\mathrm{H}, \tag{2.5}$$

$$\mathbf{a}_\mathrm{B} = \mathbf{B}_\mathrm{s}[1\cdots 1]^\mathrm{T}, \tag{2.6}$$

where P_out is the output power of the BS Capon, $\mathbf{W}_\mathrm{BS}$ is the BS weighting vector, $(\cdot)^\mathrm{H}$ denotes the Hermitian transpose, $\mathbf{B}_\mathrm{s}$ is the Butler matrix for the sub-array, $\mathbf{a}_\mathrm{B}$ is the steering vector for BS Capon method, $\mathbf{R}_\mathrm{AD}$ is the covariance matrix after spatial averaging and time-delay processes which is introduced in Sect. 1.5.3, and $\mathbf{R}_\mathrm{ABS}$ is the covariance matrix in the BS. The output power is expressed as

$$P_\mathrm{out} = 1/\left\{\mathbf{a}_\mathrm{B}^\mathrm{H}(\mathbf{R}_\mathrm{ABS} + \eta\mathbf{I})^{-1}\mathbf{a}_\mathrm{B}\right\}, \tag{2.7}$$

where η is the diagonal loading (DL) factor used to stabilize the estimated intensity and $\mathbf{I}$ is the identity matrix. The DL factor determines the sensitivity of the Capon method. When we use a large DL factor, the output power approaches that of the DAS technique. Conversely, a small DL factor results in a high-resolution image and a large estimation error of the output power.

Compared with the ES Capon method, the BS method reduces the computational complexity associated with the inversion of the covariance matrix. However, additional reduction of complexity is desired for clinical use. In addition, both accurate estimation of intensity and high-resolution imaging are required. We thus employ the following three steps.

2.2.2 Computational cost reduction using a steering vector

To reduce the computational complexity, we replace the time-delay process by the multiplication of a steering vector with an estimated covariance matrix. We first divide the ROI into sub-ROIs, as shown in Fig. 2.2. The output powers at the measurement points in a sub-ROI are estimated using a covariance matrix at the center of the sub-ROI with steering vectors. That is, we approximate the time-delay process that is focused on the

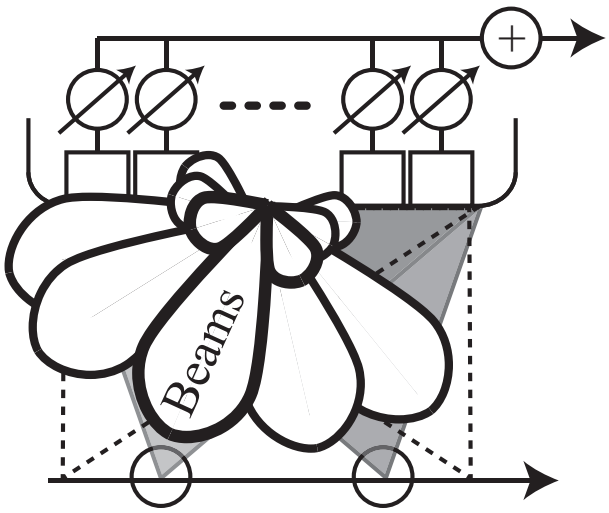

Figure 2.1: Schematic illustration of the BS Capon method.

measurement point with a steering vector and time-delay processes that is focused at the center of the sub-ROI.

The output power at (x,z) in sub-ROI i, $P_{\mathrm{out}i}(x,z)$, is estimated by the proposed BS Capon method using the steering vector $\mathbf{a}'_i(x,z)$:

$$P_{\mathrm{out}i}(x,z) = 1/\left\{\mathbf{a}'_i(x,z)^{\mathrm{H}}(\mathbf{R}_{\mathrm{ABS}}(x_{\mathrm{f}i},z)+\eta\mathbf{I})^{-1}\mathbf{a}'_i(x,z)\right\}, \tag{2.8}$$

$$\mathbf{C}'_i(x,z) = \mathbf{B}[\exp(\mathrm{j}\theta_1)\cdots\exp(\mathrm{j}\theta_{N_{\mathrm{sub}}})]^{\mathrm{T}}, \tag{2.9}$$

$$\theta_m = 2\pi f_0(r_{i,n}-r_{x,n})/c, \tag{2.10}$$

where $\mathbf{R}_{\mathrm{ABS}}(x_{\mathrm{f}i},z)$ is the covariance matrix when the beam is focused at the center of the sub-ROI $(x_{\mathrm{f}i},z)$, i is the sub-ROI index, c is the speed of sound, f_0 is the center frequency, and $r_{i,n}$ and $r_{x,n}$ are the distances from the n-th element in the sub-array to the focal points $(x_{\mathrm{f}i},z)$ and (x,z), respectively. When we reduce the number of time-delay processes, the transformation from ES signal processing to BS signal processing is also simplified because we can reuse the BS covariance matrix in the sub-ROI.

Because the steering vector $\mathbf{C}'_i$ compensates for the phase rotation at the center frequency, the large distance from the focal point to the measurement point $r_{i,n}-r_{x,n}$ should deteriorate the image quality of the proposed method. As shown in Fig. 2.2, we mitigate the deterioration with a filter, $w_i(x)$, that amplifies the output power calculated at the

center of the sub-ROI:

$$
\begin{aligned}
w_i(x) &= \{\sin[3\pi(x-x_{\mathrm{f}i})/x_{\mathrm{s}}+\pi]+1\}/4 \text{ for } x_{\mathrm{f}i}-x_{\mathrm{s}}/2 \le x \le x_{\mathrm{f}i}-x_{\mathrm{s}}/6, && (2.11)\\
w_i(x) &= 0.5 \text{ for } x_{\mathrm{f}i}-x_{\mathrm{s}}/6 \le x \le x_{\mathrm{f}i}+x_{\mathrm{s}}/6, && (2.12)\\
w_i(x) &= \{\sin[3\pi(x-x_{\mathrm{f}i})/x_{\mathrm{s}}]+1\}/4 \text{ for } x_{\mathrm{f}i}+x_{\mathrm{s}}/6 \le x \le x_{\mathrm{f}i}+x_{\mathrm{s}}/2, && (2.13)\\
w_i(x) &= 0 \text{ for else}, && (2.14)
\end{aligned}
$$

where x_{s} is the sub-ROI size and the interval of $x_{\mathrm{f}i}$ is $x_{\mathrm{s}}/3$. In this chapter, we set the distance threshold, $x_{\mathrm{s}}/3$, to be is almost equal to the main beam width.

The output power with the filter, $P'_{\mathrm{out}i}(x,z)$, is given by

$$
P'_{\mathrm{out}}(x,z) = \sum_{i=1}^{N_{\mathrm{R}}} w_i(x) P_{\mathrm{out}i}(x,z), \tag{2.15}
$$

where N_{R} is the number of sub-ROIs.

2.2.3 Sensing target position with peak detection and refocusing

Since the large distance from the focal point to the measurement point causes false images, we must make new focal points and recalculate the intensity at positions nearer to where the targets exist. To select the points, we first search the peaks in $P'_{\mathrm{out}r}(x,z)$ because the target is most likely to exist at a position where the estimated intensity is high. In this chapter, we select peaks where the slopes of the peaks exceed the threshold $\varepsilon_{\mathrm{th}}$.

The false image may appear near the actual target position. Thus, when the lateral distance of adjacent peaks is less than a threshold distance, x_{c}, we consider the peaks to be originating from a single target and these peaks are classified into the same cluster. After clustering, we designate a focal point at the center of each cluster and recalculate the intensity at $x_l - x_{\mathrm{re}}/2 < x_l < x_l + x_{\mathrm{re}}/2$, where x_l is the position of the center of the cluster l and x_{re} is the lateral length of recalculation. If the peaks appear again in the region of recalculation, the targets are assumed to exist at the peaks' positions.

2.2.4 Power compensation technique

In the previous step, we estimated the target position, x_k, accurately. In the next step, we acquire an accurate approximation of the intensity at x_k. When a small N_{sub} is used for the Capon method, the output power approaches the intensity estimated by DAS method

(Kimura et al., 2009; Takao and Kikuma, 1987; Taki et al., 2013, 2015b). Because the large distance from the focal point to the measurement point also deteriorates the accuracy of intensity estimation, we set focal points at all x_k. Then we calculate the output power using a small sub-array size for power compensation N'_{sub}, that is, a large N_{ave}. Finally, we linearly interpolate the intensity of the measurement points $P'_{\mathrm{out}}(x)$ in the range of $x_k - x_{\mathrm{c}} < x < x_k + x_{\mathrm{c}}$, where we adjust the intensity at the target position to the above-mentioned estimated intensity.

2.2.5 Simulation settings

To demonstrate the effectiveness of the proposed method, we used a numerical simulation employing the Field II simulation package (Jensen, 1996; Jensen and Svendsen, 1992). We used a 96-element probe with a center frequency of 2.0 MHz and a fractional bandwidth of 50% to simulate the experimental setting. The element pitch was half of the wavelength at the center frequency, that is, 0.375 mm. The two scatterers were positioned at depths of 20 and 50 mm with a lateral interval of 1.0 mm. The lateral pixel size Δx was 0.050 mm and threshold $\varepsilon_{\mathrm{th}}$ was 0.02 W/mm, where the intensity was normalized to the highest intensity. The lateral imaging width was from -3.0 to 3.0 mm. The sub-ROI size, x_{s}, was 2.25 mm, the length for recalculation, x_{re}, was 0.55 mm, and the length for clustering, x_{c}, was 0.30 mm. The distance threshold, $x_{\mathrm{s}}/3$, was almost equal to the main-lobe width at the depth of 35 mm. The sub-array size for imaging, N_{sub}, and the sub-array size for compensation, N'_{sub}, were 64 and 32, respectively, and the DL factors for imaging, η, and compensation were -60 and -40 dB of the received signal intensity, respectively.

2.2.6 Experimental settings

We conducted an experimental study to investigate the performance of the proposed method. Figs. 2.3(a) and (b) show a photograph and a schematic of the experimental system, respectively. We placed two copper wire targets with a lateral interval of 1.0 mm in a water tank. The diameter of the wire was 0.20 mm. For simplicity, we evaluated the performance of the proposed technique in a 2D problem. We used a JPR 10-CN (Japan Probe, Tokyo, Japan) ultrasound device that can export raw RF data (Taki et al., 2015c). The sampling frequency was 20 MHz. Because the JPR 10-CN that exports the RF data uses two separate elements to transmit and receive, we employed the STA technique to simulate plane wave transmission (Hasegawa and Kanai, 2012; Jensen et al., 2006; Takahashi et al., 2014). We changed the target depth by scanning down the probe. Fig. 2.3(b) shows the data-acquisition procedure. The target depths were 21, 31, 41, and 51

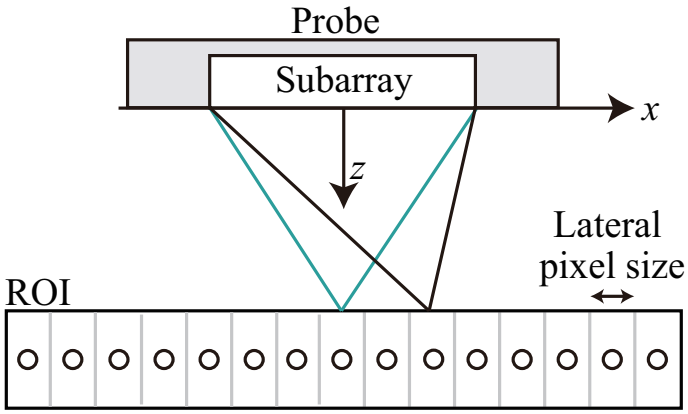

Figure 2.2: Schematic illustration of proposed method.(Reproduction from Okumura et al. (2016); Copyright(2016) The Japan Society of Applied Physics.)

mm. The conventional BS Capon method employed a sub-array size of 64 and DL factor of -40 dB to follow the conventional study (Taki et al., 2015b). The ROI size at each scanning depth was 15 mm $\times$ 10.4 mm. The other parameters are the same as those used in the numerical simulation study.

We evaluated the proposed method using five indicators: the first side-lobe level, the -6 dB beam width, the intensity estimation error, the number of operations, and the calculation time. The first side-lobe level was calculated from the intensity at the center of the two wire targets. The -6 dB beam width is the lateral width of the region centered on the target position where the estimated intensity has decreased by less than -6 dB relative to the estimated peak intensity. The intensity estimation error was calculated as the difference between the estimated intensity and the intensity estimated using the DAS method at the target position. We dismissed the running time of loading the experimental data. In the evaluation, we averaged the first side-lobe level, -6 dB beam width, and the intensity estimation error at each lateral position where the estimated intensity is highest in the ROIs.

2.3 Simulation and experimental results

2.3.1 Simulation results

The intensities estimated by the DAS method and the proposed method at the depths of 20 and 50 mm are shown in Figs. 2.4(a) and (b). The dotted lines shown in Fig. 2.4 are the estimated intensity, P'_{out}, obtained by the proposed BS Capon method with only the

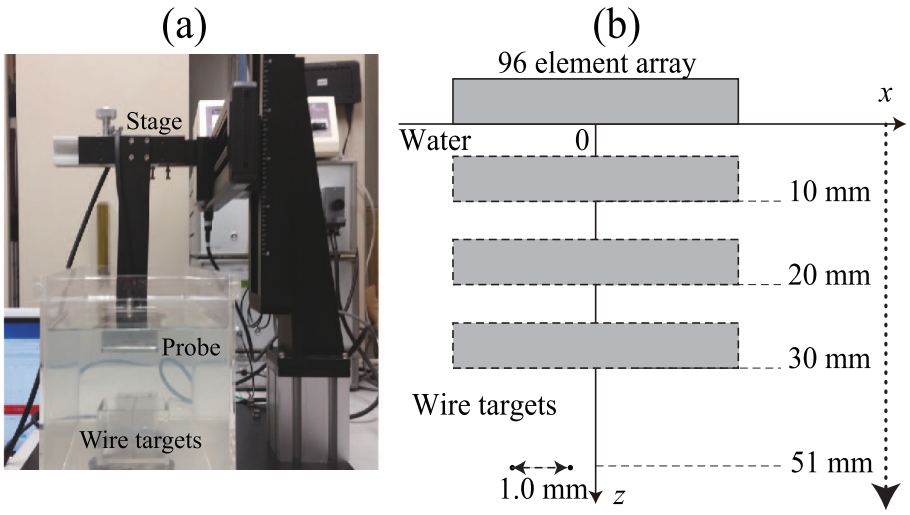

Figure 2.3: (a) Photograph of experimental setup, and (b) schematic illustration of the measurement system with two wire targets in the water tank. (Reproduction from Okumura et al. (2016); Copyright(2016) The Japan Society of Applied Physics.)

complexity reduction technique. The false images appeared at lateral distances of around -0.50 and 0.50 mm. The arrows show the detected peaks in output power P'_{out}. The solid black line in Fig. 2.4 shows the output power obtained using both the complexity reduction technique and compensation technique. The numbers of processes associated with the time-delay and the transformation of the conventional method and the proposed method were 121 and 12, respectively. The estimation errors of the proposed method at the target locations are 1.2 and 2.0 dB at depths of 20 and 50 mm, respectively. These results show that the proposed method successfully yielded high-resolution and high-contrast images with accurate intensity estimation and low computational complexity.

2.3.2 Experimental results

Fig. 2.5 shows the images acquired by the three methods: (a) the DAS method, (b) the conventional BS Capon method with a sub-array size of 64, and (c) the proposed method. The dynamic range in the figure is 60 dB. Figs. 2.6(a), (b), (c), and (d) are cross–sectional views of Fig. 2.5 at 21.4, 31.4, 41.4, and 51.4 mm depths, where the B-mode image acquired by the DAS method has maximum intensity. Table 2.1 shows the evaluation indicators. The first side-lobe levels of the DAS method, conventional BS

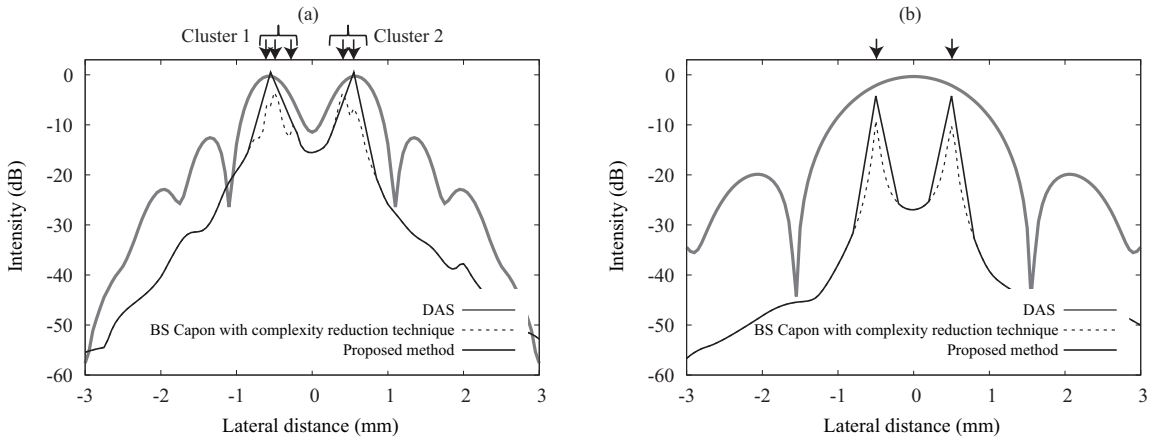

Figure 2.4: Intensity estimated by DAS method, BS Capon method with complexity reduction, and proposed method at the depths of (a) 20 and (b) 50 mm. (Reproduction from Okumura et al. (2016); Copyright(2016) The Japan Society of Applied Physics.)

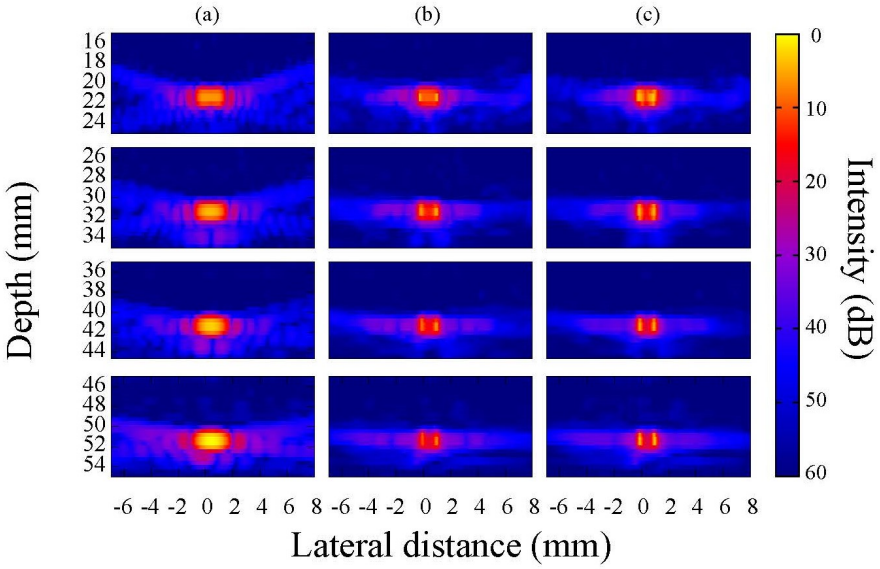

Figure 2.5: Experimental results of B-mode images of wire targets obtained by (a) the DAS method, (b) the conventional BS Capon, and (c) the proposed BS Capon method. The lateral intervals of the targets were 1.0 mm. (Reproduction from Okumura et al. (2016); Copyright(2016) The Japan Society of Applied Physics.)

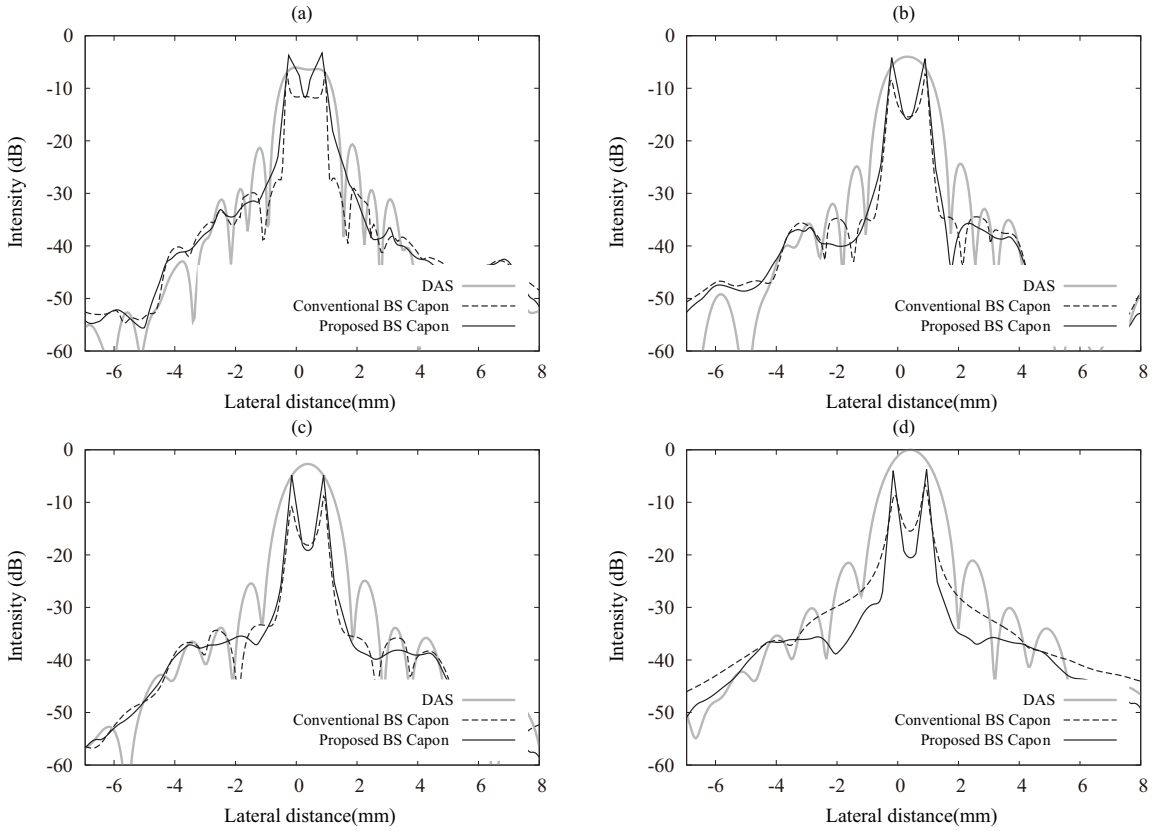

Figure 2.6: Experimental result of cross-sectional images at the target depth obtained by the DAS method, the conventional BS Capon, and the proposed BS Capon method. The lateral interval of the targets was 1.0 mm and the target depths were (a) 21.4, (b) 31.4, (c) 41.4, and (d) 51.4 mm. (Reproduction from Okumura et al. (2016); Copyright(2016) The Japan Society of Applied Physics.)

Capon method, and the proposed BS Capon method with the compensation technique were -5.3, -15, and -17 dB, respectively. The -6 dB beam widths of these methods were 1.7, 0.7, and 0.36 mm, respectively. The estimation errors of these methods in echo intensity were 0, 3.2, and 1.6 dB, respectively. The numbers of operations for the conventional method and the proposed method were 7800 and 532, respectively. The computational complexity of the proposed technique was less than 7% that of the conventional method.

To evaluate the calculation time required to make a 300×26 pixel image, we used a Linux workstation with an Intel(R) Core(TM) i7 CPU (Intel Corp., Santa Clara, CA). The calculation times were 656 ms by the conventional BS Capon method and 81 ms

Table 2.1: Experimental results of (a) the DAS method, (b) the conventional BS Capon method, and (c) the proposed BS Capon method. Each value is the average of four measurements at each depth.

	First side-lobe level (dB)	−6 dB beam width(mm)	Intensity estimation error (dB)	Number of operations	Calculation time (ms)
(a)	−5.3	1.7	–	–	–
(b)	−15	0.7	3.2	7800	656
(c)	−17	0.36	1.6	532	81

by the proposed BS Capon method. The proposed method reduced the calculation time by 88% compared with the conventional BS Capon method. Because in the proposed method the intensity at each depth is calculated individually, we can employ parallel calculations.

2.4 Discussion

The reduction in the number of processes associated with the time-delay and transformation from ES signal processing to BS signal processing is determined by the sub-ROI size. In this experiment, we used Δx of 0.05 mm and sub-ROI size of 2.25 mm, i.e., the sub-ROI size was 45 pixels. The interval of the focal point used in this chapter was 15 pixels. Theoretically, the number of operations in the proposed method might be almost 6.7% of that in the conventional method when we dismiss the recalculation process. Indeed, the number of processes in the proposed method is 6.8% of that in the conventional method even when we take into account of recalculation processes. However, as shown in Sect. 2.3.2, the calculation times for the conventional method and the proposed method were 656 and 81 ms, respectively. The reduction in the calculation time is smaller than the expected reduction. Both conventional and proposed BS Capon methods require an analytic signal at each element. Thus, the RF signals must be transformed into analytic signals. The process is employed by both methods and the calculation time associated with the process is 32 ms. When we dismiss this calculation time, the calculation times for the conventional method and the proposed method are 624 and 50 ms, respectively. The proposed method reduced the calculation time by 92%

of the whole calculation time under this situation.

The error caused by the approximation is small at deeper areas because the distance from the focal point to the measurement point $r_{i,n} - r_{x,n}$ for deep areas is smaller than that at shallow areas. The proposed method of using a large sub-ROI size may yield accurate images of deep areas. Further reduction in complexity may be possible by optimizing the sub-ROI size at each depth.

Theoretically, the imaging performance of the proposed method without power compensation is almost the same as that of the conventional BS Capon method when we use the same sub-array size for both methods. As shown in Table 2.1, the proposed method improves the first side-lobe level and beam width. These improvements were brought about by the power compensation technique.

2.5 Summary and concluding remarks

In this chapter, we proposed techniques that reduce the computational complexity of medical ultrasound imaging by the BS Capon method. A reduction in the number of time-delay processes and a transformation from ES to BS signal processing were required. We replaced the time-delay process by a simpler multiplication of a steering vector and a covariance matrix to reduce the number of processes. Additionally, to achieve accurate echo intensity estimation, we employed a compensation technique of using a small sub-array size.

In an experimental study using a 2.0 MHz center frequency, the proposed method successfully depicted two closely positioned targets with a lateral interval of 1.0 mm. In the proposed method, the number of processes was reduced from 7800 to 532, the first side-lobe level was suppressed from -15 to -17 dB, and the estimation error in echo intensity was decreased from 3.2 to 1.6 dB. The calculation time required for generating a 300×26 pixel image by the proposed method was less than 13% of the time required in the case of the conventional BS Capon method. These results indicate that the proposed method may have the potential to implement adaptive signal processing for real-time medical ultrasound imaging.

Chapter 3

Phase velocity estimation technique based on adaptive array signal processing for ultrasonic guided waves propagating along cortical long bones

3.1 Introduction

As shown in Sect. 1.3.5, several recent studies have used the AT technique, which emits wide-band signals and analyzes the ultrasonic guided waves propagating along the cortical bone. The cortical bone has been described as a transversely isotropic absorbing plate with a finite thickness (Dong and Guo, 2004; Haïat et al., 2009; Naili et al., 2010). The ultrasonic guided waves propagating in cortical bone consist of multiple propagation modes, and their frequency dependent wavenumbers represent the elastic properties of the medium. Thus, many techniques for frequency-phase velocity (f–c) or frequency-wavenumber (f–k) analysis have been reported.

The two-dimensional (2D) Fourier-transform technique provides a means to estimate the f–c relationship of the signals (Alleyne and Cawley, 1991). This technique is equivalent to the non-adaptive beamforming technique, i.e. DAS beamformer for the narrow band signal. Therefore, as well as the non-adaptive DAS beamformer, the resolution strongly depends on the size of the probe; indeed, a larger probe and a larger number of receivers are required for higher resolutions and broader frequency ranges in estimations.

Sasso et al. (2008) proposed a technique based on singular-value decomposition (SVD), a matrix algorithm for nonsquare matrices, for data obtained with a probe consisting of multiple numbers of transmitters and receivers. Minonzio et al. (2010) extended this SVD-based method and succeeded in estimating the phase velocity of Lamb waves propagating in a copper plate. They applied the technique to in-vivo cortical bone and demonstrated a good estimation of phase velocities for different modes (Vallet et al., 2016). However, the measurement frequency range shown in the conventional study is limited (Minonzio et al., 2010). The number of existing modes, the required resolution, and the SNR for the phase velocity estimation of Lamb waves depend on the frequency of the signal. These difficulties limit the measurement frequency range of the conventional method.

In this chapter, we employ estimation of signal parameters via rotational invariance techniques (ESPRIT) (Haardt and Nossek, 1995; Roy and Kailath, 1989). The ESPRIT algorithm is a classical high-resolution beamforming technique. As shown in Sect. 1.5.4, the basics of the beamforming technique for DOA estimation and phase velocity estimation is the same, so we can directly apply the ESPRIT algorithm to the AT technique. In the ESPRIT algorithm, phase velocity is directly and numerically estimated without peak search process. In the inversion process that estimates the elastic properties of a specimen (Bochud et al., 2017; Foiret et al., 2014), the values of the wavenumbers or phase velocities are required. To estimate the values from the intensity profile, the determination of parameters such as thresholds for intensity and prominence is required. Thus, the ESPRIT algorithm should be effective for the wavenumber or phase velocity estimation.

Both SVD and ESPRIT algorithms require the number of existing modes at the measurement frequency. However, this is difficult to determine because it depends on the frequency. Additionally, ESPRIT algorithm assumes that the arrival waves do not correlate with each other (Haardt and Nossek, 1995; Roy and Kailath, 1989; Takao and Kikuma, 1987). However, the propagation modes of Lamb waves correlate with each other.

To suppress this correlation, the spatial averaging technique is widely known and conventionally used with the ESPRIT algorithm. Spatial averaging, which is introduced in Sect. 1.5.3, situates sub-arrays in the whole receiver array and averages the received signals. The receiver size after spatial averaging determines not only the correlation suppression performance but also the resolution of the adaptive beamforming technique and the SNR. That is, there is a trade-off between resolution and SNR, making it difficult to determine the optimal size. When a large sub-array is used, the resolution of the estimation increases, but the SNR decreases.

In this chapter, we propose a new algorithm that does not require a specific sub-array size or the estimation of the number of existing modes. We first estimate phase velocity using multiple sub-arrays of different sizes for spatial averaging and multiple different numbers of existing modes for the ESPRIT algorithm with one transmitter and multiple receivers. We evaluate the correspondence of the estimated phase velocities with the different sub-arrays and modes. If an inappropriate number is used, false phase velocities are estimated. Additionally, we propose a false-phase-velocity rejection technique using a particular feature of Lamb waves.

We evaluated this method using a copper plate of known thickness and shear and longitudinal wave velocities. We conducted the experiments and numerical simulation (Nguyen and Naili, 2012, 2013) and herein present our results.

3.2 System model

Fig. 3.1 shows the system model employed in this chapter. The wave associated with each mode propagates along the x direction with a certain phase velocity that is determined by its shear and longitudinal wave velocities and plate thickness. For a copper plate, the longitudinal and shear wave velocities are 4650 and 2260 m/s, respectively.

The signal model is shown in Eq. (1.96). With the vector and matrix form, the vector corresponding to the received signal $\mathbf{S}(f)$ in the frequency domain is given by

$$\begin{aligned}
\mathbf{S}(f) &= [S_1(f)\cdots S_N(f)]^{\mathrm{T}}, && (3.1)\\
&= \mathbf{A}_{\mathrm{c}}(f)\mathbf{S}^{\mathrm{t}}(f), && (3.2)\\
&= [\mathbf{a}_{\mathrm{c}}(f,c_1)\cdots\mathbf{a}_{\mathrm{c}}(f,c_M)][S_1^{\mathrm{t}}(f)\cdots S_M^{\mathrm{t}}(f)]^{\mathrm{T}}, && (3.3)\\
\mathbf{a}_{\mathrm{c}}(f,c_m) &= [\exp\{j\Psi_1(f,c_m)\}\cdots\exp\{j\Psi_N(f,c_m)\}]^{\mathrm{T}}, && (3.4)\\
\Psi_n(f,c_m) &= -2\pi f n\Delta l/c_m(f), && (3.5)
\end{aligned}$$

where f is the measurement frequency, $S_n(f)$ is the received signal at the n-th element, $c_m(f)$ is the phase velocity of the m-th propagation signal, Δl is the pitch of the receiver, $\mathbf{a}_{\mathrm{c}}$ is the steering vector for $f-k$ analysis, M is the number of modes, and $S_m^{\mathrm{t}}(f)$ is the amplitude of the m-th propagation signal. The sizes of the matrix $\mathbf{A}_{\mathrm{c}}(f)$ and vector $\mathbf{S}(f)$ are $N\times M$ and $N\times 1$, respectively.

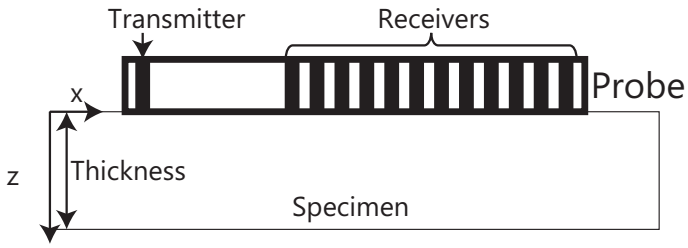

Figure 3.1: System model of axial transmission technique. (Reproduction from Okumura et al. (2017); Copyright(2017) The Japan Society of Applied Physics.)

3.3 Materials and methods

3.3.1 Estimation of phase velocity using the ESPRIT algorithm

Here, we briefly explain the phase velocity estimation using the ESPRIT algorithm that forms the basis of the proposed method. By the ESPRIT method, we estimate the phase velocity by comparing the received signals at two arrays shown in Fig. 3.2. When there is a propagation signal, i.e., $M = 1$ in the previous section, with the phase velocity of $c_1(f)$, the relationship between the received signal vectors of array 1 and 2 is shown as

$$\mathbf{S}_2(f) = \mathbf{S}_1 \exp(-\mathrm{j}2\pi f \Delta l / c_1(f)), \tag{3.6}$$

$$\mathbf{S}_1(f) = [S_1(f) \cdots S_{N-1}(f)]^{\mathrm{T}}, \tag{3.7}$$

$$\mathbf{S}_2(f) = [S_2(f) \cdots S_N(f)]^{\mathrm{T}}, \tag{3.8}$$

where $\mathbf{S}_1(f)$ and $\mathbf{S}_2(f)$ are the received signal vectors of arrays 1 and 2, respectively.

As shown in Eq. (3.6) and Fig. 3.2, a single phase velocity of a single signal is estimated by comparing two arrays. The ESPRIT algorithm expands this principle to multiple signals using the eigenvalue decomposition, as shown in Fig. 3.2. The ESPRIT algorithm applies eigenvalue decomposition to the covariance matrix of the received signal to separate signals and noises. After the separation of signals, the ESPRIT algorithm estimates the phase velocity by comparing two arrays. The detail of this algorithm is shown in Haardt and Nossek (1995); Roy and Kailath (1989).

Spatial averaging is performed in 2D ultrasound imaging using an adaptive beamforming technique (Okumura et al., 2016; Taki et al., 2012). This technique situates the sub-arrays in the whole array and averages the covariance matrices of these sub-arrays (Fig. 3.3) (Takao and Kikuma, 1987). The covariance matrix obtained using the spatial

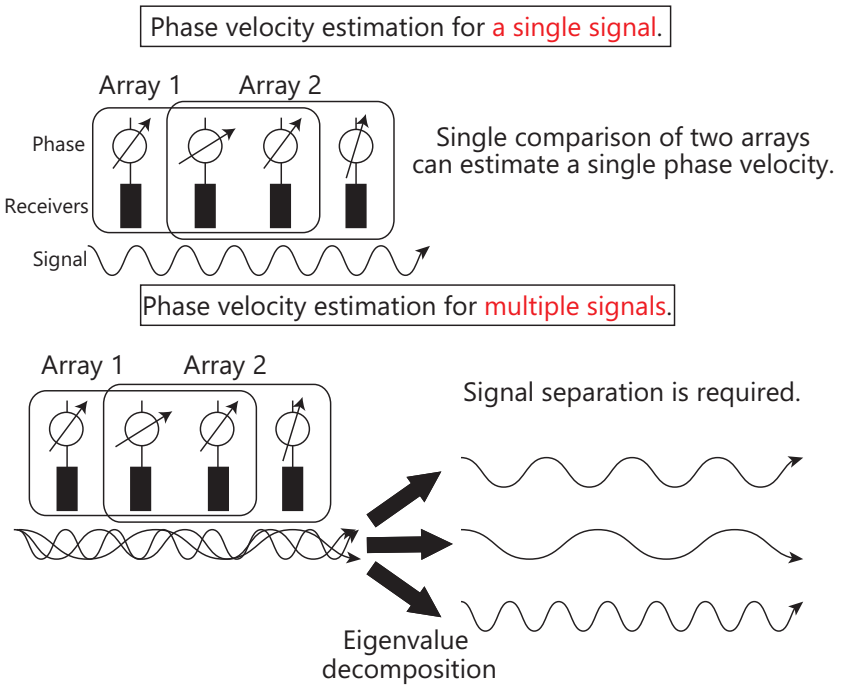

Figure 3.2: Schematic of the ESPRIT algorithm.(Reproduction from Okumura et al. (2017); Copyright(2017) The Japan Society of Applied Physics.)

averaging technique for AT technique is given by

$$\mathbf{R}_{\mathrm{A}}(f) = \frac{1}{N_{\mathrm{ave}}} \sum_{n=1}^{N_{\mathrm{ave}}} \mathbf{R}_n(f), \tag{3.9}$$

$$\mathbf{R}_n(f) = \mathbf{S}_n(f)\mathbf{S}_n(f)^{\mathrm{H}}, \tag{3.10}$$

$$\mathbf{S}_n(f) = [S_n(f) \cdots S_{n+N_{\mathrm{sub}}-1}(f)]^{\mathrm{T}}, \tag{3.11}$$

where N_{ave} is the number of averaging steps. The sub-array size N_{sub} is given by $N_{\mathrm{sub}} = N - N_{\mathrm{ave}} + 1$. The technique controls the resolution of the ESPRIT algorithm and SNR. Note that a small N_{sub} achieves a low resolution because the number of usable elements is small. In contrast, because the number of averaging steps is large, the SNR increases. The maximum number of modes that the ESPRIT algorithm can estimate is $N_{\mathrm{sub}} - 1$ and note that the algorithm requires the number of existing modes, M.

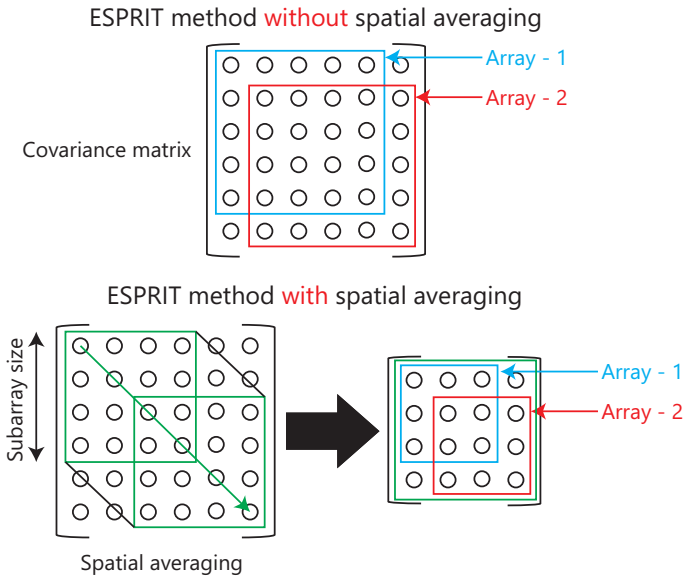

Figure 3.3: Schematic illustration of spatial averaging. (Reproduction from Okumura et al. (2017); Copyright(2017) The Japan Society of Applied Physics.)

3.3.2 High-accuracy phase velocity estimation

In this section, we describe the proposed method. To estimate phase velocity, the estimation of the number of modes present at the measurement frequency, M, is required. Conventional studies determine the number through its dependence on eigenvalue, which related to the intensity. However, when we determine the number in this manner, we cannot extract modes with small eigenvalues. Thus, we propose an alternative technique to obtain a better estimate M.

The ranges of longitudinal and shear wave velocities and thicknesses of cortical bone, which determine the phase velocities of bone, are limited. Thus, we can roughly estimate the maximum number of existing modes. The maximum number of estimation modes is determined by the number of receivers. In this chapter, we propose the technique with the sufficient number of receivers that is more than or equal to the maximum number of existing modes over the measurement frequency range.

When we overestimate M, false estimates of phase velocity occur because the ESPRIT algorithm estimates the phase velocity of noise. To correctly estimate the number of modes, a technique to exclude false estimates of phase velocity is required. In the application to Lamb waves, we remove noise by exploiting certain features of the phase velocity associated with false estimates.

Because different sizes of sub-arrays vary the number of averaging steps and the SNR, when we employ a sub-array of different size, N_{sub}, the estimated phase velocity of noise is also changed. Therefore, with a different sub-array size, the falsely estimated phase velocity appears randomly. In contrast, the estimated phase velocity that represents a real mode remains almost unchanged even when we change N_{sub}. The phase of the noise that determines the phase velocity should have a random value from 0 to 2π. The estimated phase velocity of noise is given by

$$c_{\mathrm{N}}(f) = -2\pi f \Delta l / \phi_{\mathrm{N}}, \tag{3.12}$$

where ϕ_{N} is the randomly distributed phase of the noise and c_{N} is the phase velocity of the noise. Thus, with a random value of ϕ_{N}, the phase velocity of the noise appears to spread randomly at higher phase velocities and more densely at lower phase velocities. We remove false velocities using the following two conditions.

(i) We first estimate phase velocity with sub-arrays of different sizes from N_1 to N_2. We set the number of modes present as $N_{\mathrm{sub}} - 1$, that is, the maximum number of modes when we use the sub-array size of N_{sub}. We identify the isolated estimates of phase velocity as false estimates. To identify the reliable estimates, we set the following conditions:

$$|c_{\mathrm{e},m'}(f,n') - c_{\mathrm{e},m}(f,n)| < c_{\mathrm{th}}, \tag{3.13}$$

where $c_{\mathrm{e},m}(f,n)$ is the m-th estimated phase velocity with a sub-array size of n, $n' \neq n, m' \neq m, N_1 \leq (n,n') \leq N_2$, $1 \leq (m,m') \leq n-1$, and c_{th} is the critical threshold. We consider reliable phase velocities, $c_{\mathrm{e},m}(f,n)$, as those that can provide more than one different estimated phase velocity, $c_{\mathrm{e},m'}(f,n')$, that satisfies Eq. (3.13).

(ii) At this point, we have removed some of the false estimates at higher phase velocities. We next propose the condition to remove lower false phase velocities by using a feature of the phase velocity of Lamb waves. The A0-mode has the lowest phase velocity and is dominant at lower frequencies. Therefore, when we select the mode with the highest estimate of power at lower frequencies, the phase velocity of the A0-mode is estimated. We therefore estimate its phase velocity and remove all phase velocities below the A0-mode phase velocity.

We estimate the A0-mode phase velocity, $c_{\mathrm{A0}}(f)$, using the expression

$$c_{\mathrm{A0}}(f) = \frac{1}{N_2 - N_1 + 1} \sum_{n=N_1}^{N_2} c_{\mathrm{e},1}(f,n), \tag{3.14}$$

where $c_{\mathrm{e},1}(f,n)$ is the estimated phase velocity having the highest estimated intensity with a sub-array size of n. We remove the estimated phase velocities lower than $c_{\mathrm{A0}}(f) -$

c_{th2}. c_{th2} is the threshold for false phase velocity rejection using the A0-mode phase velocity.

3.3.3 Simulation and experimental settings

To verify the described algorithm above, we performed a simulation and an experiment with the same settings. We use a 2.0-mm-thick copper plate. The center frequency of the transmitted signal is 1.0 MHz. We used a transmitter and sixteen receivers. The pitch of the receivers is 0.75 mm and the distance from transmitter to the first receiver is 15 mm. We use a range of sub-array sizes, N_1 and N_2, of 5 to 9. We used values of 20 m/s for c_{th} and 100 m/s for c_{th2}. In the numerical simulation, we use the semi-analytical finite element method (Nguyen and Naili, 2012, 2013).

3.4 Results

Figs. 3.4 and 3.5 show the numerical simulation and experimental results for a 2-mm-thick copper plate. To show the advantage of the proposed method, we compare the measurement frequency range of the proposed method with that of the conventional SVD method. The dashed lines express the measurement limitation given by Minonzio et al. (2010). We calculated the limitation using the relation $1/7 = c_{\text{d}}(f)/(fN\Delta l)$, where $c_{\text{d}}(f)$ is the limit of phase velocity at f. For comparison with the conventional study, we plotted not only the line with $N = 16$ but also that with $N = 14$ because that study employed fourteen receivers.

The proposed method successfully reduced the phase velocities obtained in both the simulation and experiment. Compared with the limitations of the conventional method, our proposed method achieves an accurate and broad estimation.

To quantitatively evaluate the proposed method, we use the index of 'fitting error' for the following conventional study.

$$100\frac{1}{N^{\text{exp}}}\sum_{f_{\text{min}}}^{f_{\text{max}}}\sum_{n=N_1}^{N_2}\sum_{m=1}^{n-1}|c'_{\text{e},m}(f,n)-c^{\text{t}}|/c^{\text{t}}, \tag{3.15}$$

where N^{exp} is the number of estimated phase velocities, $c'_{\text{e},m}(f,n)$ is the estimated phase velocity after applying all false velocity rejection techniques, c^{t} is the theoretical phase velocity estimated using the true thickness and longitudinal and shear wave velocities, and f_{min} and f_{max} are respectively the minimum and maximum measurement frequencies.

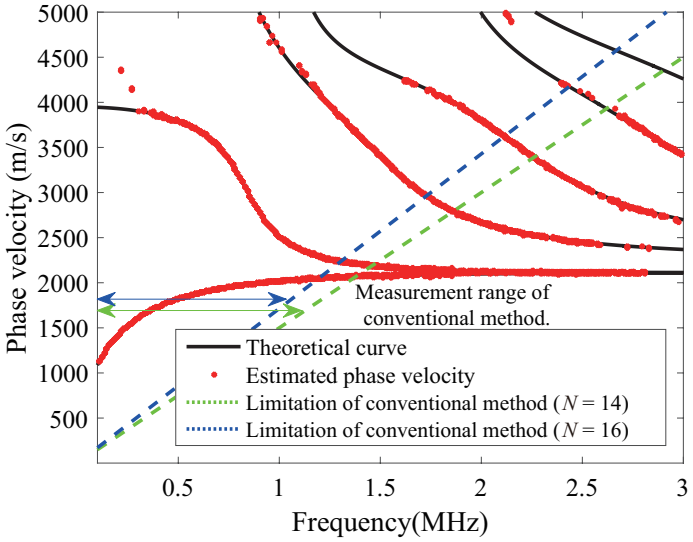

Figure 3.4: Results of the numerical simulation. Red dots indicate the estimated phase velocity using the proposed method. Black solid lines mark the theoretical phase velocity of Lamb waves. Blue and green dashed lines indicate the measurement limits of the conventional SVD method. c_{th} and c_{th2} are 20 and 100 m/s, respectively. (Reproduction from Okumura et al. (2017); Copyright(2017) The Japan Society of Applied Physics.)

The fitting errors of the numerical simulation and experimental results are 0.26 and 1.3%, respectively. The maximum measurement frequency of the A0-mode is 2.8 MHz in both cases, whereas that of the conventional method with fourteen receivers is only 1.4 MHz. Thus, the measurement frequency range of the proposed method is twice wider than that of the conventional method.

3.5 Discussion

Fig. 3.6 shows the estimated phase velocities with multiple different sub-array sizes of the experimental study after phase velocity rejection technique based on A0-mode phase velocity. We can see that the estimated phase velocities concentrate at the true phase velocities. Thus, the evaluation of the consistency is reasonable.

The basic ideas are similar between the conventional SVD-based technique and the ESPRIT algorithm. Both separate the signal and noise using singular-value and eigen-

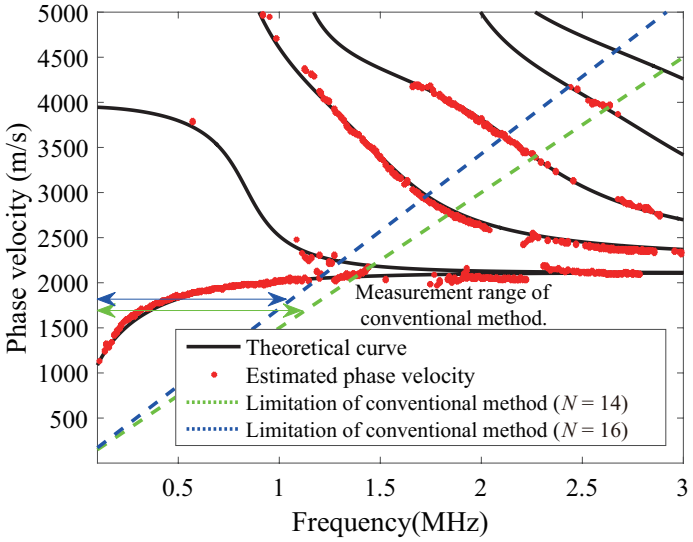

Figure 3.5: Same as in Fig. 3.4, but for results of the experiment. (Reproduction from Okumura et al. (2017); Copyright(2017) The Japan Society of Applied Physics.)

value decompositions, respectively. However, in the conventional techniques, the phase velocity is estimated using the 2D (frequency-phase velocity) intensity map. Therefore, in addition to estimating this map, extracting the exact phase velocity is required. In contrast, in the case of using the ESPRIT algorithm, the phase velocity is directly estimated. To estimate the parameters of the plate, an inversion process is required, for which the exact phase velocity is required. Hence, the ESPRIT makes it easier to estimate parameters.

We used 16 receivers and one transmitter, which differs from the conventional study (Minonzio et al., 2010), in which 14 receivers and 3 transmitters are used. Because the conventional technique with multiple transmitters is equivalent to the spatial averaging, the conventional technique with three transmitters is equivalent to an eigenvalue decomposition applying spatial averaging three times. Moreover, the difference in whole-receiver size is 1.5 mm, the effects of which can thus be ignored.

The reported fitting error in the conventional study was around 5% (Minonzio et al., 2010). Because the system and algorithm are different, these previous results cannot be directly compared with the results. However, errors of the proposed method (0.26 and 1.3%) are sufficiently small for bone quality assessment.

Here, we show the performance of the proposed method with different thresholds, c_{th}

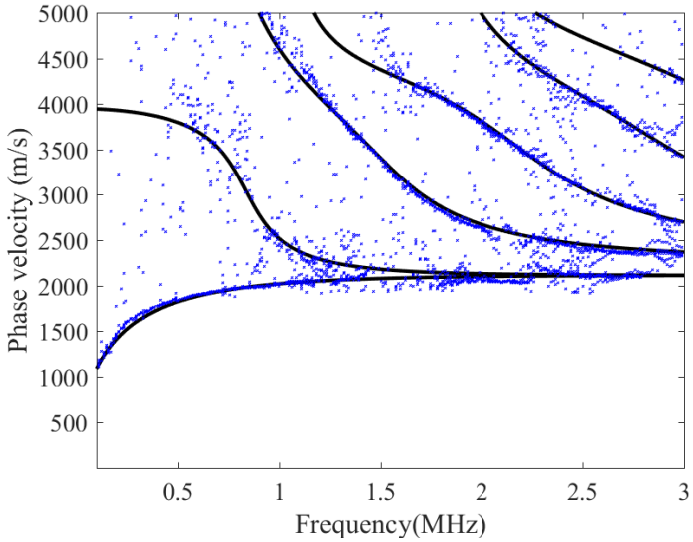

Figure 3.6: Estimated phase velocities of the experimental study with multiple different sub-array sizes after the false phase velocity rejection technique based on A0-mode phase velocity.

and c_{th2}. Fig. 3.7 shows the experimental results with (c_{th}, c_{th2})=(10 m/s, 100 m/s) and (100 m/s, 100 m/s). c_{th} determines the range of false phase velocity rejection. Thus, there is a trade-off between the number of estimated phase velocities and the reliability of estimated phase velocities. As shown in Fig. 3.7, there is a higher-order mode at 2.5 MHz with c_{th} of 100 m/s. However, the estimation error increases. When we change c_{th} from 10 to 100 m/s with c_{th2} of 100 m/s, the fitting errors range from 1.3 to 1.6% and the measurement frequency range is constant. The dependence of fitting error on the threshold is small. The value should depend on the requirement of the system for estimating bone quality using the estimated phase velocities.

Fig. 3.8 shows the experimental results with (c_{th}, c_{th2})=(20 m/s, 10 m/s) and (20 m/s, 200 m/s). c_{th2} is the threshold that removes low false phase velocities. Thus, when we use small values for c_{th2}, the proposed method may remove the A0-mode phase velocity. As shown in Fig. 3.8, the dependence of fitting error on c_{th2} is small. When we change c_{th2} from 10 to 200 m/s with c_{th} of 20 m/s, the fitting errors range from 1.28 to 1.35% and the measurement frequency range is constant. A smaller value, e.g., smaller than 200 m/s, is appropriate.

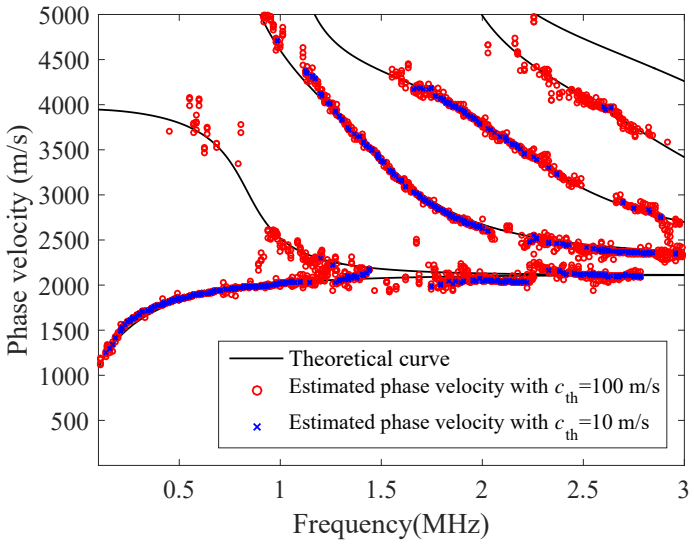

Figure 3.7: Estimated phase velocities with different threshold c_{th} values of 10 and 100 m/s with c_{th2} of 100 m/s. (Reproduction from Okumura et al. (2017); Copyright(2017) The Japan Society of Applied Physics.)

3.6 Summary and concluding remarks

The analysis of guided waves propagating in cortical bone using the AT technique is promising for medical applications. Wider frequency ranges and more accurate velocity estimations might bring better diagnoses. We proposed and assessed an estimation technique based on the ESPRIT algorithm with spatial averaging. Spatial averaging controls the resolution and SNR. We estimate the phase velocity multiple times using different sub-array sizes and evaluate the correspondence of the results. In addition, we proposed a method to remove false phase velocities. The simulation and experimental results demonstrate that the fitting errors are 0.26 and 1.3%, respectively. The frequency measurement ranges are twice as wide as those in the conventional method. We believe that the proposed AT technique is effective in the analysis of cortical bone quality.

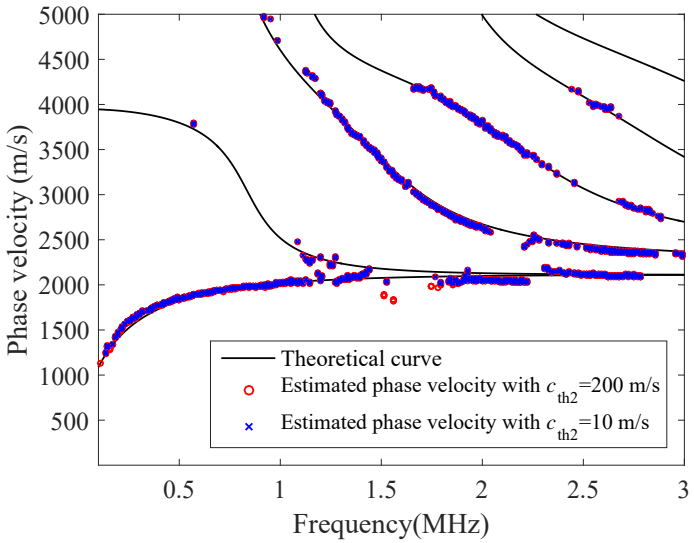

Figure 3.8: Estimated phase velocities with threshold c_{th} of 20 m/s with different c_{th2} values of 10 and 200 m/s. (Reproduction from Okumura et al. (2017); Copyright(2017) The Japan Society of Applied Physics.)

Chapter 4

High-resolution and fast wavenumber estimation of ultrasonic guided waves with adaptive array signal processing

4.1 Introduction

In the previous chapter, we proposed a technique to estimate the phase velocities of the guided waves with the ESPRIT algorithm. In this chapter, we propose a technique with lower computational complexity.

To avoid strictly estimating the number of signals M, we used the multiple sub-arrays with different sizes and iteratively calculated the eigenvalues which cost the large computational complexity in the previous study. Additionally, the resolution of the previously proposed technique is limited because it is determined by the smallest sub-array size.

To resolve these problems, in this chapter, we propose a new algorithm to estimate the number of signals M using the information theoretic criteria without including process that requires the large computational complexity. This estimation is effective for using both SVD and ESPRIT methods. While many studies estimating M that employ information theoretic criteria have been reported (Huang et al., 2012; Lombardini and Gini, 2005; Sauer et al., 2007; Wax, 1991; Wax and Kailath, 1985), these methods were not applied for the analysis of ultrasonic guided waves propagating along a transversely isotropic absorbing material like cortical bone.

Several high-resolution wavenumber estimation techniques have been reported. Tran et al. (2014b) proposed the Radon transform method, which estimates the phase velocity at each frequency. The Radon transform method employs a single transmitter and mul-

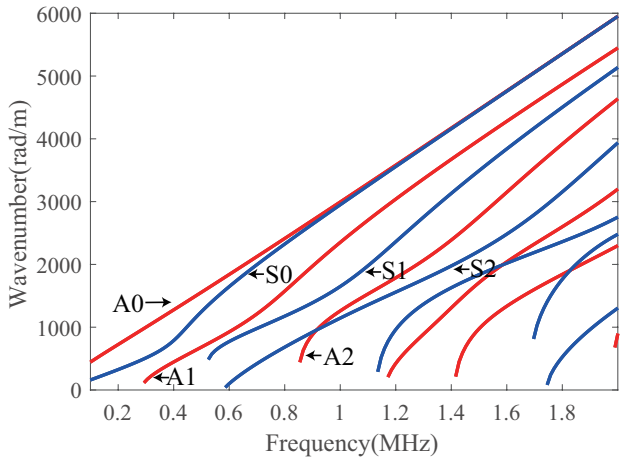

Figure 4.1: Theoretical wavenumbers of 4mm-thick copper plate.

tiple receivers and estimate the phase velocity using an iterative process, and produces high-resolution estimates. However, the computational complexity is not low because it requires the inversion of a large matrix. Xu et al. (2016a) proposed the sparse SVD (S-SVD) method, which combines the Radon transform method proposed by Tran et al. (2014b) and the SVD method. The method acquires super-resolution estimates by employing SVD and an iterative process. However, this method also requires the estimation of the number of propagation modes in the received signal and multiple calculations of a large matrix inversion.

We compared the computational complexity between the proposed method and a conventional method and determined the effectiveness of the proposed method via a simple numerical simulation and experiments with a copper plate and a bone-mimicking plate.

4.2 Materials and methods

In this chapter, we estimate wavenumbers, not phase velocities to follow the recent studies (Bochud et al., 2017; Xu et al., 2016a,b). The theoretical wavenumbers are shown in Fig. 4.1. Because the wavenumber k is given by $k = 2\pi f/c$, the analysis of wavenumber and phase velocity is theoretically same. However, in the wavenumber axis, the resolution does not depend on the frequency.

4.2.1 Estimation of the number of signals

Overview of the basic theory

The schematic system and signal model are the same as the Chap. 3. We first estimate the covariance matrix with the sub-array size of N_{sub} with the whole array size of N as shown in Eq. (3.9). We next apply the eigenvalue decomposition as one of the steps of the ESPRIT algorithm.

The eigenvalues of the covariance matrix with spatial averaging, $\mathbf{R}_{\mathrm{A}}(f)$ which is shown in Eq. (3.9), are expressed as:

$$\lambda_1^{\mathrm{e}}(f) \geq \cdots \geq \lambda_{M(f)}^{\mathrm{e}}(f) > \lambda_{M(f)+1}^{\mathrm{e}}(f) = \cdots = \lambda_{N_{\mathrm{sub}}}^{\mathrm{e}}(f) = \sigma_{\mathrm{n}}^2, \tag{4.1}$$

where σ_{n}^2 is the noise intensity. We note that the absolute value of the eigenvalues do not directly match the intensity of the signal, i.e. when we have two waves with the same intensity, the eigenvalues that correspond to the signals do not have the same value. Thus, the simple thresholding process is not suitable for the accurate estimation of the number of signals.

In this section, we propose a technique to estimate $M(f)$. To estimate $M(f)$, methods that use the information theoretic criteria, which is called minimum description length (MDL), have been reported (Wax, 1991; Wax and Kailath, 1985). The evaluation index $G(m)$ to estimate M is given by:

$$G(m) = -\log \left(\frac{\prod_{i=m+1}^{N_{\mathrm{sub}}} \lambda_i^{\mathrm{e}}(f)^{\frac{1}{N_{\mathrm{sub}}-m}}}{\sum_{i=m+1}^{N_{\mathrm{sub}}} \frac{\lambda_i^{\mathrm{e}}(f)}{N_{\mathrm{sub}}-m}} \right)^{(N_{\mathrm{sub}}-m)N_{\mathrm{ave}}} + \frac{1}{2} m(2N_{\mathrm{sub}} - m) \log N_{\mathrm{ave}}, \tag{4.2}$$

where $G(m)$ is the index, m that minimizes $G(m)$ represents the estimated $M(f)$. Here, let us define the estimated $M(f)$ as $M'(f)$.

Diagonal loading technique for AT technique

In Eq. (4.2), the numerator and denominator represent the geometric and arithmetic means of the eigenvalues, respectively. Thus, smaller eigenvalues make the estimates unstable. To stabilize the estimation, we employ a technique, which adds a diagonal matrix to the covariance matrix (Huang et al., 2012; Lombardini and Gini, 2005; Sauer et al., 2007). This is equivalent to adding an offset value to the eigenvalues.

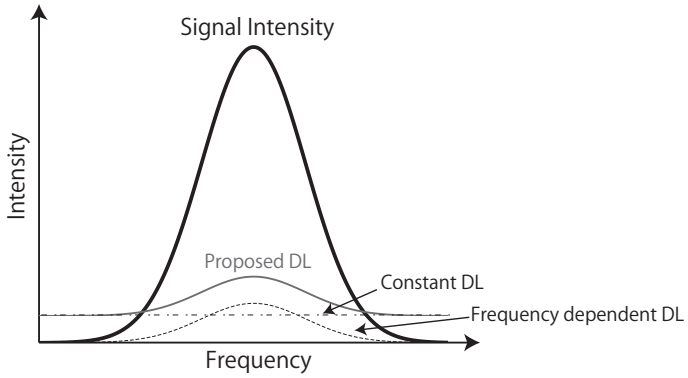

Figure 4.2: Proposed diagonal loading(DL) technique.

We propose a new scheme for the wavenumber estimation. The process is given by the following:

$$\mathbf{R}'(f) = \mathbf{R}(f) + \eta_{\mathrm{d}}(f)\mathbf{I}, \tag{4.3}$$

where η_{d} is a DL factor for AT technique and $\mathbf{I}$ is the identity matrix. The process shown in the previous equation can be rewritten as follows:

$$\lambda_i^{\mathrm{e}\prime}(f) = \lambda_i^{\mathrm{e}}(f) + \eta_{\mathrm{d}}(f), \tag{4.4}$$

where $\lambda_i^{\mathrm{e}\prime}(f)$ is an eigenvalue that is calculated from $\mathbf{R}'(f)$. Therefore, even when we use a different DL factor with the same covariance matrix, we do not need to employ the eigenvalue decomposition process again. In other words, we employ the DL technique for the estimation of M as the offset value. By replacing λ_i^{e} in Eq. (4.2) with $\lambda_i^{\mathrm{e}\prime}$, we can get the modified estimates of M.

Determination of the DL factor

The selection of the DL factor is important for the estimation of M. In this chapter, we employed two DL factors that depend on the received signal intensity. The schematic illustration of the two factors is shown in Fig. 4.2.

The DL factor is given by

$$\eta_{\mathrm{d}}(f) = \eta_1(f)\delta_1(f) + \eta_2\delta_2, \tag{4.5}$$

$$\delta_1(f) = \mathrm{tr}\{\mathbf{R}(f)\}, \tag{4.6}$$

$$\delta_2 = \frac{1}{f_2 - f_1} \int_{f_1}^{f_2} \mathrm{tr}\{\mathbf{R}(f)\} \mathrm{d}f, \tag{4.7}$$

where η_1 and η_2 are the DL factors and f_1 and f_2 are the frequency range used for η_2. $\mathrm{tr}\{*\}$ represents the trace of the matrix. $\eta_2\delta_2$ is employed for the stabilization, which is called constant DL in Fig. 4.2, because with small signal intensity, $\eta_1(f)\delta_1(f)$, which is called frequency dependent DL in Fig. 4.2, approaches zero. Because $\eta_2\delta_2$ is employed just for the stabilization, we choose the frequency range that contains the noise only and set the small value of η_2.

To determine $\eta_1(f)$ for the wavenumber estimation, we assumed that in a certain frequency range, the optimal $\eta_1(f)$ is common. This assumption was made for the reason that as mentioned below, M' has a step-like change with respect to η_1. The optimal η_1 that gives the optimum M has a range and is not a critical value.

We change $\eta_1(f)$ within the range and select the minimum η_1 that gives $M'(f)$ that satisfies the following condition:

$$\max\{M'(f)\} < M_{\mathrm{th}}, \text{ with } (f - f_{\mathrm{w}} \leq f \leq f + f_{\mathrm{w}}), \tag{4.8}$$

where f_w is the width of the frequency window, which is employed for stable estimation and M_{th} is a threshold value of M that is sufficiently large for the wavenumber estimation.

4.2.2 Experimental setup

We employed an array probe that consists of a single transmitter and 28 receivers ($N = 28$) with an element pitch of 0.75 mm. The distance between a transmitter and the first receiver was 18.75 mm. Note that, the aperture size is larger than the previous chapter to follow the recent study (Xu et al., 2016a). The center frequency of the transmitted wave was 1.0 MHz. We used two specimens: 1) a 4 mm thick copper plate (shear wave velocity of 2260 m/s and longitudinal wave velocity of 4650 m/s), and 2) a 4 mm thick transversely isotropic bone-mimicking plate (Sawbones, Vashon, WA). The elastic parameters of the bone-mimicking plate were determined in previous studies (Foiret et al., 2014; Xu et al., 2016a).

In the proposed method, we set $M_{\mathrm{th}} = N_{\mathrm{sub}} - 1$, $f_{\mathrm{w}} = 0.5$ MHz, $\eta_2 = -40$ dB at the frequency range of $f_1 = 4.9$ MHz and $f_2 = 6.1$ MHz, and $N_{\mathrm{sub}} = 15$. We prepare the DL factor with the range of η_1 was -100 dB to 0 dB and interval of 10 dB.

We used $N_{\mathrm{ave}} = 5$ and $N_{\mathrm{sub}} = 24$ in the conventional SVD method (Xu et al., 2016a). In the previous study, they used multiple transmitters. The employment of multiple transmitters and sub-arrays is theoretically the same.

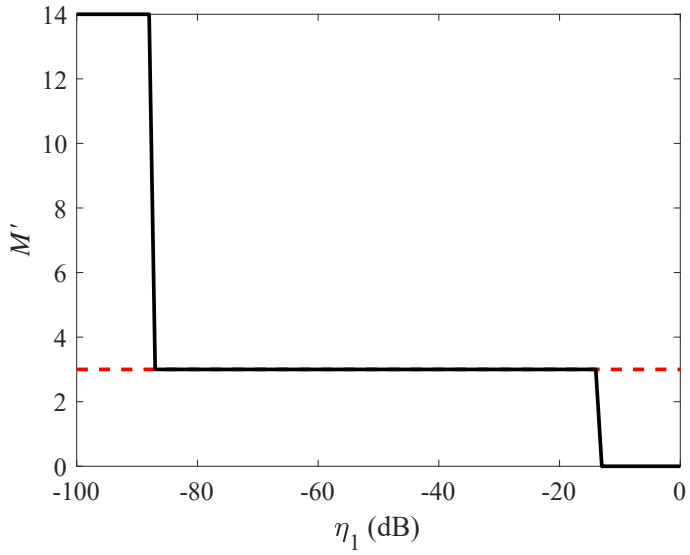

Figure 4.3: Estimated number of propagation modes (black line). True number of propagation modes (red dotted line).

4.3 Results

4.3.1 Evaluation of the number of the propagation modes with diagonal loading

To evaluate the M estimation using DL, we conducted a simple simulation. We assumed that three waves with $k = 1000, 2000$, and 3000 rad/m are propagating. The SNR was 40 dB, $N = 28$, and $N_{\mathrm{sub}} = 15$. In this subsection, we prepare the DL factor with interval of 1 dB.

The estimation result is shown in Fig. 4.3. The estimated M, M' = 14, 3, and 0 with the -100 dB $\leq \eta_1 \leq -88$ dB, -87 dB $\leq \eta_1 \leq -14$ dB, and -13 dB $\leq \eta_1 \leq 0$ dB, respectively. We can see that estimated M has a step-like change with respect to the change of η_1. The root mean square error (RMSE) at $\eta_1 = -40$ dB was 0.73 rad/m.

4.3.2 Experimental results

Figs. 4.4 and 4.5 show the experimental results with the copper plate and bone-mimicking plate, respectively. The color maps show results using the conventional SVD method. The red dots are estimated results with the proposed method. To remove the obvious false estimates, we removed the estimates with the $c < 1200$ and $c > 50000$ m/s. The pro-

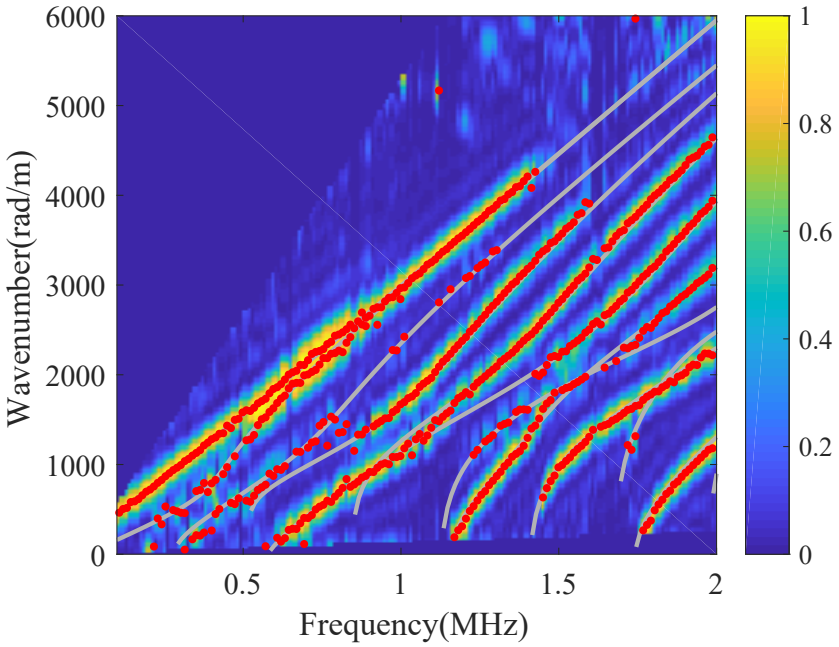

Figure 4.4: Estimated wavenumbers of the 4 mm copper plate using the proposed method and conventional SVD method. Red dots show estimates of the proposed method. The color intensity map shows the results of the conventional SVD method. Solid gray lines show the theoretical curve.

posed method succeeded in depicting the wavenumber without peak search processes. The RMSE of the estimation result of the proposed method with the copper plate and bone-mimicking plate was 108 rad/m and 121 rad/m, respectively. The wavenumber of the shear wave that had a larger effect on the theoretical curve than the longitudinal wave at the center frequency (1.0 MHz) of the copper plate and bone-mimicking plate was 2780 rad/m and 3879 rad/m, respectively. Compared with the wavenumber of the shear wave, the RMSE was less than 4%.

The spectrum at the frequency that is denoted by a white dotted line in Fig. 4.5 is shown in Fig. 4.6. As shown in Fig. 4.6, the proposed method has a higher resolution than the conventional method. The estimated wavenumbers with the proposed method were almost the same as the peak position in the SVD spectrum when the resolution of SVD was high enough or the resolution of the ESPRIT algorithm was not enough to separate the signals. However, it is difficult to identify some of the peaks because of their small amplitude and poor prominence when we use the SVD method such as the peaks with the wavenumber of around 2800 and 4300 rad/m.

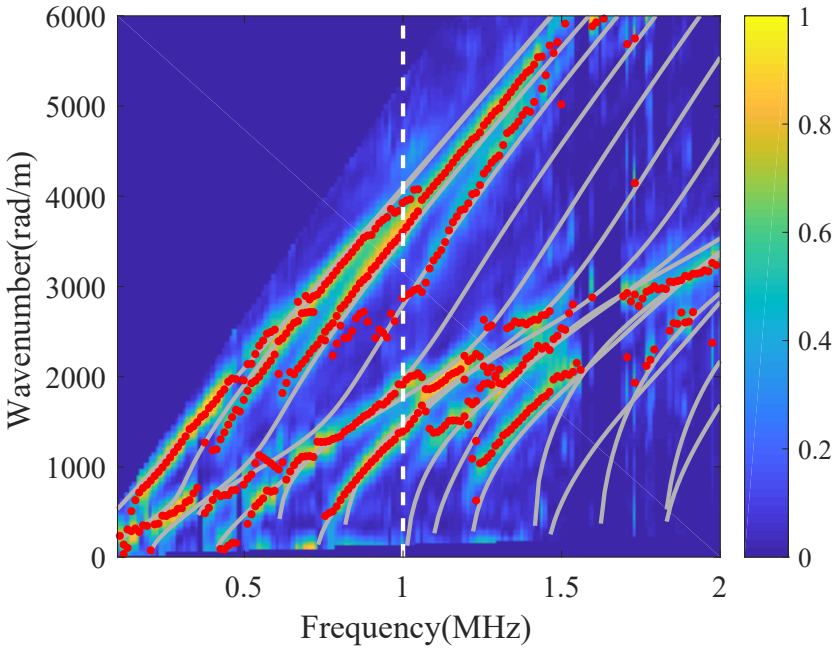

Figure 4.5: Estimated wavenumbers of the 4 mm thick bone-mimicking plate using the proposed method and conventional SVD method. Red dots show the estimates of the proposed method. The color intensity map shows the result of the conventional SVD method. Solid gray lines show the theoretical curve.

The computational complexity related to a wavenumber or phase velocity estimation steps that requires the relatively high computational complexity in the proposed method are the eigenvalue decomposition of the covariance matrix with the size of $N_{\mathrm{sub}} \times N_{\mathrm{sub}}$, $\mathscr{O}(N_{\mathrm{sub}}^3)$, the SVD of the matrix of size $N_{\mathrm{sub}} - 1 \times 2M$, $\mathscr{O}(\min\{(N_{\mathrm{sub}} - 1)^2 \times 2M, (N_{\mathrm{sub}} - 1) \times 4M^2\})$, (Saarnisaari, 1997) while those in the conventional SVD method, Radon transform method, and S-SVD method are the SVD of the matrix of size $N_{\mathrm{ave}} \times N_{\mathrm{sub}}$, $\mathscr{O}(N_{\mathrm{ave}}^2 \times N_{\mathrm{sub}})$, inversion fo the matrix of size $N_{\mathrm{c}} \times N_{\mathrm{c}}$, $\mathscr{O}(N_{\mathrm{c}}^3)$ and inversion of the matrix of size $N_{\mathrm{k}} \times N_{\mathrm{k}}$, $\mathscr{O}(N_{\mathrm{k}}^3)$, respectively, where N_{c} and N_{k} are the number of sampling points in phase velocity and wavenumber axis, which is normally at least more than 64. Therefore, the SVD method had the smallest computational complexity with the lowest resolution. The computational complexity of the proposed method was significantly smaller than the Radon and S-SVD method.

The calculation time not including loading time for experimental data was less than 0.5 sec with a commercial processor (Core(TM) i7, Intel(R), USA) on a workstation. The calculation time of the conventional Radon transform was less than 60 sec as refer

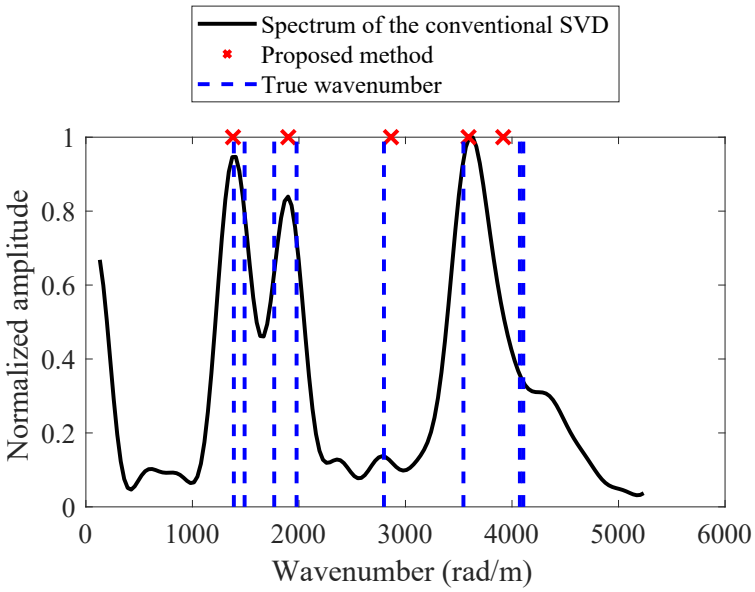

Figure 4.6: Depicted wavenumbers of the proposed method and spectrum of the conventional method at 1.0 MHz. This is the cross sectional view at the white dotted line in Fig. 4.5. The vertical blue dotted line shows the theoretical values.

to Tran et al. (2014b). Note that we do not use the same processor and machine, however, the reduction of 99% of the calculation time is interesting. Moreover, the computational complexity of the S-SVD method is greater than that of the Radon method.

In order to examine the effectiveness of the proposed method in determining M, we compared the proposed method with ESPRIT method with fixed threshold. Figs. 4.7 and 4.8 show the results with a bone plate when we use the eigenvalues that are higher than -40 and -30 dB of maximum eigenvalue. The red circles represent the result of the proposed method. The RMSEs of the conventional methods were 184 and 143 rad/m, respectively. As shown in Fig. 4.7, small threshold makes the estimates unstable. Contrary, the large threshold miss the weak modes. The threshold should be determined manually and the results are severely sensitive to the threshold. Therefore it is difficult to determine it.

4.4 Discussion

We selected a sub-array size of $N_{\text{sub}} = 15$, and we investigated the optimal size. Fig. 4.9 shows the depicted wavenumbers with $N_{\text{sub}} = 5$ and 26. The smaller sub-array missed

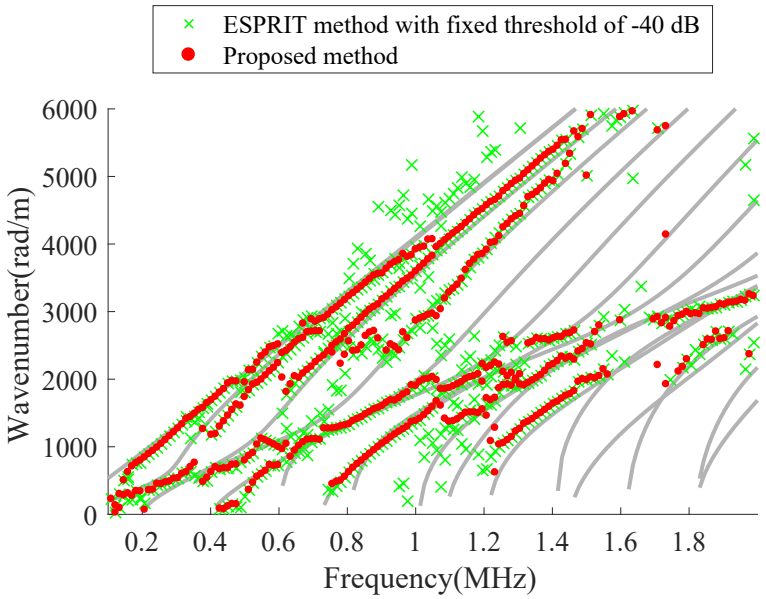

Figure 4.7: Estimated wavenumbers of the 4 mm thick bone-mimicking plate using the conventional ESPRIT algorithm with a fixed threshold of -40 dB and the proposed method. Red dots show the estimates of the proposed method and green cross marks show the that of the conventional method. Solid gray lines show the theoretical curve.

weak modes and the larger sub-array caused false estimates. Fig. 4.10 shows the RMSE with sub-array sizes of $N = 28$ and 32. We can see that the sub-array size $N_{\text{ave}} = N/2$ is optimum. Therefore, $N_{\text{sub}} = 15$ used in the previous section was the optimal size.

In the previous section, we used a frequency window, f_{w}, of 0.5 MHz. The larger value should give a stable estimate. When we employed f_{w} of 0.1 MHz and 0.74 MHz in the experiment with the bone-mimicking plate, the RMSE was 144 rad/m and 118 rad/m, respectively. Thus, the dependence on f_{w} was not significant and a larger window width provided stable estimation.

We chose a DL factor of $\eta_2 = -40$ dB. Because this value was added for stabilization, a smaller value was selected. When we used a larger value, more stable estimates resulted but the weak modes were missed by the method.

As shown in Figs. 4.4 and 4.5, the proposed method and the conventional method both missed some modes. The theoretical curve shows the wavenumber of the modes under ideal conditions. However, realistic propagation depends on the excitation conditions and each mode has a unique transfer function. Thus, we note that we cannot see all

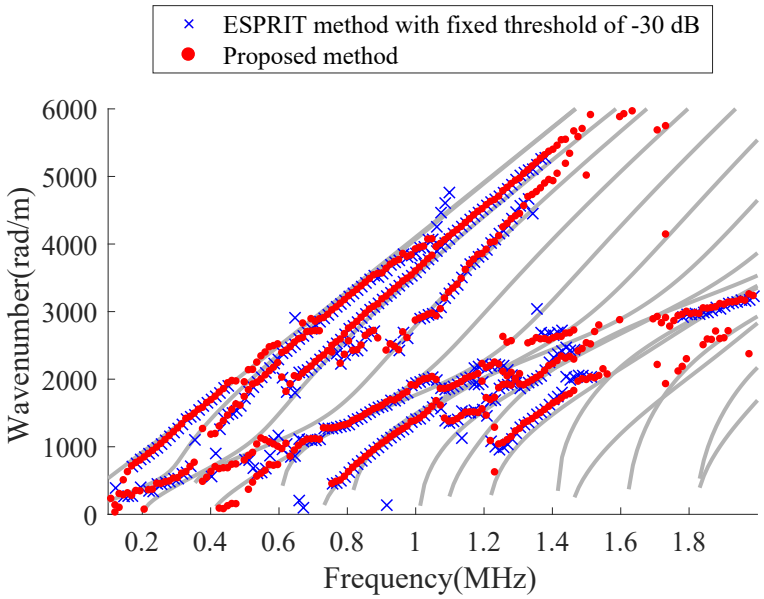

Figure 4.8: Estimated wavenumbers of the 4 mm thick bone-mimicking plate using the conventional ESPRIT algorithm with a fixed threshold of -30 dB and the proposed method. Red dots show the estimates of the proposed method and blue cross marks show the that of the conventional method. Solid gray lines show the theoretical curve.

modes indicated by the theoretical curve.

Figs. 4.11 and 4.12 show the results of the 2D-FFT with copper and bone mimicking plate, respectively. When we compare Fig. 4.4 to Fig. 4.11, we can see that the proposed method and SVD method succeeded in extracting the weak mode. For example, the correct wavenumber is estimated by using the proposed method and SVD method around 0.5 MHz that corresponds to the S0-mode phase velocity, where the conventional 2D-FFT failed to depict the wavenumbers. The curve of the S0-mode is shown in Fig. 4.1.

4.5 Summary and concluding remarks

In this thesis, we proposed a low-computational complexity technique to estimate the number of propagation modes for AT device. We estimated the number of propagation modes using the information theoretic criteria and DL technique. We proposed a method to estimate the optimal value of DL for guided wave characterization. The proposed method did not include processes with high computational complexity. The proposed

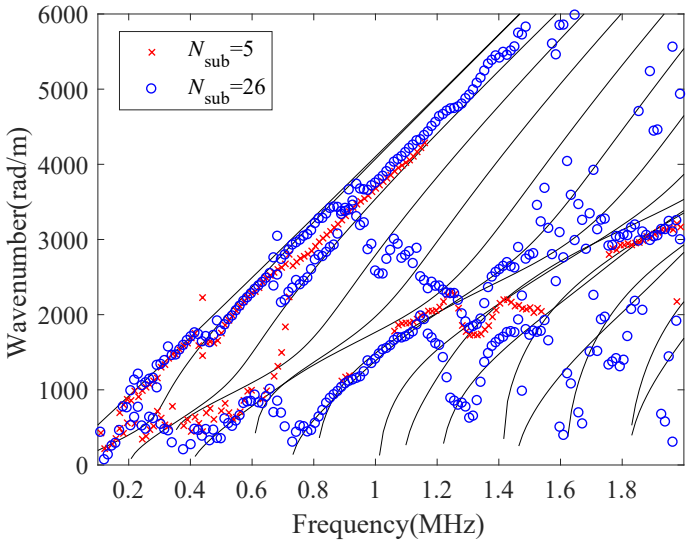

Figure 4.9: Estimated wavenumbers with different sized sub-arrays. Red cross marks and blue circles show the results with $N_{\text{sub}} = 5$ and 26, respectively.

method was experimentally evaluated using 4 mm thick copper and bone-mimicking plates. The estimation error was less than 4% and the calculation time of the proposed method was less than 0.5 sec with a workstation. Although the processor is not same and faster than that used in the conventional study, the calculation time is less than 1% of the conventional method. We believe that our proposed method has potential to accurately characterize the elastic properties of the cortical bone.

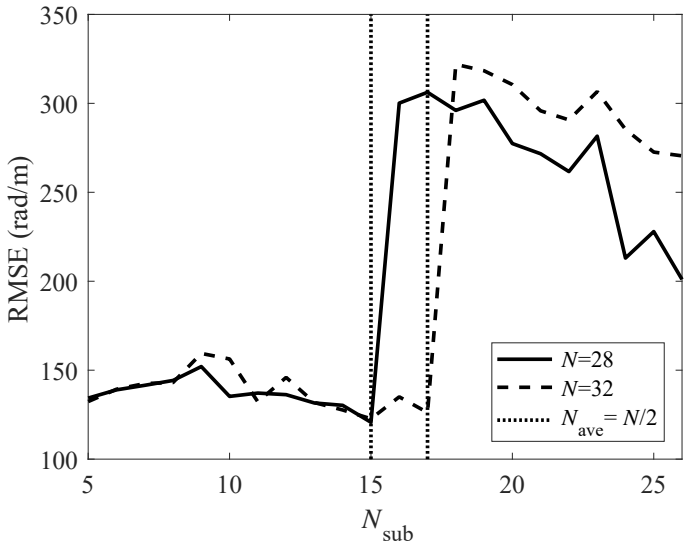

Figure 4.10: Dependence of the proposed method on sub-array size. The black solid line and dotted line show the results with arrays composed of different numbers of receivers. The vertical black dotted line shows the horizontal value with $N_{\mathrm{ave}} = N/2$, i.e., $N_{\mathrm{sub}} - 1 = N_{\mathrm{ave}}/2$.

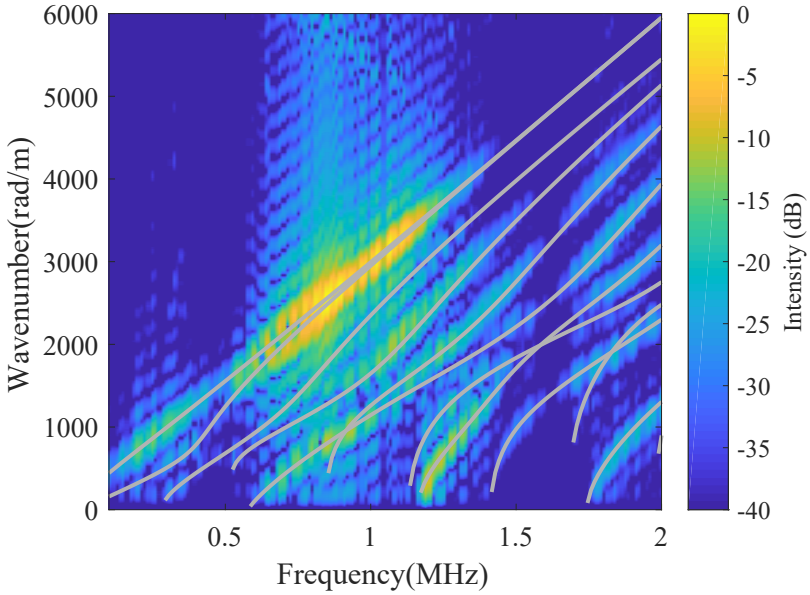

Figure 4.11: Spectrum of the 2D-FFT with 4 mm-thick copper plate. Solid gray lines show the theoretical curve.

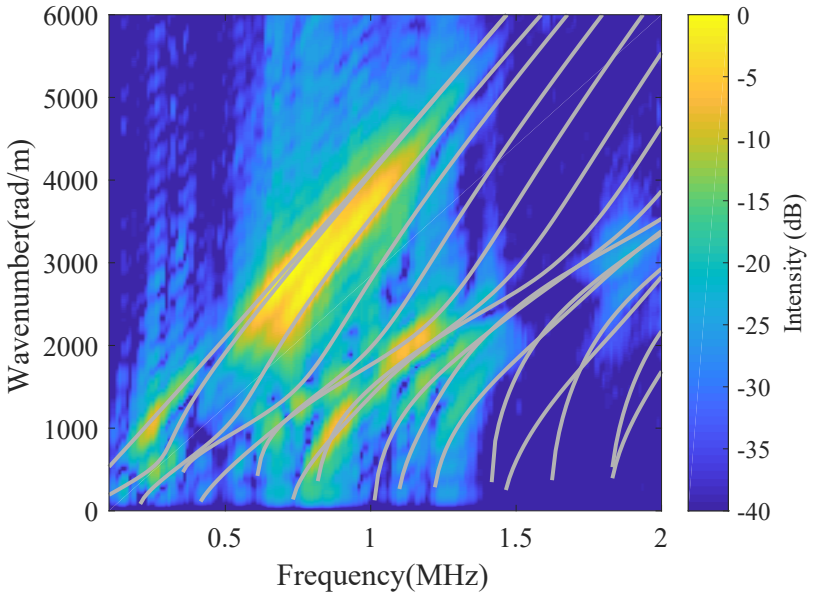

Figure 4.12: Spectrum of the 2D-FFT with 4 mm-bone mimicking plate. Solid gray lines show the theoretical curve.

Chapter 5

Estimation of elastic parameters of homogeneous plates with guided ultrasonic waves using one transmitter and two receivers

5.1 Introduction

As shown in Chap. 3 and 4, and in previous studies, the employment of multiple receivers, transmitters or transmissions that are equivalent to the employment of multiple receivers have been suggested to analyze the guided waves and estimate the properties of bone. However, the reduction of the number of ultrasonic elements would be of interest in order to reduce the cost as much as possible. In this chapter, we focus on the development of the low-cost measurement technique and try to minimize the number of ultrasonic elements used in the system. As the pilot study of the AT technique for bone, we characterize the homogeneous isotropic plate, which is described by a simpler model than that used in Chap. 4.

Several studies have been reported that focus on the low-cost characterization. Tran et al. (2014b) proposed a Radon-transform-based adaptive approach that estimates phase velocity despite missing data. The method worked well with experimental data and should be useful for low-cost assessment. In this chapter, we reduced further the number of receivers. Xu et al. (2012) proposed a technique that employs a single transmitter-receiver pair. The method accurately separates multiple modes of the Lamb wave and estimates the thickness of the metal plate; however, it requires the determination of both the shear wave velocity and longitudinal velocity. Sale et al. (2011) proposed a technique that uses one transmitter and two receivers. Their method characterizes the Lamb wave by minimizing the difference in the group velocities acquired from a semi-analytical

finite element analysis and experimental data. They used a large separation between the transmitter and receivers (350 mm) and between receivers (150 mm) and applied a wavelet transformation to estimate the group velocity. A smaller probe size is desirable when using the AT technique to assess bone quality (Bossy et al., 2004; Naili et al., 2010).

These inversion problems have also been investigated for the air-coupled transducers (Castaings and Hosten, 2001), and the laser-based methods (Gao et al., 2003; Harb and Yuan, 2015, 2016). However, most techniques characterize the plate with multiple angle transmissions (Harb and Yuan, 2015, 2016) or multiple reception events (Castaings and Hosten, 2001; Gao et al., 2003) to eliminate the effects of the multiple modes propagation. In this chapter, to realize a low-cost measurement system, we do not change the positions and angles of transmission and reception.

To minimize the number of elements, we use not only the wavenumbers of the propagation modes but also the transfer function. In addition to the phase velocity, the transfer function, i.e. waveform, of the Lamb wave also strongly depends on the parameters d, c_{S}, and c_{L} (Viktorov, 1967). Therefore, theoretically, parameter values can be estimated by a fitting procedure of the waveform. However, the inversion process leads to a multi-dimensional optimization problem and requires a large computational complexity. A reduction in the computational complexity is as important as the reduction in hardware costs.

In this chapter, we propose a technique that estimates d, c_{S}, and c_{L} using a transmitter and two receivers with a low computational complexity. We transmit a wide-band ultrasound signal from a transmitter. Using two receivers, we can estimate a phase velocity of a single wave by its dependence on the difference between the phases of the received signals. Hence, we first apply the Fourier transform and partially estimate the phase velocity of the dominant wave within a certain frequency range. Next, we solve numerically the Rayleigh–Lamb equation for the frequency using the estimated phase velocity. Finally, we apply the multi-linear least-mean-squares (LLMS) method with the solutions of the previous procedure in the time domain (Taki et al., 2015a). The proposed method is applied with success to numerical (Nguyen and Naili, 2012, 2013) and experimental signals.

5.2 Materials and methods

5.2.1 Partial phase velocity estimation

We first describe the procedure to estimate the phase velocity of a single mode of propagation. Fig. 5.1 shows a schematic illustration of the proposed method for phase velocity estimation with two receivers. We consider a small ultrasonic element attached to the surface of the plate. We label the receiver nearest to the transmitter Rx1 and the receiver furthest away Rx2. With two receivers, we can estimate a single phase velocity of a single propagation mode. With this setup, the A0-mode is the dominant mode in the lower frequency range. The A0-mode is the fundamental mode which shows strong dispersive relation in the lower frequency range. Therefore, we first estimate the phase velocity of the A0-mode within the frequency range where the A0-mode is dominant.

When measuring the phase velocity with two receivers, the received signals are taken to have the form

$$S_i(f) = S_0(f) \exp\left\{\frac{-\mathrm{j}2\pi f l_i}{c(f)}\right\}, \tag{5.1}$$

where $S_0(f)$ is the spectrum of the transmitted signal, $S_i(f)$ is the Fourier-transformed received signal at i-th receiver, l_i is the distance between the transmitter and i-th receiver ($l_1 = l_\mathrm{d}$ and $l_2 - l_1 = l$ are used in this chapter), and $c(f)$ is the phase velocity. Hence, the difference in phase $\phi_\mathrm{t}(f)$ between the two receivers for a single mode of propagation is given by

$$\phi_\mathrm{t}(f) = 2\pi f l / c(f), \tag{5.2}$$

where l is the distance between the two receivers.

In the actual measurements, the phase difference between the two receivers, $\phi(f)$, is calculated from

$$\phi(f) = \angle\{S_1(f) S_2^*(f)\}, \tag{5.3}$$

where the superscripted asterisk denotes complex conjugation. The symbol $\angle$ represents the angle of the signal phase. To connect the $\phi(f)$ smoothly along the frequency direction, we employ the unwrap process (Hu et al., 2014).

The problem is that $\phi(f)$ is not always equivalent to $\phi_\mathrm{t}(f)$ because $\phi(f)$ ranges from 0 to 2π, i.e., $\phi_\mathrm{t}(f)$ can be expressed in terms of $\phi_\mathrm{t}(f) = \phi(f) \pm 2\pi p$, where p is an integer as shown in Fig. 5.1. Therefore, we first define multiple candidate values of the phase velocities with different values of p as follows

$$c_p(f) = 2\pi f l / (\phi(f) + 2\pi p), \tag{5.4}$$

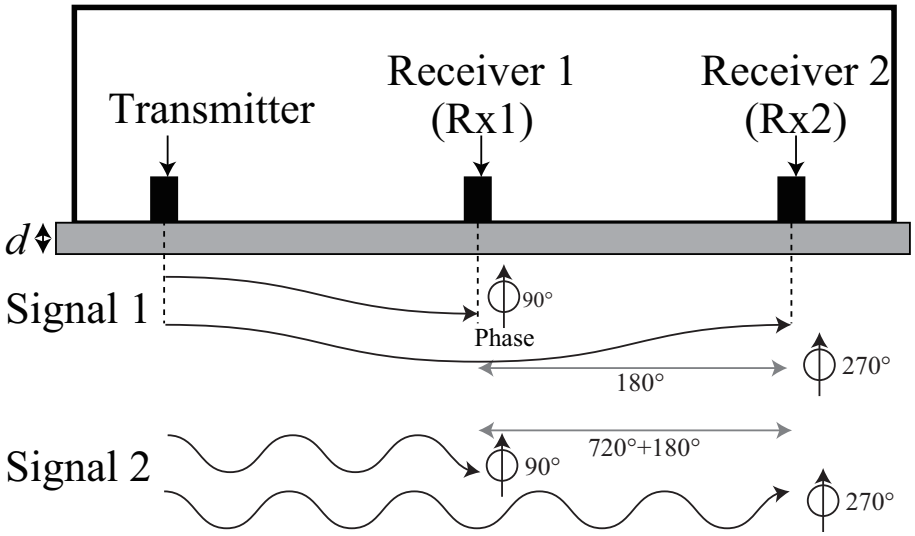

Figure 5.1: Schematic of the phase velocity estimation using two receivers.

where $c_p(f)$ is the p-th candidate of phase velocity. To estimate phase velocity of the A0-mode, we need to determine p and the frequency range where this mode is dominant.

For that purpose, we use characteristics of the phase velocity of the A0-mode. For an isotropic elastic plate, these characteristics are: 1) phase velocity is always positive, 2) it never exceeds c_{S}, 3) its curve increases monotonically with increasing frequency and 4) the slope of its curve monotonically decreases with increasing frequency. The curve of the A0-mode phase velocity is presented in Fig. 1.13. We next select the P_{c} candidate values and frequency ranges that satisfy some particular characteristics. Here let us define the selected A0-mode phase velocities, $c_1^{\mathrm{e}}(f), \cdots, c_p^{\mathrm{e}}(f), \cdots, c_{P_{\mathrm{c}}}^{\mathrm{e}}(f)$. The reason why we do not use all candidate values that satisfy the condition is discussed later in Sect. 5.4.

5.2.2 Inversion process using the Rayleigh–Lamb equations and fitting procedures

With the aforementioned set up, the Lamb wave propagates along the axial direction of the plate. The important point to note is that the phase velocity and transfer function are mainly determined by c_{S}, c_{L}, and d (Núñez et al., 2000).

In the previous step, we obtained estimates of the A0-mode phase velocity. In general, the phase velocities are determined using the Rayleigh–Lamb equation (Eq. (1.70)). In this step, we numerically solve the Rayleigh–Lamb equation to find candidate values of the parameters c_{S}, c_{L}, and d using $c_p^{\mathrm{e}}(f)$.

When solving Eq. (1.70) with the p-th candidate for a given frequency f_q by substituting $c_p^{\mathrm{e}}(f_q)$ into $c(f)$, the solutions trace out a curved surface in c_{S}–c_{L}–d space, see Fig. 5.2(a). With different f, the solutions trace out different curved surfaces. If $c_p^{\mathrm{e}}(f)$ is the exact value sought, the curved surfaces intersect at one point in this candidate space, that point providing the parameter values of the Lamb wave, see Fig. 5.2(b). However, in the measurement, $c_p^{\mathrm{e}}(f)$ is not the exact value and the surfaces do not exactly intersect at one point, see Fig. 5.2(c).

To solve these problems, we solve Eq. (1.70) by successive approximations using incremental values of c_{S}, c_{L}, and d with appropriate intervals. From Fig. 5.2(c), the solution curves approach the "real" values of the parameters. We thus evaluate the degree of concentration of the solution using the weighting function as follows (Illingworth and Kittler, 1988; Sirmacek and Unsalan, 2010):

$$J_p(c_{\mathrm{S}}, c_{\mathrm{L}}, d) = \sum_{q=1}^{Q} w(c_{\mathrm{S}} - c'_{\mathrm{S}}(f_q, c_p^{\mathrm{e}}), c_{\mathrm{L}} - c'_{\mathrm{L}}(f_q, c_p^{\mathrm{e}}), d - d'(f_q, c_p^{\mathrm{e}})), \tag{5.5}$$

where J_p is the degree of concentration when we use c_p^{e}, f_q is the q-th component of frequency, Q is the number of frequency components, $c'_{\mathrm{S}}(f_q, c_p^{\mathrm{e}})$, $c'_{\mathrm{L}}(f_q, c_p^{\mathrm{e}})$, and $d'(f_q, c_p^{\mathrm{e}})$ are the solutions of Rayleigh–Lamb equation Eq. (1.70) with $f = f_q$ and $c = c_p^{\mathrm{e}}(f_q)$, and w is the weighting function. The Gaussian function is used in this chapter.

Finally, we select as candidate values where the degree of concentration exceeds a set threshold such as 75% of the maximum degree of the concentration,

$$\max\{J_p(c_{\mathrm{S}}, c_{\mathrm{L}}, d)\} \times \varepsilon_{\mathrm{v}}, \tag{5.6}$$

where ε_{v} is the threshold value.

In the next step, we employ multi LLMS processes, their number being equal to the number of parameter candidates. The dependence of c_{L} on the phase velocity and waveform is considerably smaller than that of c_{S}. Hence, we select a single c_{L} that maximizes v at each c_{S} and d.

In the previous step, we acquired candidate values for c_{S}, c_{L}, and d. With these values, we can calculate the transfer functions and phase velocities for the various modes of the Lamb wave. Thereby, we finally estimate all parameter values using the fitting procedure in the time domain.

In Sect. 5.2.1, we estimated the phase velocity of a single mode and noted that with two receivers we cannot estimate the phase velocities of multiple propagating modes. Nonetheless, in this step, we consider these multiple modes of propagation. We already

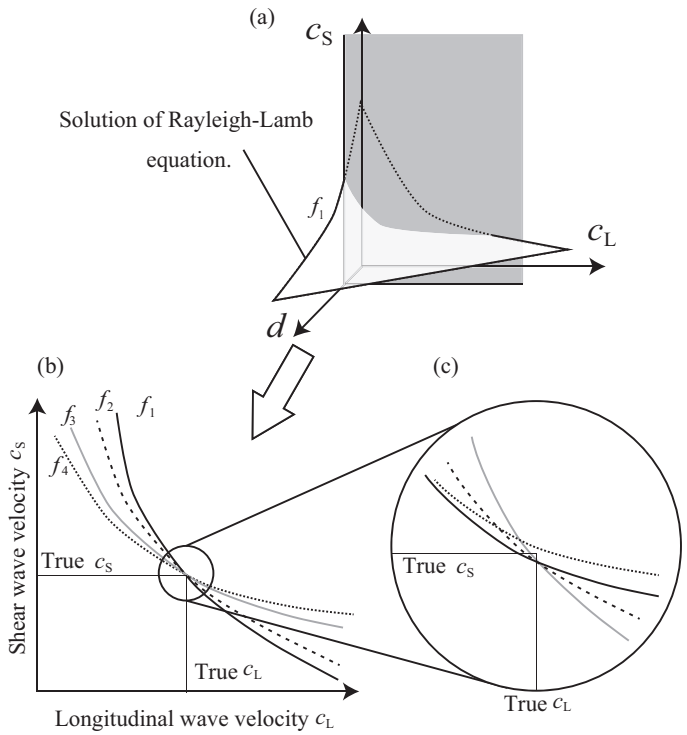

Figure 5.2: Schematic illustration of the iterative process with the candidate estimates of the A0-mode phase velocity. (a) Solution of Rayleigh-Lamb equation with f_1 in d–c_S–c_L space. (b) Solutions in c_S–c_L plane with several f. (c) Detail of solutions. Note that the lines do not intersect at one point.

have the transfer functions and phase velocities of multiple modes of propagation using a set of candidate parameter values. With the transfer functions and phase velocities, we can predict the waveforms of all modes of propagation and the received signals at the two receivers containing these multiple modes of propagation.

We modified the transfer function for the Lamb wave propagating in an isotropic elastic plate reported by Núñez et al. (2000). We introduced a phase rotation factor, which proved to be effective in the fitting procedure using the LLMS method (Cantrell, 2008; Taki et al., 2015a). The procedure for the estimation involves calculating the fitting residue

$$D_i = \int_0^{t_d} |s_i^o(t, A_{i,m}^s, \theta_{i,m}^s, A_{i,m}^a, \theta_{i,m}^a) - s(t)|^2 dt, \tag{5.7}$$

where D_i is the fitting residue of i-th candidate, t_d is the time duration for the fitting procedure, i is the candidate number, s_i^o is the objective function of m-th candidate, and $s(t)$ is the received signal. The quantities $A_{i,m}^s$, $A_{i,m}^a$, $\theta_{i,m}^s$ and $\theta_{i,m}^a$ are optimized

parameters in the LLMS, where $A^{\mathrm{s}}_{i,m}$ and $A^{\mathrm{a}}_{i,m}$ are the signal amplitude parameters of the S and A modes of order m, and $\theta^{\mathrm{s}}_{i,m}$ and $\theta^{\mathrm{a}}_{i,m}$ are the phase rotation factors. Subscripts $^{\mathrm{s}}$ and $^{\mathrm{a}}$ denote the S and A modes. The objective function $s^{\mathrm{o}}_i(t)$ is given by:

$$s^{\mathrm{o}}_i(t, A^{\mathrm{s}}_{i,m}, \theta^{\mathrm{s}}_{i,m}, A^{\mathrm{a}}_{i,m}, \theta^{\mathrm{a}}_{i,m}) = \sum_{m=0}^{M-1} \{s^{\mathrm{s}}_{i,m}(t, A^{\mathrm{s}}_{i,m}, \theta^{\mathrm{s}}_{i,m}) + s^{\mathrm{a}}_{i,m}(t, A^{\mathrm{a}}_{i,m}, \theta^{\mathrm{a}}_{i,m})\}, \tag{5.8}$$

$$s^{\mathrm{s}}_{i,m}(t, A^{\mathrm{s}}_{i,m}, \theta^{\mathrm{s}}_{i,m}) = \mathscr{F}^{-1}[A^{\mathrm{s}}_{i,m} |H^{\mathrm{s}}_{i,m}(f)| S_0(f) \exp\{-\mathrm{j}2\pi f l_{\mathrm{d}} / c^{\mathrm{s}}_{i,m}(f) + \mathrm{j}\theta^{\mathrm{s}}_{i,m}\}], \tag{5.9}$$

where M is the number of modes of propagation used for the estimation, $\mathscr{F}^{-1}$ denotes the inverse Fourier transform, $H_{i,m}(f)$ the transfer function of the i-th candidate given by Núñez et al. (2000), and l_{d} is the distance between transmitter and receiver. For receivers Rx1 and Rx2, the duration t_{d} is respectively 20 and 40 μs. We finally select the candidate that minimizes the fitting residue.

5.2.3 Measurement settings

Figs. 5.3 and 5.4 show a schematic and a photo of the measurement setup. We attach a linear array probe with 128 elements (composite oscillator). We pick up an element as the transmitter and two elements as receivers. The element width in the propagation direction is 0.275 mm and the normal to propagation direction is 10 mm.

In the simulation, we consider an infinite isotropic elastic plate with constant thickness and use the semi-analytical finite element method (Nguyen and Naili, 2012, 2013). We put a point transmitter and two receivers on the plate that reside in free space. The point transmitter and receivers are completely attached to the surface of the plate; i.e., during transmissions, we do not consider the reflection at the surface of the plate.

The plate is characterized by four parameters: mass density, d, c_{S}, and c_{L}. In this chapter, we employed a copper plate: mass density, d, c_{S}, and c_{L} were 8.94 g/cm^3, 2.0 mm, 2260 m/s, 4650 m/s, respectively. Following previous studies, we transmit a wide-band signal with center frequency of 1.0 MHz (Nguyen and Naili, 2012).

The distance between transmitter and Rx1 is $l_{\mathrm{d}} = 20$ mm, and between receivers is $l = 20$ mm. We set the number of A0 candidates used for inversion process to $P_{\mathrm{c}} = 2$, the value used for the thresholding process as $\varepsilon_{\mathrm{v}} = 0.75$, and the number of propagation mode used for fitting procedure to $M = 4$. We solve the Rayleigh–Lamb equation with

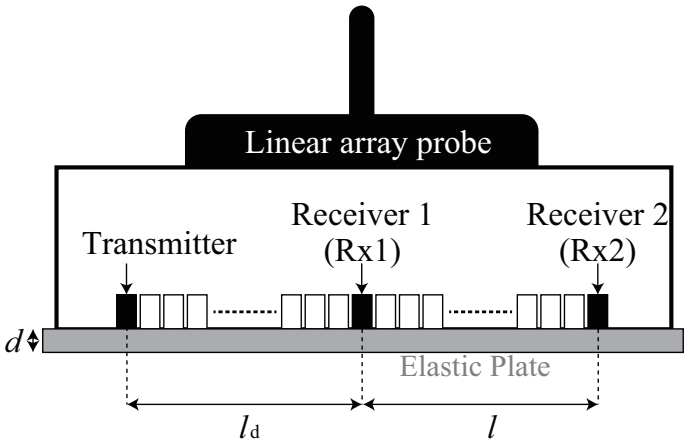

Figure 5.3: Schematic of the system model. The linear array probe consists of 128 elements. We use one element as a transmitter and two elements as receivers.

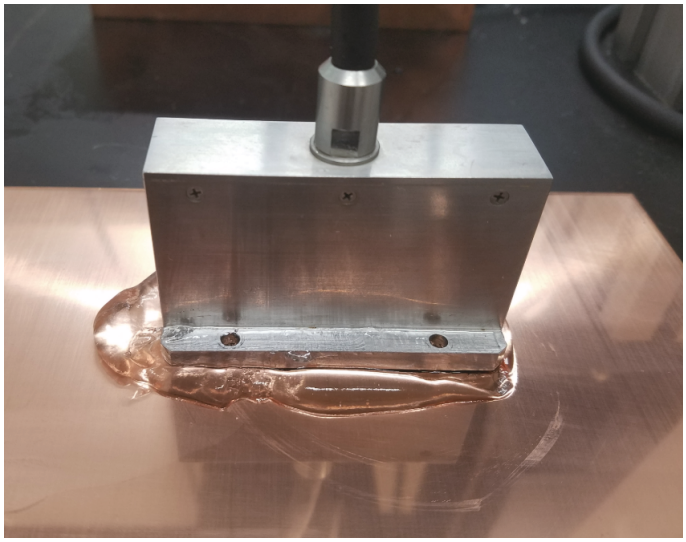

Figure 5.4: Photo of the experimental setup with the linear array probe.

ranges of 2000 m/s $\leq c_S \leq$ 2500 m/s, 3500 m/s $\leq c_L \leq$ 5000 m/s, and 0.5 mm $\leq d \leq$ 6 mm and the incremental values of c_S, c_L, and d are 10 m/s, 10 m/s, and 0.1 mm, respectively. The full-width at half-maximum of the Gaussian weighting function for c_S, c_L, and d is 50 m/s, 50 m/s, and 0.1 mm, respectively. The lowest frequency, f_{min}, used for the estimation of the A0-mode phase velocity in the simulation and in the experiment are 0.2 MHz and 0.5 MHz, respectively.

5.2.4 Algorithm flow

Here, let us summarize the algorithm flow of the proposed method.

1. Transmit a wide-band ultrasonic wave and obtain signals at two receivers at distances l_{d} and $l_{\mathrm{d}}+l$ from the transmitter.
2. Apply Fourier-transform to the signals.
3. Prepare candidate values of the partial A0-mode phase velocity.
4. Select A0-mode candidates.
5. Solve the Rayleigh–Lamb equation for frequency with the incremental values for c_{S}, c_{L}, and d with Gaussian weighting function.
6. Extract parameter values using the threshold condition.
7. Estimate exhaustively parameter values using the LLMS method.

5.3 Results

The results on the tested sample presented in Table 5.1 show the feasibility of the proposed method for estimating the parameters of the plate. The estimated c_{S}, c_{L}, and d include the estimation errors of ± 5 m/s, ± 5 m/s, and ± 0.05 mm, respectively because we set the incremental values of c_{S}, c_{L}, and d of 10 m/s, 10 m/s, and 0.1 mm, respectively. Estimation errors of simulation study are within 0.22, 2.0, and 2.5% for c_{S}, c_{L}, and d, respectively. Those of the experimental study were 0.22, 6.1, and 7.5% respectively. The estimation error is given by the relation

$$|c_{\mathrm{S}}^{\mathrm{t}} - c_{\mathrm{S}}^{\mathrm{e}}|/c_{\mathrm{S}}^{\mathrm{t}} \times 100, \tag{5.10}$$

where $c_{\mathrm{S}}^{\mathrm{t}}$ is the true shear wave velocity and $c_{\mathrm{S}}^{\mathrm{e}}$ is the estimated shear wave velocity. The estimation errors of c_{L} and d are calculated in the same way.

The calculation times for these estimates were 7.0 and 9.0 s for the simulation and experimental study, running a single thread MATLAB program on a commercial CPU (Intel(R) Core(TM) i7-7700K). The calculation time includes execution times for all procedures except for loading times for the received signals and times associated with calculating the transfer functions. Figs. 5.5 and 5.6 show the estimated phase velocities with multiple p and $c_p^{\mathrm{e}}(f)$ of the simulation and experimental study, respectively. The

Table 5.1: Estimated Lamb wave parameters (c_S, c_L, and d) of the proposed method. The estimated c_S, c_L, and d include the estimation errors of ± 5 m/s, ± 5 m/s, and ± 0.05 mm, respectively because we set the incremental values of c_S, c_L, and d of 10 m/s, 10 m/s, and 0.1 mm, respectively.

	Fitting residue (dB)	c_S (m/s)	c_L (m/s)	d (mm)
Real value		2260	4650	2.0
Simulation	-10.3 (Rx1), -10.0 (Rx2)	2260	4560	2.0
Experiment	-8.1 (Rx1), -6.9 (Rx2)	2260	4370	2.1

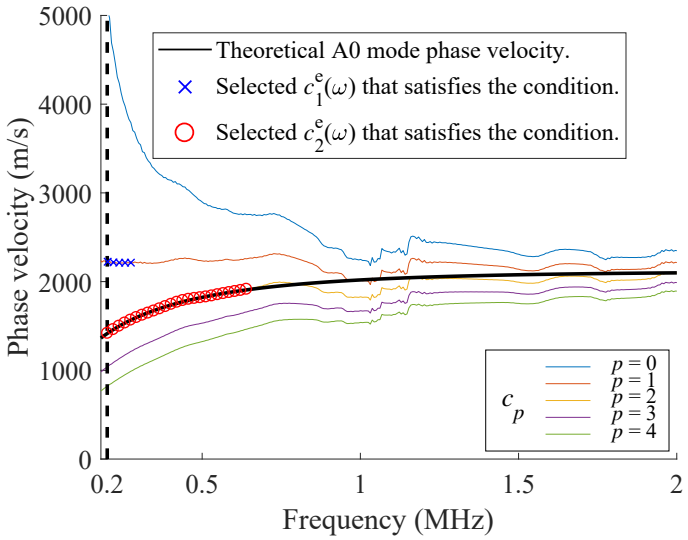

Figure 5.5: Estimated A0-mode phase velocities in the numerical simulation study with multiple p, $c_p(f)$ (solid colored lines), selected phase velocities $c_1^e(f)$ (blue crosses) and $c_2^e(f)$ (red circles) based on the A0-mode characteristics and theoretical A0-mode phase velocity (black solid line). The vertical dotted line shows the lowest frequency for the A0-mode phase velocity estimation.

red circles and blue crosses indicate the prepared candidate values used in the subsequent steps, i.e., $c_1^e(f)$ and $c_2^e(f)$. We see that one of the candidates matches well the theoretical curve (solid black line).

With $c_2^e(f)$ obtained from the simulation and experimental results, the corresponding Figs. 5.7 and 5.8 show the degree of concentration that is defined at Eq. (5.5), $J_2(c_S, c_L, d)$, obtained solving numerically Eq. (1.70) for the frequency. Note that the

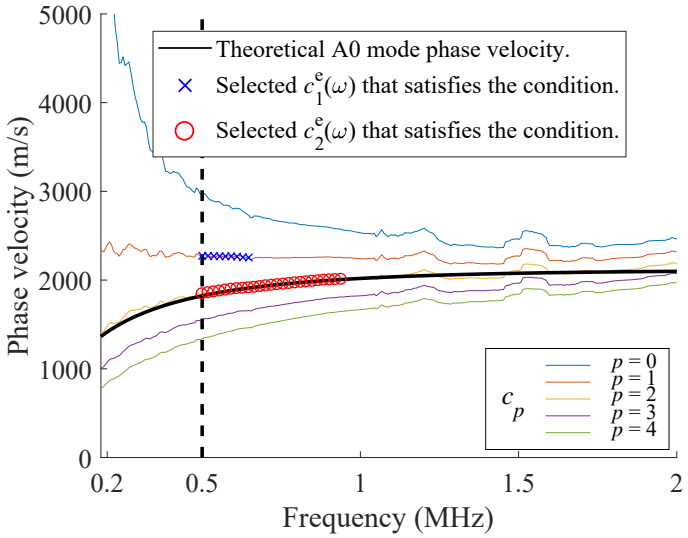

Figure 5.6: Estimated A0-mode phase velocities in the experimental study with multiple p, $c_p(f)$ (solid colored lines), selected phase velocities $c_1^{\mathrm{e}}(f)$ (blue crosses) and $c_2^{\mathrm{e}}(f)$ (red circles) based on the A0-mode characteristics and theoretical A0-mode phase velocity (black solid line). The vertical dotted line shows the lowest frequency for the A0-mode phase velocity estimation.

actual interval for the increment thickness is 0.1 mm. For simplicity, we show the results with interval of 0.5 mm. We see that the degree of concentration increases around the true parameter values marked by the black diamonds for thickness close to 2 mm.

Figs. 5.9 and 5.10 show the fitted results from the simulation and experiment, respectively. The predicted waveforms matched the received signals well.

5.4 Discussion

When we calculate transfer functions for Lamb wave, we need to provide a density of the material. However, as shown in Núñez et al. (2000), the density only affects the amplitude. Because the LLMS procedure determines the amplitudes of the propagation modes as shown in Eqs. (5.8) and (5.9), the provided density theoretically does not affect the results. In other words, if we use an arbitrary value of the density for the transfer function calculation, the proposed method will give the same estimates. Therefore the proposed method does not require any specific information of the plate.

We succeeded in accurately estimating the received signal using theoretical transfer function and LLMS method. The results show that using LLMS with the phase rotation

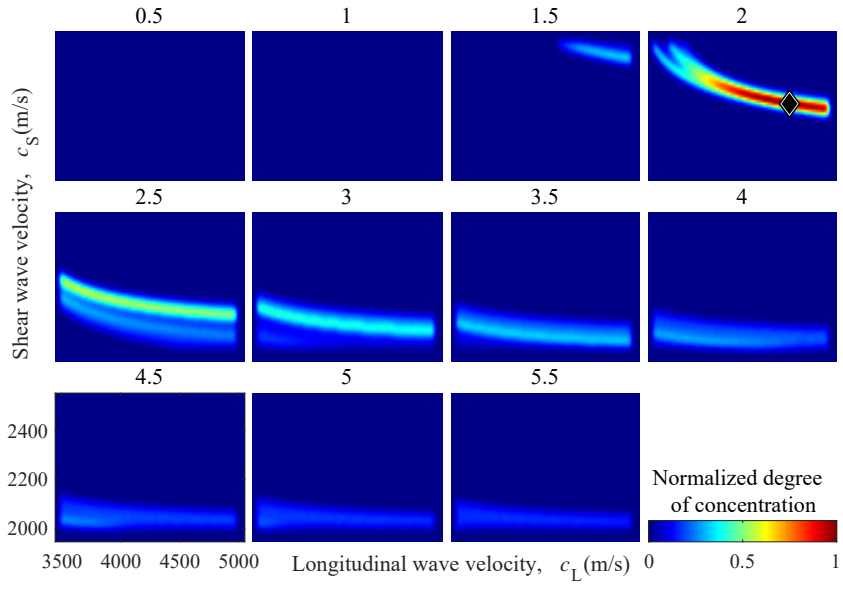

Figure 5.7: Normalized degree of concentration for each incremented thickness obtained from numerical simulation study. The vertical and horizontal axes correspond to c_S and c_L, respectively. The value above each figure is the plate thickness d [in mm]. The black diamond represents the position of true parameters.

factor shown in Eq. (5.9) is appropriate to estimate the properties of Lamb wave. In addition, a reduction in the number of the candidates might help to accurate estimation. When we employ a non-linear fitting procedure, there is a possibility that the fitting result is a localized solution and the solution does not represent the true parameters.

Because we can estimate only a single phase velocity of a single propagation mode with two receivers, we measured the characteristic of the A0-mode that dominates the lower frequency range using two receivers. To compare the intensity of the A0-mode with that of the other modes, we apply a 2D-FFT to the signal waveforms obtained from simulation and the experimental study. Figs. 5.11 and 5.12 show the results of a 2D-FFT of the simulation and experimental data. In obtaining these images, we used 78 receivers having an element pitch of 0.375 mm. Note that the A0-mode dominates at the low frequency range in both datasets. Hence, we can estimate the A0-mode phase velocity with two receivers. We reiterate that, in the fitting procedure, we used the higher order modes, see Sect. 5.2.2.

In the A0-mode phase velocity selection (procedures 3 and 4 introduced in Sect. 5.2.4), we used $P_c = 2$. A larger value stabilizes the estimation. Fig. 5.13 shows the estimated A0-mode phase velocity with $l = 12$ mm. In Figs. 5.5 and 5.13, the respective

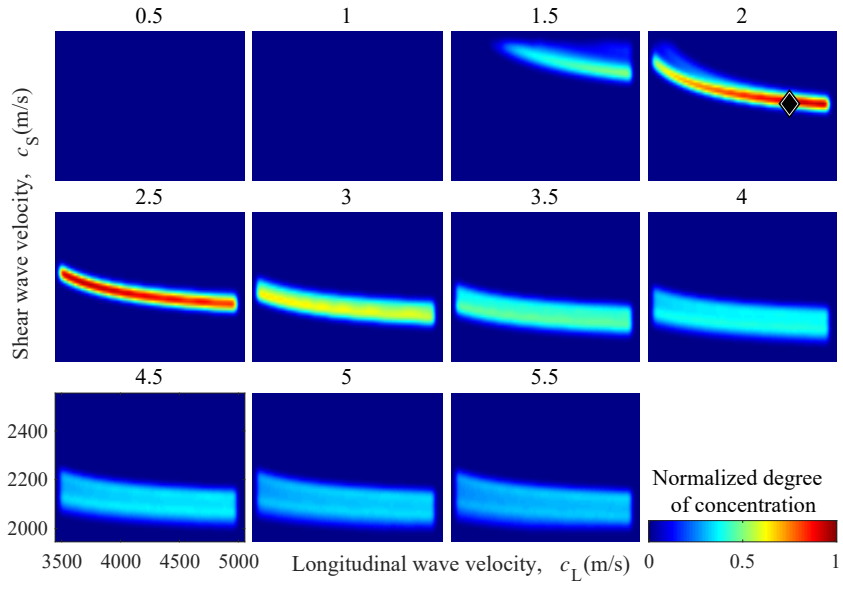

Figure 5.8: Normalized degree of concentration for each incremented thickness employed in the experimental study. The vertical and horizontal axes correspond to c_S and c_L, respectively. The value above each figure is the plate thickness d [in mm]. The black diamond represents the position of true parameters.

curves of $c_2^e(f)$ and $c_1^e(f)$ show that they match well with the theoretical curves. Thus, a multiple selection of candidate values for the A0-mode phase velocity, i.e., $P_c > 1$, is desirable for robust estimation. Using unsuitable candidates, i.e., those marked by red circles in Fig. 5.13, the degree of concentration increases at unsuitable parameter values as shown in Fig. 5.14. With unsuitable parameter values, the predicted waveform is completely different (Fig. 5.15) and the fitting procedure removes these unsuitable parameters. Hence, there is no problem in selecting multiple p from the viewpoint of robustness. However, larger values of P_c also extends the calculation time. Therefore a trade-off is necessary that depends on the requirement of the system and application.

To assess the effect of l, we set $l = 10$ and 25 mm and compare the results. The results are shown in Figs. 5.16 and 5.17, where with Eq. (5.4), the difference in c_p diminishes when we select larger value of l. This makes the selection of the "correct" A0-mode phase velocity more difficult to reach, and a larger value of P_c is required to select multiple A0-mode phase velocity candidates. Additionally, in the experimental study, SNR at the second receiver decreases. However, when we use smaller value of l, the estimation becomes unstable because the A0-mode is estimated from the difference between the two signals. With $l = 10$ mm, we succeeded in estimating parameter values with errors

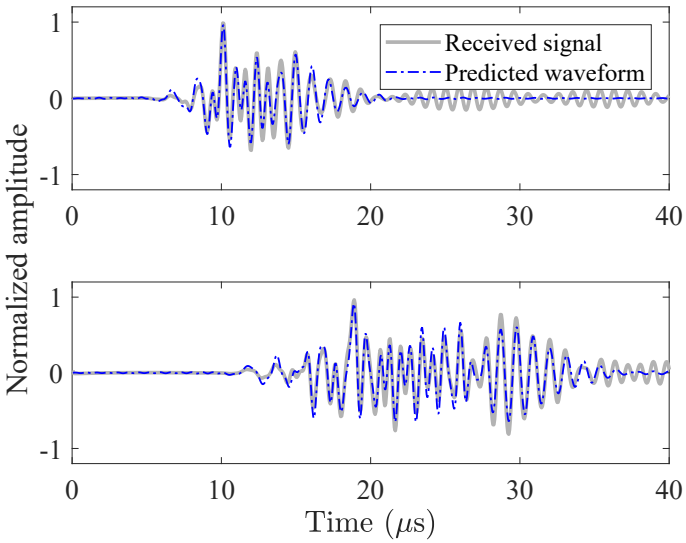

Figure 5.9: Received signals (gray solid line) and predicted waveforms (blue dotted line) at Rx1 (upper panel) and Rx2 (lower panel) in the numerical simulation study. The sizes of the time windows used in the fitting process, t_{d}, were 20 and 40 μs for Rx1 and Rx2, respectively.

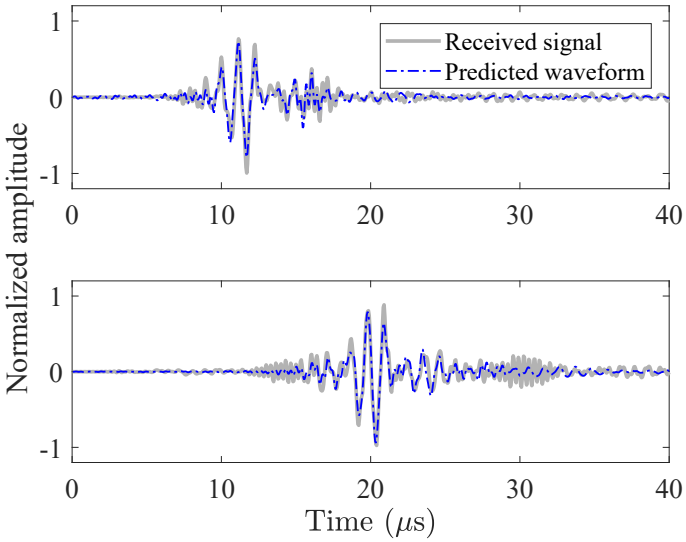

Figure 5.10: Received signals (gray solid line) and predicted waveforms (blue dotted line) at Rx1 (upper panel) and Rx2 (lower panel) in the experimental study. The sizes of the time windows used in the fitting process, t_{d}, were 20 and 40 μs for Rx1 and Rx2, respectively.

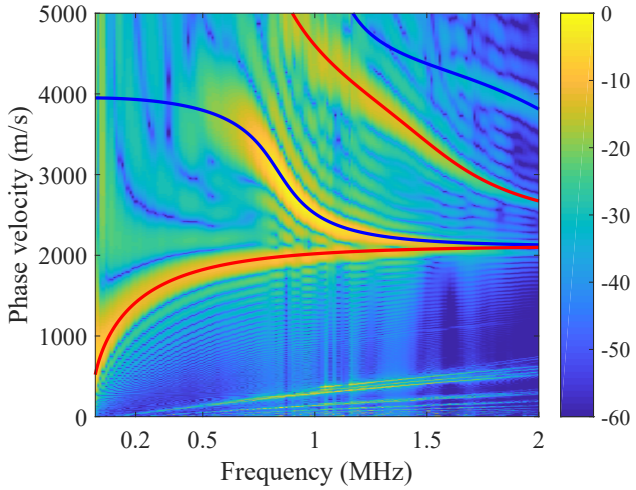

Figure 5.11: Results from a 2D-FFT of signals from 78 receivers in a simulation study. The color map gives the intensity of the signal and solid red and blue lines show theoretical curves for the A and S modes. Note the scale is in dB units.

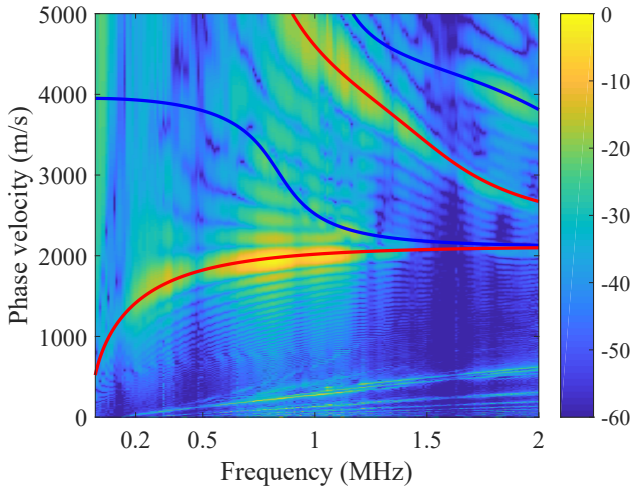

Figure 5.12: Results from a 2D-FFT of signals from 78 receivers in the experimental study. The color map gives the intensity of the signal and solid red and blue lines show theoretical curves for the A and S modes. Note the scale is in dB units.

of 12.5% or less, although, the error is larger. With $l = 25$ mm, we failed to estimate the

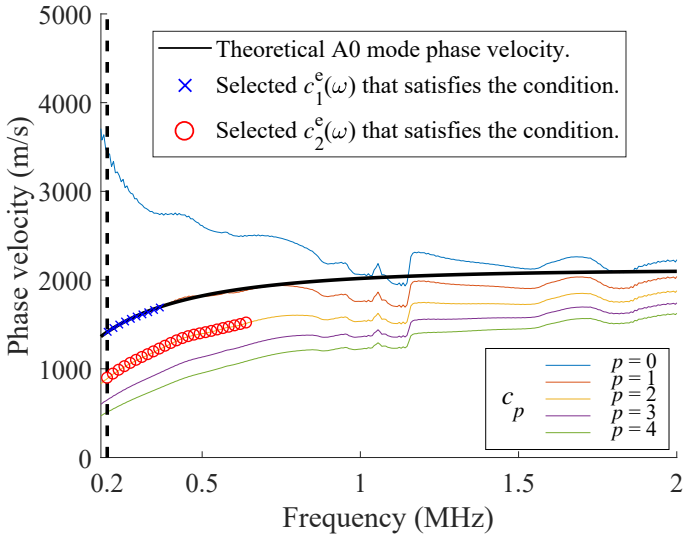

Figure 5.13: Estimated A0-mode phase velocities with $l = 12$ mm in the simulation study.

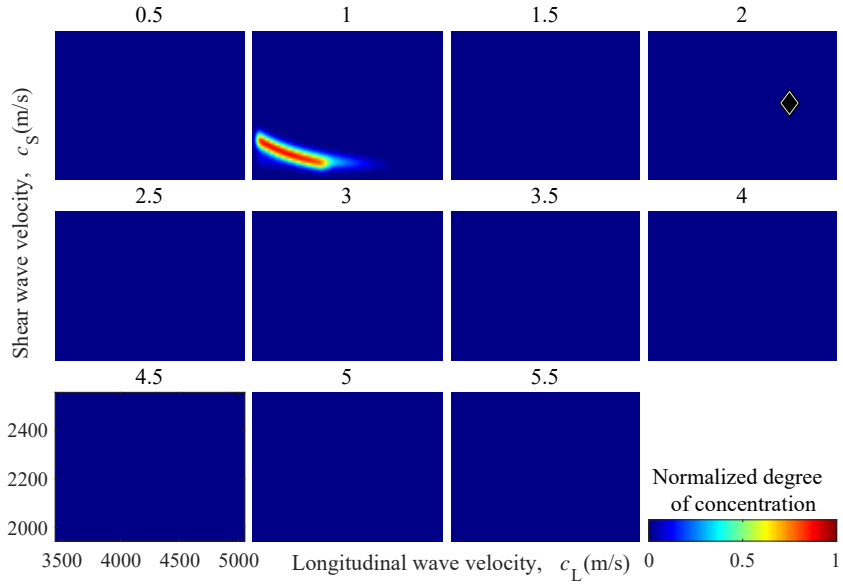

Figure 5.14: Normalized degree of concentration at each thickness when using an unsuitable A0-mode phase velocity candidate (red circles in Fig. 5.13). The black diamond represents the position of true parameter.

parameter values. To shorten the measurement aperture, a smaller value of l_d is desired. However, with values of l_d that are too small, the fitting accuracy decreases because

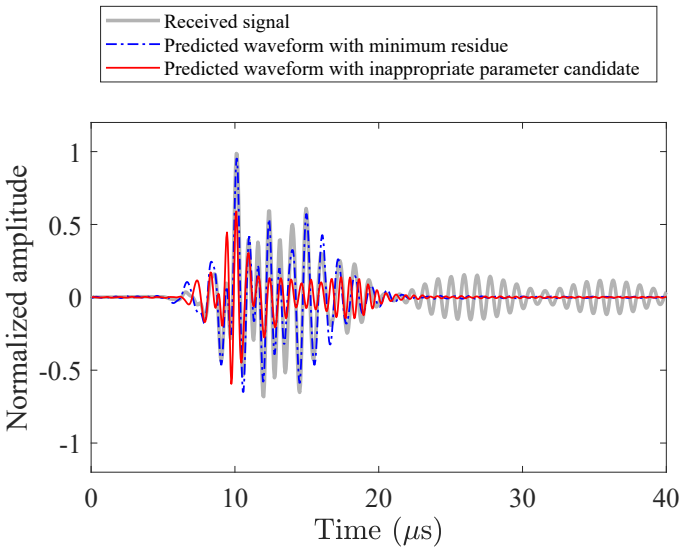

Figure 5.15: Received signal at the Rx1 (gray solid line) at 20 mm, predicted waveform with minimum fitting residue (blue dotted line), and predicted waveform with an unsuitable parameter candidate (red line).

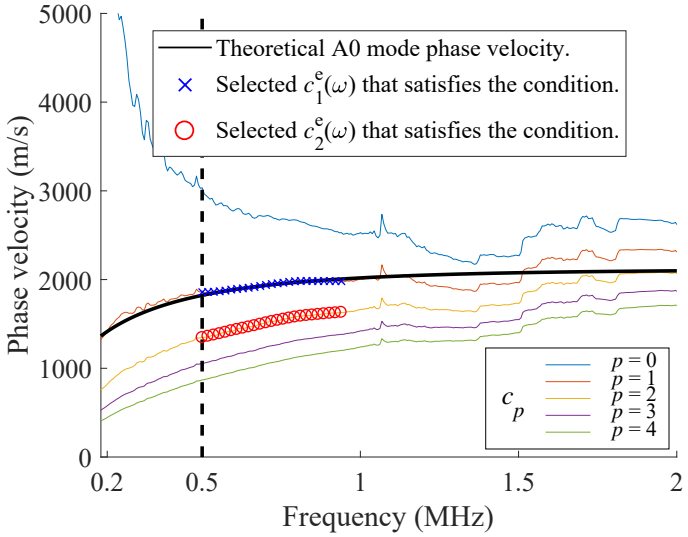

Figure 5.16: Estimated A0-mode phase velocities with $l = 10$ mm obtained from the experimental study.

the received signal does not include enough effects of the multiple propagation modes with multiple different phase velocities. Thus, for the sample tested in this chapter, we empirically determined $l_{\mathrm{d}} = 20$ and $l = 20$ mm.

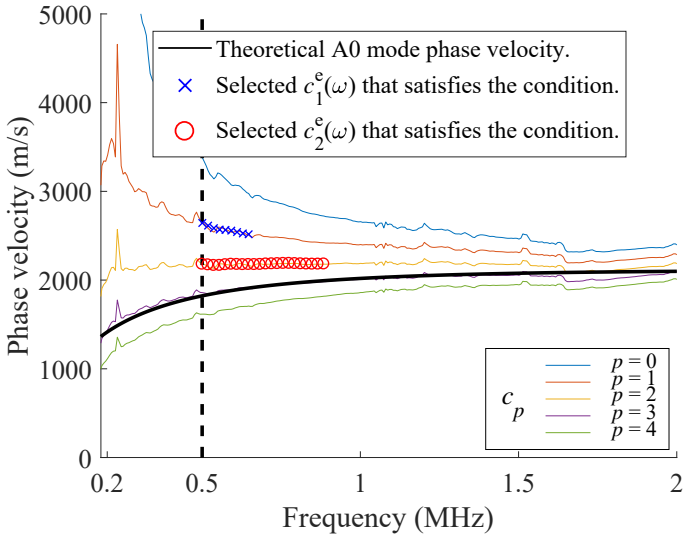

Figure 5.17: Estimated A0-mode phase velocities with $l = 25$ mm obtained from the experimental study.

The error for the estimated slow wave velocity, c_{S}, is smaller than that of the longitudinal wave velocity c_{L} and thickness d. The reason is that the phase velocity and waveform of the Lamb wave strongly depends on c_{S}. This dependence is larger than that for c_{L} and d. Fig. 5.18 shows the dependence of the phase velocities on the product of the frequency and thickness for different settings. The red solid line corresponds to results for a copper plate; the blue solid and black dashed lines correspond to calculations using 10% smaller velocities for c_{S} and c_{L}, respectively, for the copper plate. Note that the thickness d changes the scale of the abscissa. From Fig. 5.18, we see the phase velocity has a stronger dependence on c_{S}. In the proposed method, we calculated the c_{S} and c_{L} at intervals of 10 m/s and d at intervals of 0.1 mm. However, the sensitivities of these three parameters are different and c_{S} has the higher sensitivity.

This is also the reason why we set a narrower range for c_{S} candidates than for c_{L} candidates. When we measure a phase velocity that has a wide range of c_{S}, the proposed method is able to provide the same results but the calculation time should be longer.

In the A0-mode phase velocity estimation procedure, we manually determine the lowest frequency, f_{min}, used for the estimation. The A0-mode is dominant in the lower frequency range, however, the excitation of low frequency such as around 0.1 MHz with the ultrasonic elements used in this chapter is difficult and the SNR decrease severely. Thus, we use the frequency component that is higher than f_{min}. From Fig. 5.18, the A0-mode has high sensitivity to changes in the elastic parameter (Rogers, 1995), i.e., a small error in the A0-mode phase velocity estimation causes a large estimation error in the elastic

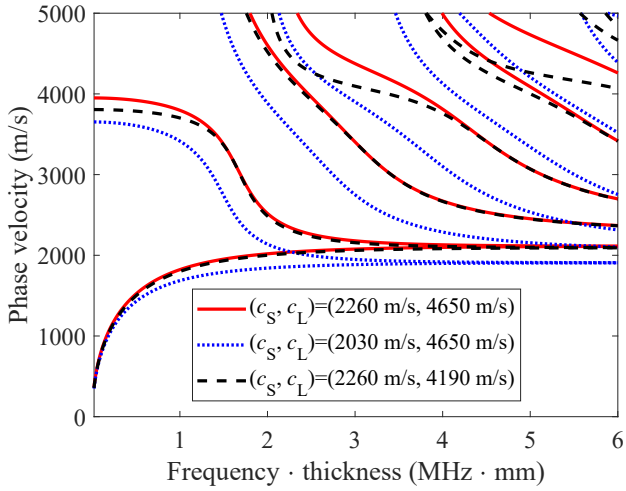

Figure 5.18: Phase velocities with three different elastic parameter settings.

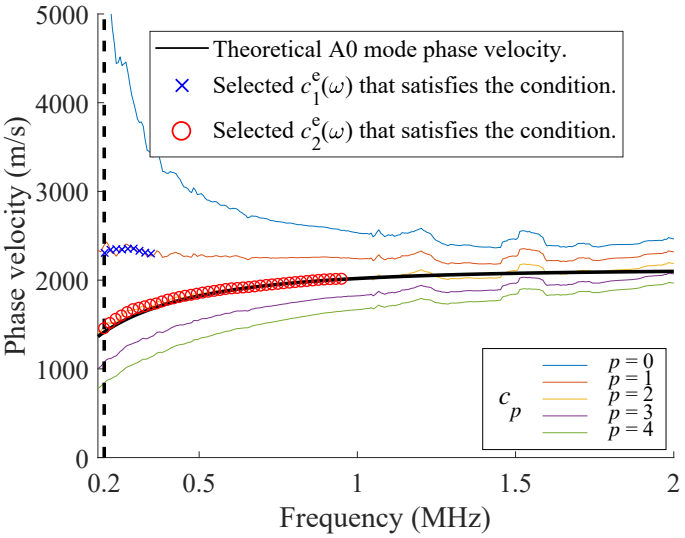

Figure 5.19: A0-mode phase velocity estimation results with $f_{\min} = 0.2$ MHz obtained from experimental data.

parameter estimation. Therefore, selecting a frequency with a sufficiently high SNR is required. This is why we selected $f_{\min} = 0.5$ MHz in the experiments and employed an evaluation process of degree of concentration and fitting procedure rather than using just the A0-mode phase velocity and inversion results from the Rayleigh–Lamb equation.

To show the dependence of the proposed method on $f_{\min}$, we evaluated the results setting $f_{\min} = 0.2$ MHz, see Figs. 5.19 and 5.20. This is the same parameter setting as

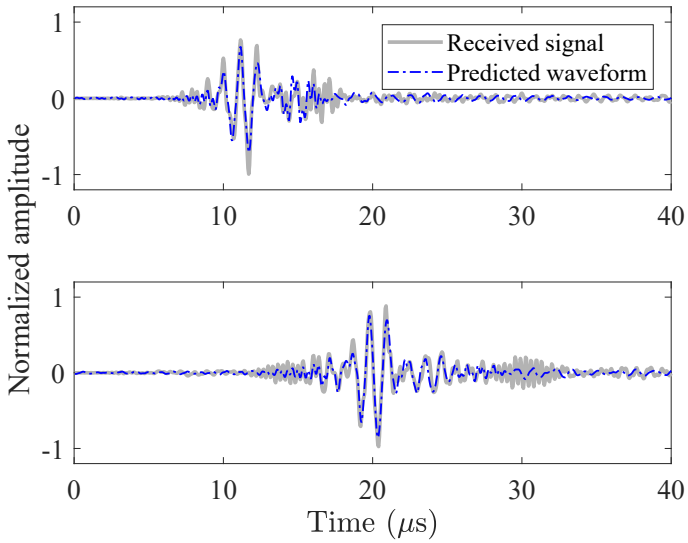

Figure 5.20: Fitting results with $f_{\min} = 0.2$ MHz obtained from experimental data.

used for the numerical simulation. The estimated parameter values (c_S, c_L, d and fitting residues) at Rx1 and Rx2 are (2240 m/s, 4830 m/s, 2.1 mm, and -7.6 dB) and (2250 m/s, 4090 m/s, 2.3 mm, and -6.8 dB), respectively. The estimation errors are higher than those with $f_{\min} = 0.5$ MHz. However, when we select the estimated result at the receiver with the smaller fitting residue, the estimation error is 7.5% or less.

We see that employing the lower frequency yields a lower SNR, making estimations slightly unstable. However, when we employ a thicker plate, a lower frequency range is required because multiple propagating modes appear even in the low-frequency components compared with the propagation modes with a thinner plate. Figs. 5.21 and 5.22 show the experimental results for a 4-mm-thick copper plate. We see that the frequency components higher than 0.5 MHz interfere through couplings among the higher-order modes. Hence, we need to use lower $f_{\min}$. With $f_{\min} = 0.2$ MHz, the estimated parameters(c_S, c_L, d and fitting residues) are (2270 m/s, 4670 m/s, 4.3 mm, and -10.6 dB) and (2360 m/s, 3540 m/s, 4.8 mm, and -4.3 dB), respectively. The error at the receiver with smaller residue is 8.8% or less. The estimation is slightly unstable compared with that for the thin plate; nevertheless, the estimation error remains small at the receiver with smaller residue.

With these results, we conclude that the proposed method does not strongly depend on the parameter settings shown in Sect. 5.2.3, but has limitations when measuring thicker plates as we are unable to register the A0-mode at frequencies with sufficiently high SNR.

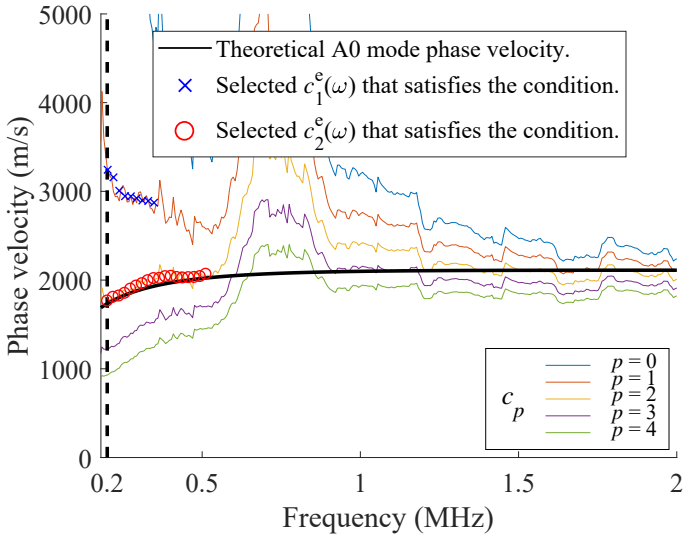

Figure 5.21: Estimated phase velocities for a 4-mm-thick copper plate obtained from experimental data.

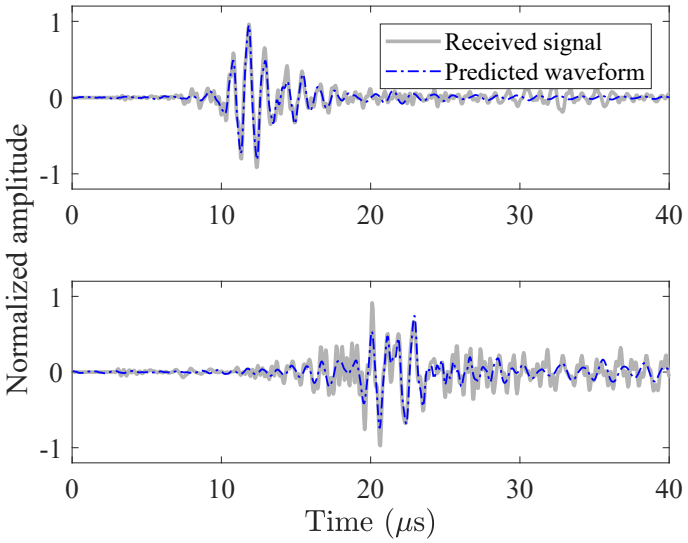

Figure 5.22: Fitting results for a 4-mm-thick copper plate obtained from experimental data.

In this chapter, we used the phase velocity of the A0-mode. We emphasize that there is no limitation to the geometry and dominant mode. The one need only record the dominant wave in certain frequency range and regardless of whether it is a symmetric or anti-symmetric mode and it is a plate or cylinder, the proposed method might work just

as well.

5.5 Summary and concluding remarks

A reduction in the number of transmitters and receivers and the computational complexity is desired for AT devices. We reported a method that characterizes the Lamb wave and estimates plate thickness and both longitudinal and shear wave velocities with estimation errors of 7.5% or less, with the 2-mm-thick copper plate using a single transmitter and two receivers without changing the positions and angles of elements having small measurement aperture size. The distances between the transmitter and the first and second receivers were 20 and 40 mm, respectively, and the central frequency of the transmitted signal was 1.0 MHz. The calculation time when using a single thread MATLAB platform program was 9.0 s or less. The recording aperture of the probe used with our method is reasonable. Its advantages include requiring a minimal number of transmitters and receivers and concurrent estimates of the parameter values obtained at low computational complexity. The proposed method may therefore be gainfully used in testing techniques desiring high efficiency at low computation cost. Moreover, the extension of the proposed method to other types of guided waves is straightforward. The reduction of the calculation time is not enough for the real time assessment. However, the calculation time would be reduced by the multi-thread computation.

In this chapter, we showed the possibility of the low-cost characterization of the guided wave propagating in the homogeneous isotropic plate as the pilot study for the AT technique. Because the model used in this chapter is simpler than the transversely isotropic plate model which is used in Chap. 4, modifications are necessary to expand this technique for the bone quality analysis. For example, the transversely isotropic plate has the three different velocities; two longitudinal wave velocities and a shear wave velocity, where the homogeneous isotropic plate has a single longitudinal velocity and a single shear wave velocity. Additionally, to employ the fitting procedure, we need to consider the effect of the attenuation. Therefore, in the fitting procedure, we might need to employ higher dimensional fitting procedures. These modifications might require higher computational complexity. However, there should be a possibility to characterize the cortical bone with the smaller number of the receivers.

Chapter 6

Concluding remarks

In this thesis, we have proposed array signal processing techniques for medical ultrasound B-mode imaging and the axial transmission technique for cortical bone assessment. We focused on achieving a high-accuracy measurement technique with a comparatively low computational complexity and hardware cost.

In Chap. 2, we proposed a modified beam-space (BS) Capon method for high-resolution and low-computational complexity imaging. Many of the conventional medical ultrasound imaging systems using adaptive beamforming techniques involve substantial computational complexity, which is required to compensate for the difference between the theories that assume a narrow-band signal condition and the actual situation where wide-band signals are used. To reduce the computational complexity, we replaced the time-delay process which increases the computational complexity by the multiplication of a steering vector and a covariance matrix. The time-delay process is employed in the wide-band signal processing and the multiplication of the vector and matrix is used in the narrow-band signal processing. Because the difference between the wide and narrow-band signal processing is small when the measurement point is not far from the focal point, the replacement is effective. In an experiment, the proposed method was successful in separately depicting two closely positioned wire-targets, with a faster calculation than achievable with the conventional BS Capon method.

In Chap. 3, we used a linear array probe for axial transmission technique that characterizes the plate properties. Locally, the cortical bone can be recognized as the transversely isotropic plate. The axial transmission technique normally estimates the wavenumbers of multimodal ultrasonic guided waves. To estimate the wavenumbers, we utilized the ESPRIT algorithm, which separates multiple signals by employing eigenvalue decomposition and estimates the wavenumber numerically, without a peak search process along the intensity profile. The exact values of the wavenumbers, not the profile, are required in the inversion process which estimates the properties of the bone. To employ the ESPRIT method, estimation of the number of propagation modes existing at

the measurement frequency is required. To estimate this, we situated the multiple sizes of sub-arrays in the whole array and evaluated the consistency of the results. We succeeded in widening the measurement frequency range and estimating the wavenumbers accurately.

In Chap. 4, we proposed a low-computational complexity technique to estimate the number of propagation modes for an axial transmission device. In Chap. 3, we used multiple sizes of sub-arrays in the proposed method. However, this process deteriorated the resolution and increased the computational complexity, as the maximum resolution depended on the minimum sub-array size and multiple eigenvalue decompositions, which resulted in a high computational complexity. Thus, we estimated the number by using information theoretic criteria. The estimation results of the information theoretic criteria can be stabilized by the diagonal loading technique, which adds an offset value to the eigenvalues of the covariance matrix. This estimation of the number of signals by the information theoretic criteria has a considerably lower computational complexity than the eigenvalue decomposition. The proposed method was evaluated in an experiment with a bone-mimicking plate. We succeeded in accurately estimating the wavenumber of the bone-mimicking plate with a lower computational complexity.

In Chap. 5, we tried to minimize the number of receivers and transmitters. As the pilot study for the axial transmission technique, a characterization technique for ultrasonic guided waves propagating along a homogeneous isotropic elastic plate, which is a simpler model than the model for the cortical bone was proposed. We used a single element as the transmitter and two elements as receivers. We also reduced the calculation complexity. We used two receivers for the single wavenumber estimation of a single propagation mode and estimated the properties of the plate by using the characteristics of the ultrasonic guided waves. The conclusive characterization was conducted by the linear least squares method, which has a low computational complexity with the use of the modified transfer function. The method succeeded in estimating the thin plate properties with a high accuracy and low hardware cost and computational complexity. Compared to the proposed method showed in Chap. 4 which succeeded in characterizing the bone-mimicking plate, the proposed method shown in Chap. 5 should require modification of the theoretical model and consideration of the attenuation to characterize the bone quality.

The results described in this thesis demonstrate that the proposed techniques show promise for obtaining accurate medical ultrasound measurements at a low-cost and high-resolution. However, the results do not include in-vivo and in-vitro experiments with real tissues. Additional experiments on real tissues and modification of the proposed algorithm for the realistic clinical situation will be the focus of future work.

Bibliography

Abe, H., G. Caracciolo, A. Kheradvar, G. Pedrizzetti, B. K. Khandheria, J. Narula, and P. P. Sengupta, 2013: Contrast echocardiography for assessing left ventricular vortex strength in heart failure: a prospective cohort study. *European Heart Journal–Cardiovascular Imaging*, **14 (11)**, 1049–1060.

Alleyne, D., and P. Cawley, 1991: A two-dimensional Fourier transform method for the measurement of propagating multimode signals. *The Journal of the Acoustical Society of America*, **89 (3)**, 1159–1168.

Berger, M., A. Haimowitz, A. Van Tosh, R. L. Berdoff, and E. Goldberg, 1985: Quantitative assessment of pulmonary hypertension in patients with tricuspid regurgitation using continuous wave Doppler ultrasound. *Journal of the American College of Cardiology*, **6 (2)**, 359–365.

Biot, M. A., 1956a: Theory of propagation of elastic waves in a fluid-saturated porous solid. I. Low-frequency range. *The Journal of the Acoustical Society of America*, **28 (2)**, 168–178.

Biot, M. A., 1956b: Theory of propagation of elastic waves in a fluid-saturated porous solid. II. Higher frequency range. *The Journal of the Acoustical Society of America*, **28 (2)**, 179–191.

Biot, M. A., 1962: Mechanics of deformation and acoustic propagation in porous media. *Journal of Applied Physics*, **33 (4)**, 1482–1498.

Bochud, N., Q. Vallet, J.-G. Minonzio, and P. Laugier, 2017: Predicting bone strength with ultrasonic guided waves. *Scientific Reports*, **7**, 43 628.

Bossy, E., M. Talmant, M. Defontaine, F. Patat, and P. Laugier, 2004: Bidirectional axial transmission can improve accuracy and precision of ultrasonic velocity measurement in cortical bone: a validation on test materials. *IEEE Transactions on Ultrasonics, Ferroelectrics, and Frequency Control*, **51 (1)**, 71–79.

Cantrell, C. A., 2008: Technical note: Review of methods for linear least-squares fitting of data and application to atmospheric chemistry problems. *Atmospheric Chemistry and Physics*, **8 (17)**, 5477–5487.

Capon, J., 1969: High-resolution frequency-wavenumber spectrum analysis. *Proceedings of the IEEE*, **57 (8)**, 1408–1418.

Castaings, M., and B. Hosten, 2001: Lamb and SH waves generated and detected by air-coupled ultrasonic transducers in composite material plates. *NDT & E International*, **34 (4)**, 249–258.

Chang, L.-W., K.-H. Hsu, and P.-C. Li, 2009: Graphics processing unit-based high-frame-rate color Doppler ultrasound processing. *IEEE Transactions on Ultrasonics, Ferroelectrics, and Frequency Control*, **56 (9)**, 1856–1860.

Cobbold, R. S. C., 2006: *Foundations of biomedical ultrasound*. Oxford University Press.

Connell, I. R. O., K. M. Gilbert, M. A. Abou-Khousa, and R. S. Menon, 2015: MRI RF array decoupling method with magnetic wall distributed filters. *IEEE Transactions on Medical Imaging*, **34 (4)**, 825–835.

Currie, P. J., J. B. Seward, K.-L. Chan, D. A. Fyfe, D. J. Hagler, D. D. Mair, G. S. Reeder, R. A. Nishimura, and A. J. Tajik, 1985: Continuous wave Doppler determination of right ventricular pressure: a simultaneous Doppler-catheterization study in 127 patients. *Journal of the American College of Cardiology*, **6 (4)**, 750–756.

Daffertshofer, M., A. Gass, P. Ringleb, M. Sitzer, U. Sliwka, T. Els, O. Sedlaczek, W. J. Koroshetz, and M. G. Hennerici, 2005: Transcranial low-frequency ultrasound-mediated thrombolysis in brain ischemia. *Stroke*, **36 (7)**, 1441–1446.

Deng, J., R. Yates, A. G. Birkett, C. F. Ruff, A. D. Linney, W. R. Lees, M. A. Hanson, and C. H. Rodeck, 2001: Online motion-gated dynamic three-dimensional echocardiography in the fetus–preliminary results. *Ultrasound in Medicine & Biology*, **27 (1)**, 43–50.

Dong, X. N., and X. E. Guo, 2004: The dependence of transversely isotropic elasticity of human femoral cortical bone on porosity. *Journal of Biomechanics*, **37 (8)**, 1281–1287.

Foiret, J., J.-G. Minonzio, C. Chappard, M. Talmant, and P. Laugier, 2014: Combined estimation of thickness and velocities using ultrasound guided waves: a pioneering study on in vitro cortical bone samples. *IEEE Transactions on Ultrasonics, Ferroelectrics, and Frequency Control*, **61 (9)**, 1478–1488.

Fukao, S., T. Tsuda, T. Sato, S. Kato, K. Wakasugi, and T. Makihira, 1985: The MU radar with an active phased array system 1. Antenna and power amplifiers. *Radio Science*, **20 (6)**, 1155–1168.

Gao, W., C. Glorieux, and J. Thoen, 2003: Laser ultrasonic study of Lamb waves: determination of the thickness and velocities of a thin plate. *International Journal of Engineering Science*, **41 (2)**, 219–228.

Granke, M., Q. Grimal, A. Saïed, P. Nauleau, F. Peyrin, and P. Laugier, 2011: Change in porosity is the major determinant of the variation of cortical bone elasticity at the millimeter scale in aged women. *Bone*, **49 (5)**, 1020–1026.

Haardt, M., and J. A. Nossek, 1995: Unitary ESPRIT: How to obtain increased estimation accuracy with a reduced computational burden. *IEEE Transactions on Signal Processing*, **43 (5)**, 1232–1242.

Haïat, G., S. Naili, Q. Grimal, M. Talmant, C. Desceliers, and C. Soize, 2009: Influence of a gradient of material properties on ultrasonic wave propagation in cortical bone: Application to axial transmission. *The Journal of the Acoustical Society of America*, **125 (6)**, 4043–4052.

Haïat, G., F. Padilla, R. Barkmann, S. Kolta, C. Latremouille, C.-C. Glüer, and P. Laugier, 2005: In vitro speed of sound measurement at intact human femur specimens. *Ultrasound in Medicine & Biology*, **31 (7)**, 987 – 996.

Harb, M. S., and F. G. Yuan, 2015: A rapid, fully non-contact, hybrid system for generating Lamb wave dispersion curves. *Ultrasonics*, **61**, 62 – 70.

Harb, M. S., and F. G. Yuan, 2016: Non-contact ultrasonic technique for Lamb wave characterization in composite plates. *Ultrasonics*, **64**, 162–169.

Hasegawa, H., and H. Kanai, 2008: Simultaneous imaging of artery-wall strain and blood flow by high frame rate acquisition of RF signals. *IEEE Transactions on Ultrasonics, Ferroelectrics, and Frequency Control*, **55 (12)**, 2626–2639.

Hasegawa, H., and H. Kanai, 2012: High-frame-rate echocardiography with reduced sidelobe level. *IEEE Transactions on Ultrasonics, Ferroelectrics, and Frequency Control*, **59 (11)**, 2569–2575.

Hashimoto, T., K. Nishimura, and T. Sato, 2016: Adaptive sidelobe cancellation technique for atmospheric radars containing arrays with nonuniform gain. *IEICE Transactions on Communications*, **99 (12)**, 2583–2591.

Hein, I. A., and W. D. O'Brien, 1993: Current time-domain methods for assessing tissue motion by analysis from reflected ultrasound echoes-a review. *IEEE Transactions on Ultrasonics, Ferroelectrics, and Frequency Control*, **40 (2)**, 84–102.

Hoffmeister, B. K., C. I. Jones III, G. J. Caldwell, and S. C. Kaste, 2006: Ultrasonic characterization of cancellous bone using apparent integrated backscatter. *Physics in Medicine & Biology*, **51 (11)**, 2715–2727.

Hosokawa, A., and T. Otani, 1997: Ultrasonic wave propagation in bovine cancellous bone. *The Journal of the Acoustical Society of America*, **101 (1)**, 558–562.

Hu, S., E. A. Hoffman, and J. M. Reinhardt, 2001: Automatic lung segmentation for accurate quantitation of volumetric X-ray CT images. *IEEE Transactions on Medical Imaging*, **20 (6)**, 490–498.

Hu, W., Z. Zhao, Y. Wang, H. Zhang, and F. Lin, 2014: Noncontact accurate measurement of cardiopulmonary activity using a compact quadrature Doppler radar sensor. *IEEE Transactions on Biomedical Engineering*, **61 (3)**, 725–735.

Huang, Y., L. Ferro-Famil, and A. Reigber, 2012: Under-foliage object imaging using SAR tomography and polarimetric spectral estimators. *IEEE Transactions on Geoscience and Remote Sensing*, **50 (6)**, 2213–2225.

Illingworth, J., and J. Kittler, 1988: A survey of the Hough transform. *Computer Vision Graphics and Image Processing*, **44 (1)**, 87–116.

International Osteoporosis Foundation, 2002: Osteoporosis in the Workplace: the social, economic and human costs of osteoporosis on employees, employers and governments.

Ito, K., K. Yoshida, H. Maruyama, J. Mamou, and T. Yamaguchi, 2017: Acoustic impedance analysis with high-frequency ultrasound for identification of fatty acid species in the liver. *Ultrasound in Medicine & Biology*, **43 (3)**, 700–711.

Jensen, J. A., 1996: Field: A program for simulating ultrasound systems. *Medical and Biological Engineering and Computing*, **34 (Supplement 1)**, 351–353.

Jensen, J. A., 2001: A new estimator for vector velocity estimation. *IEEE Transactions on Ultrasonics, Ferroelectrics, and Frequency Control*, **48 (4)**, 886–894.

Jensen, J. A., and P. Munk, 1998: A new method for estimation of velocity vectors. *IEEE Transactions on Ultrasonics, Ferroelectrics, and Frequency Control*, **45 (3)**, 837–851.

Jensen, J. A., S. I. Nikolov, K. L. Gammelmark, and M. H. Pedersen, 2006: Synthetic aperture ultrasound imaging. *Ultrasonics*, **44 (Supplement)**, e5–e15.

Jensen, J. A., S. I. Nikolov, A. C. H. Yu, and D. Garcia, 2016a: Ultrasound vector flow imaging–part I: Sequential systems. *IEEE Transactions on Ultrasonics, Ferroelectrics, and Frequency Control*, **63 (11)**, 1704–1721.

Jensen, J. A., S. I. Nikolov, A. C. H. Yu, and D. Garcia, 2016b: Ultrasound vector flow imaging–part II: Parallel systems. *IEEE Transactions on Ultrasonics, Ferroelectrics, and Frequency Control*, **63 (11)**, 1722–1732.

Jensen, J. A., and N. B. Svendsen, 1992: Calculation of pressure fields from arbitrarily shaped, apodized, and excited ultrasound transducers. *IEEE Transactions on Ultrasonics, Ferroelectrics, and Frequency Control*, **39 (2)**, 262–267.

Kanis, J. A., O. Johnell, A. Oden, A. Dawson, C. De Laet, and B. Jonsson, 2001: Ten year probabilities of osteoporotic fractures according to BMD and diagnostic thresholds. *Osteoporosis International*, **12 (12)**, 989–995.

Kasai, C., K. Namekawa, A. Koyano, and R. Omoto, 1985: Real-time two-dimensional blood flow imaging using an autocorrelation technique. *IEEE Transactions on Sonics and Ultrasonics*, **32 (3)**, 458–464.

Kimura, T., H. Taki, T. Sakamoto, and T. Sato, 2009: Experimental study of high-range-resolution medical acoustic imaging for multiple target detection by frequency domain interferometry. *Japanese Journal of Applied Physics*, **48 (7S)**, 07GJ07.

Langton, C. M., S. B. Palmer, and R. W. Porter, 1984: The measurement of broadband ultrasonic attenuation in cancellous bone. *Engineering in Medicine*, **13 (2)**, 89–91.

Laugier, P., 2008: Instrumentation for in vivo ultrasonic characterization of bone strength. *IEEE Transactions on Ultrasonics, Ferroelectrics, and Frequency Control*, **55 (6)**, 1179–1196.

Laugier, P., and G. Haïat, 2011: *Bone quantitative ultrasound*. Springer.

Lenge, M., A. Ramalli, P. Tortoli, C. Cachard, and H. Liebgott, 2015: Plane-wave transverse oscillation for high-frame-rate 2-D vector flow imaging. *IEEE Transactions on Ultrasonics, Ferroelectrics, and Frequency Control*, **62 (12)**, 2126–2137.

Liu, C., T. Tang, F. Xu, D. Ta, M. Matsukawa, B. Hu, and W. Wang, 2015: Signal of interest selection standard for ultrasonic backscatter in cancellous bone evaluation. *Ultrasound in Medicine & Biology*, **41 (10)**, 2714–2721.

Lombardini, F., and F. Gini, 2005: Model order selection in multi-baseline interferometric radar systems. *EURASIP Journal on Advances in Signal Processing*, **2005 (20)**, 3206–3219.

Mano, I., K. Horii, S. Takai, T. Suzaki, H. Nagaoka, and T. Otani, 2006: Development of novel ultrasonic bone densitometry using acoustic parameters of cancellous bone for fast and slow waves. *Japanese Journal of Applied Physics*, **45 (5B)**, 4700–4702.

Marín, F., J. González-Macías, A. Díez-Pérez, S. Palma, and M. Delgado-Rodríguez, 2006: Relationship between bone quantitative ultrasound and fractures: A meta-analysis. *Journal of Bone and Mineral Research*, **21 (7)**, 1126–1135.

Mehdizadeh, S., A. Austeng, T. F. Johansen, and S. Holm, 2012: Minimum variance beamforming applied to ultrasound imaging with a partially shaded aperture. *IEEE Transactions on Ultrasonics, Ferroelectrics, and Frequency Control*, **59 (4)**, 683–693.

Minonzio, J.-G., M. Talmant, and P. Laugier, 2010: Guided wave phase velocity measurement using multi-emitter and multi-receiver arrays in the axial transmission configuration. *The Journal of the Acoustical Society of America*, **127 (5)**, 2913–2919.

Moghimirad, E., C. A. V. Hoyos, A. Mahloojifar, B. M. Asl, and J. A. Jensen, 2016: Synthetic aperture ultrasound Fourier beamformation using virtual sources. *IEEE Transactions on Ultrasonics, Ferroelectrics, and Frequency Control*, **63 (12)**, 2018–2030.

Nagatani, Y., K. Mizuno, T. Saeki, M. Matsukawa, T. Sakaguchi, and H. Hosoi, 2008: Numerical and experimental study on the wave attenuation in bone–FDTD simulation of ultrasound propagation in cancellous bone. *Ultrasonics*, **48 (6)**, 607–612.

Naili, S., M.-B. Vu, Q. Grimal, M. Talmant, C. Desceliers, C. Soize, and G. Haïat, 2010: Influence of viscoelastic and viscous absorption on ultrasonic wave propagation in cortical bone: Application to axial transmission. *The Journal of the Acoustical Society of America*, **127 (4)**, 2622–2634.

Nelson, A. M., J. J. Hoffman, C. C. Anderson, M. R. Holland, Y. Nagatani, K. Mizuno, M. Matsukawa, and J. G. Miller, 2011: Determining attenuation properties of interfering fast and slow ultrasonic waves in cancellous bone. *The Journal of the Acoustical Society of America*, **130 (4)**, 2233–2240.

Nguyen, V.-H., and S. Naili, 2012: Simulation of ultrasonic wave propagation in anisotropic poroelastic bone plate using hybrid spectral/finite element method. *International Journal for Numerical Methods in Biomedical Engineering*, **28 (8)**, 861–876.

Nguyen, V.-H., and S. Naili, 2013: Ultrasonic wave propagation in viscoelastic cortical bone plate coupled with fluids: A spectral finite element study. *Computer Methods in Biomechanics and Biomedical Engineering*, **16 (9)**, 963–974.

Nilsen, C.-I. C., and I. Hafizovic, 2009: Beamspace adaptive beamforming for ultrasound imaging. *IEEE Transactions on Ultrasonics, Ferroelectrics, and Frequency Control*, **56 (10)**, 2187–2197.

Núñez, I., R. K. Ing, C. Negreira, and M. Fink, 2000: Transfer and Green functions based on modal analysis for Lamb waves generation. *The Journal of the Acoustical Society of America*, **107 (5)**, 2370–2378.

O'Donnell, M., 1992: Coded excitation system for improving the penetration of real-time phased-array imaging systems. *IEEE Transactions on Ultrasonics, Ferroelectrics, and Frequency Control*, **39 (3)**, 341–351.

Okumura, S., V.-H. Nguyen, H. Taki, G. Haïat, S. Naili, and T. Sato, 2017: Phase velocity estimation technique based on adaptive beamforming for ultrasonic guided waves propagating along cortical long bones. *Japanese Journal of Applied Physics*, **56 (7S1)**, 07JF06.

Okumura, S., H. Taki, and T. Sato, 2015a: High-contrast and low-computational complexity medical ultrasound imaging using beamspace Capon method. *2015 37th Annual International Conference of the IEEE Engineering in Medicine and Biology Society (EMBC)*, 6334–6337.

Okumura, S., H. Taki, and T. Sato, 2015b: Stabilization techniques for high resolution ultrasound imaging using beamspace Capon method. *2015 IEEE International Conference on Acoustics, Speech and Signal Processing (ICASSP)*, 892–896.

Okumura, S., H. Taki, and T. Sato, 2016: Computational complexity reduction techniques for real-time and high-resolution medical ultrasound imaging using the beamspace Capon method. *Japanese Journal of Applied Physics*, **55 (7S1)**, 07KF07.

Otani, T., 2005: Quantitative estimation of bone density and bone quality using acoustic parameters of cancellous bone for fast and slow waves. *Japanese Journal of Applied Physics*, **44 (6B)**, 4578–4582.

Pothuaud, L., C. L. Benhamou, P. Porion, E. Lespessailles, R. Harba, and P. Levitz, 2000: Fractal dimension of trabecular bone projection texture is related to three-dimensional microarchitecture. *Journal of Bone and Mineral Research*, **15 (4)**, 691–699.

Rabin, O., J. M. Perez, J. Grimm, G. Wojtkiewicz, and R. Weissleder, 2006: An X-ray computed tomography imaging agent based on long-circulating bismuth sulphide nanoparticles. *Nature materials*, **5 (2)**, 118–122.

Raum, K., Q. Grimal, P. Varga, R. Barkmann, C. C. Glüer, and P. Laugier, 2014: Ultrasound to assess bone quality. *Current Osteoporosis Reports*, **12 (2)**, 154–162.

Riekkinen, O., M. A. Hakulinen, J. Töyräs, and J. S. Jurvelin, 2007: Spatial variation of acoustic properties is related with mechanical properties of trabecular bone. *Physics in Medicine & Biology*, **52 (23)**, 6961–6968.

Riggs, B. L., H. W. Wahner, W. L. Dunn, R. B. Mazess, K. P. Offord, and L. J. Melton III, 1981: Differential changes in bone mineral density of the appendicular and axial skeleton with aging: Relationship to spinal osteoporosis. *Journal of Clinical Investigation*, **67 (2)**, 328–335.

Rogers, W. P., 1995: Elastic property measurement using Rayleigh-Lamb waves. *Research in Nondestructive Evaluation*, **6 (4)**, 185–208.

Rose, J. L., 1999: Ultrasonic waves in solid media. Cambridge University Press.

Rossman, P., J. Zagzebski, C. Mesina, J. Sorenson, and R. Mazess, 1989: Comparison of speed of sound and ultrasound attenuation in the os calcis to bone density of the radius, femur and lumbar spine. *Clinical Physics and Physiological Measurement*, **10 (4)**, 353–360.

Roux, C., V. Roberjot, R. Porcher, S. Kolta, M. Dougados, and P. Laugier, 2001: Ultrasonic backscatter and transmission parameters at the os calcis in postmenopausal osteoporosis. *Journal of Bone and Mineral Research*, **16 (7)**, 1353–1362.

Roy, R., and T. Kailath, 1989: ESPRIT-estimation of signal parameters via rotational invariance techniques. *IEEE Transactions on Acoustics, Speech, and Signal Processing*, **37 (7)**, 984–995.

Saarnisaari, H., 1997: TLS-ESPRIT in a time delay estimation. *1997 IEEE 47th Vehicular Technology Conference. Technology in Motion*, Vol. 3, 1619–1623 vol.3.

Sakamoto, T., A. Matsuoka, and H. Yomo, 2016: Estimation of Doppler velocities from sub-Nyquist ultra-wideband radar measurements. *IEEE Sensors Journal*, **16 (23)**, 8557–8565.

Sale, M., P. Rizzo, and A. Marzani, 2011: Semi-analytical formulation for the guided waves-based reconstruction of elastic moduli. *Mechanical Systems and Signal Processing*, **25 (6)**, 2241–2256.

Sasso, M., G. Haïat, M. Talmant, P. Laugier, and S. Naili, 2008: Singular value decomposition-based wave extraction in axial transmission: application to cortical bone ultrasonic characterization [correspondence]. *IEEE Transactions on Ultrasonics, Ferroelectrics, and Frequency Control*, **55 (6)**, 1328–1332.

Sauer, S., L. Ferro-Famil, A. Reigber, and E. Pottier, 2007: Physical parameter extraction over urban areas using L-band POLSAR data and interferometric baseline diversity. *2007 IEEE International Geoscience and Remote Sensing Symposium*, 5045–5048.

Schoellhammer, C. M., S. Srinivasan, R. Barman, S. H. Mo, B. E. Polat, R. Langer, and D. Blankschtein, 2015: Applicability and safety of dual-frequency ultrasonic treatment for the transdermal delivery of drugs. *Journal of Controlled Release*, **202**, 93–100.

Schuit, S. C. E., M. van der Klift, A. E. A. M. Weel, C. E. D. H. de Laet, H. Burger, E. Seeman, A. Hofman, A. G. Uitterlinden, J. P. T. M. van Leeuwen, and H. A. P. Pols, 2004: Fracture incidence and association with bone mineral density in elderly men and women: the Rotterdam study. *Bone*, **34 (1)**, 195–202.

Shiina, T., K. R. Nightingale, M. L. Palmeri, T. J. Hall, J. C. Bamber, R. G. Barr, L. Castera, B. I. Choi, Y.-H. Chou, D. Cosgrove, C. F. Dietrich, H. Ding, D. Amy, A. Farrokh, G. Ferraioli, C. Filice, M. Friedrich-Rust, K. Nakashima, F. Schafer, I. Sporea, S. Suzuki, S. Wilson, and M. Kudo, 2015: WFUMB guidelines and recommendations for clinical use of ultrasound elastography: Part 1: basic principles and terminology. *Ultrasound in Medicine & Biology*, **41 (5)**, 1126–1147.

Simonelli, C., R. A. Adler, G. M. Blake, J. P. Caudill, A. Khan, E. Leib, M. Maricic, J. C. Prior, S. R. Eis, C. Rosen, and D. L. Kendler, 2008: Dual-energy X-ray absorptiometry technical issues: The 2007 ISCD official positions. *Journal of Clinical Densitometry*, **11 (1)**, 109 – 122.

Sirmacek, B., and C. Unsalan, 2010: Road network extraction using edge detection and spatial voting. *2010 20th International Conference on Pattern Recognition*, 3113–3116.

Suetoshi, R., D. Cretin, K. Chiba, and M. Osaki, 2016: Comparison between an axial transmission device and high resolution peripheral quantitative computed tomography–A clinical evaluation of ultrasound for the assessment of cortical bone quality. *The Journal of the Acoustical Society of America*, **140 (4)**, 3189–3189.

Sun, H., J. A. Fessler, D. C. Noll, and J.-F. Nielsen, 2016: Joint design of excitation k-space trajectory and RF pulse for small-tip 3D tailored excitation in MRI. *IEEE Transactions on Medical Imaging*, **35 (2)**, 468–479.

Synnevåg, J.-F., A. Austeng, and S. Holm, 2009: Benefits of minimum-variance beamforming in medical ultrasound imaging. *IEEE Transactions on Ultrasonics, Ferroelectrics, and Frequency Control*, **56 (9)**, 1868–1879.

Ta, D., W. Wang, K. Huang, Y. Wang, and L. H. Le, 2008: Analysis of frequency dependence of ultrasonic backscatter coefficient in cancellous bone. *The Journal of the Acoustical Society of America*, **124 (6)**, 4083–4090.

Takahashi, H., H. Hasegawa, and H. Kanai, 2014: Echo speckle imaging of blood particles with high-frame-rate echocardiography. *Japanese Journal of Applied Physics*, **53 (7S)**, 07KF08.

Takao, K., and N. Kikuma, 1987: An adaptive array utilizing an adaptive spatial averaging technique for multipath environments. *IEEE Transactions on Antennas and Propagation*, **35 (12)**, 1389–1396.

Taki, H., Y. Nagatani, M. Matsukawa, H. Kanai, and S.-I. Izumi, 2017: Fast decomposition of two ultrasound longitudinal waves in cancellous bone using a phase rotation parameter for bone quality assessment: Simulation study. *The Journal of the Acoustical Society of America*, **142 (4)**, 2322–2331.

Taki, H., Y. Nagatani, M. Matsukawa, K. Mizuno, and T. Sato, 2015a: Fast characterization of two ultrasound longitudinal waves in cancellous bone using an adaptive

beamforming technique. *The Journal of the Acoustical Society of America*, **137 (4)**, 1683–1692.

Taki, H., T. Sakamoto, M. Yamakawa, T. Shiina, T. Sato, K. Taki, and M. Kudo, 2013: Adaptive-beamformer with accurate intensity-estimation technique for high-range-resolution vascular ultrasound imaging. *2013 IEEE International Ultrasonics Symposium (IUS)*, 805–808.

Taki, H., K. Taki, T. Sakamoto, M. Yamakawa, T. Shiina, M. Kudo, and T. Sato, 2012: High range resolution ultrasonographic vascular imaging using frequency domain interferometry with the Capon method. *IEEE Transactions on Medical Imaging*, **31 (2)**, 417–429.

Taki, H., K. Taki, M. Yamakawa, T. Shiina, M. Kudo, and T. Sato, 2015b: High-range-resolution imaging using frequency domain interferometry with stabilization techniques for real-time vascular ultrasound. *Japanese Journal of Applied Physics*, **54 (7S1)**, 07HF05.

Taki, H., S. Tanimura, T. Sakamoto, T. Shiina, and T. Sato, 2015c: Accurate ultrasound imaging based on range point migration method for the depiction of fetal surface. *Journal of Medical Ultrasonics*, **42 (1)**, 51–58.

Talmant, M., S. Kolta, C. Roux, D. Haguenauer, I. Vedel, B. Cassou, E. Bossy, and P. Laugier, 2009: In vivo performance evaluation of bi-directional ultrasonic axial transmission for cortical bone assessment. *Ultrasound in Medicine & Biology*, **35 (6)**, 912–919.

Tanter, M., and M. Fink, 2014: Ultrafast imaging in biomedical ultrasound. *IEEE Transactions on Ultrasonics, Ferroelectrics, and Frequency Control*, **61 (1)**, 102–119.

Tran, T. N. H. T., L. H. Le, M. D. Sacchi, V.-H. Nguyen, and E. H. M. Lou, 2014a: Multichannel filtering and reconstruction of ultrasonic guided wave fields using time intercept-slowness transform. *The Journal of the Acoustical Society of America*, **136 (1)**, 248–259.

Tran, T. N. H. T., K.-C. T. Nguyen, M. D. Sacchi, and L. H. Le, 2014b: Imaging ultrasonic dispersive guided wave energy in long bones using linear Radon transform. *Ultrasound in Medicine & Biology*, **40 (11)**, 2715–2727.

Udesen, J., and J. A. Jensen, 2006: Investigation of transverse oscillation method. *IEEE Transactions on Ultrasonics, Ferroelectrics, and Frequency Control*, **53 (5)**, 959–971.

Vallet, Q., N. Bochud, C. Chappard, P. Laugier, and J.-G. Minonzio, 2016: In vivo characterization of cortical bone using guided waves measured by axial transmission. *IEEE Transactions on Ultrasonics, Ferroelectrics, and Frequency Control*, **63 (9)**, 1361–1371.

Van Trees, H. L., 2002: *Optimum array processing: Part IV of detection, estimation and modulation theory*. Wiley-Interscience.

Viktorov, I. A., 1967: *Rayleigh and Lamb waves: physical theory and applications*. Plenum press.

Wang, Z., J. Li, and R. Wu, 2005: Time-delay- and time-reversal-based robust capon beamformers for ultrasound imaging. *IEEE Transactions on Medical Imaging*, **24 (10)**, 1308–1322.

Wax, M., 1991: Detection and localization of multiple sources via the stochastic signals model. *IEEE Transactions on Signal Processing*, **39 (11)**, 2450–2456.

Wax, M., and T. Kailath, 1985: Detection of signals by information theoretic criteria. *IEEE Transactions on Acoustics, Speech, and Signal Processing*, **33 (2)**, 387–392.

Wear, K. A., 2008: Ultrasonic scattering from cancellous bone: A review. *IEEE Transactions on Ultrasonics, Ferroelectrics, and Frequency Control*, **55 (7)**, 1432–1441.

Wear, K. A., 2014: Time-domain separation of interfering waves in cancellous bone using bandlimited deconvolution: Simulation and phantom study. *The Journal of the Acoustical Society of America*, **135 (4)**, 2102–2112.

Xu, K., J.-G. Minonzio, D. Ta, B. Hu, W. Wang, and P. Laugier, 2016a: Sparse SVD method for high-resolution extraction of the dispersion curves of ultrasonic guided waves. *IEEE Transactions on Ultrasonics, Ferroelectrics, and Frequency Control*, **63 (10)**, 1514–1524.

Xu, K., D. Ta, D. Cassereau, B. Hu, W. Wang, P. Laugier, and J.-G. Minonzio, 2016b: Multichannel processing for dispersion curves extraction of ultrasonic axial-transmission signals: Comparisons and case studies. *The Journal of the Acoustical Society of America*, **140 (3)**, 1758–1770.

Xu, K., D. Ta, P. Moilanen, and W. Wang, 2012: Mode separation of Lamb waves based on dispersion compensation method. *The Journal of the Acoustical Society of America*, **131 (4)**, 2714–2722.

Yamaguchi, T., H. Hachiya, K. Kato, H. Fukuda, and M. Ebara, 2000: Extraction of quantitative three-dimensional information from ultrasonic volumetric images of cirrhotic liver. *Japanese Journal of Applied Physics*, **39 (5B)**, 3266–3269.

Yapura, C. L., and V. K. Kinra, 1995: Guided waves in a fluid-solid bilayer. *Wave Motion*, **21 (1)**, 35–46.

Yeung, F., S. F. Levinson, and K. J. Parker, 1998: Multilevel and motion model-based ultrasonic speckle tracking algorithms. *Ultrasound in Medicine & Biology*, **24 (3)**, 427–441.

Yoshida, K., Z. Deng, K. Ito, J. Mamou, H. Maruyama, H. Hachiya, and T. Yamaguchi, 2016: Speed of sound, attenuation, and acoustic impedance of hepatic lobule in diseased rat liver observed by scanning acoustic microscopy with 250 MHz. *The Journal of the Acoustical Society of America*, **140 (4)**, 3138–3138.

Major publications

Refereed Journal Papers

1. S. Okumura, H. Taki, and T. Sato, "Computational complexity reduction techniques for real-time and high-resolution medical ultrasound imaging using the beam-space Capon method," *Japanese Journal of Applied Physics*, **55**(**7S1**), 07KF07, 2016

2. S. Okumura, V.-H. Nguyen, H. Taki, G. Haïat, S. Naili, T. Sato, "Phase velocity estimation technique based on adaptive beamforming for ultrasonic guided waves propagating along cortical long bones," *Japanese Journal of Applied Physics*, **56**(**7S1**), 07JF06, 2017

Refereed International Conferences

1. S. Okumura, H. Taki, and T. Sato, "Stabilization techniques for high resolution ultrasound imaging using beamspace Capon method," IEEE International Conference on Acoustics, Speech and Signal Processing (ICASSP), South Brisbane, QLD, Australia, 2015.

2. S. Okumura, H. Taki and T. Sato, "High-contrast and low-computational complexity medical ultrasound imaging using beamspace Capon method," 37th Annual International Conference of the IEEE Engineering in Medicine and Biology Society (EMBC), Milan, Italy, 2015.

3. S. Okumura, H. Taki and T. Sato, "Computational complexity reduction technique for adaptive high-contrast medical ultrasound imaging using BS Capon method," 2nd International Conference on Ultrasonic-Based Applications: from Analysis to Synthesis, Caparica, Portugal, 2016.

4. S. Okumura, V.-H. Nguyen, H. Taki, and T. Sato, "Accurate characterization of ultrasonic guided waves propagating in cortical bone acquired by a single transmit-

terreceiver pair using adaptive signal processing," 6th International Conference on the Development of Biomedical Engineering, Ho Chi Minh City, Vietnam, 2016.

5. S. Okumura, Takuro Sato, T. Sakamoto, and T. Sato, "Technique of tracking multiple pedestrians using monostatic ultra-wideband Doppler radar with adaptive Doppler spectrum estimation," International Symposium on Antennas and Propagation, Okinawa, Japan, 2016.

6. S. Okumura, V.-H. Nguyen, H. Taki and T. Sato, "Efficient phase velocity estimation of ultrasonic guided wave propagating in cortical bone using adaptive beamforming technique," Symposium on UltraSonic Electronics, Busan, South Korea, 2016.

7. S. Okumura, V.-H. Nguyen, H. Taki and T. Sato, "A fast signal processing technique for characterizing Lamb wave propagation in viscoelastic cortical long bones using one transmitter and two receivers," 5th Joint Meeting of the Acoustical Society of America and Acoustical Society of Japan, Honolulu, HI, USA, 2016.

8. S. Okumura, A. Ueshina, T. Sakamoto, T. Sato, "Multiple target imaging using a single monostatic ultra-wideband Doppler radar based on time domain adaptive signal processing," URSI General Assembly and Scientific Symposium (GASS), Montreal, Canada, 2017.

9. S. Okumura, V.-H. Nguyen, H. Taki and T. Sato, "Low-cost Lamb wave characterization technique using one transmitter and two receivers: an experimental study," 7th European Symposium on Ultrasonic Characterization of Bone (ESUCB), Bad Staffelstein, Germany, 2017.

10. S. Okumura, H. Taki, V.-H. Nguyen and T. Sato, "Estimation of phase velocity and attenuation of visco-elastic plate with adaptive beamforming technique for cortical bone assessment," IEEE International Ultrasonics Symposium (IUS), Washington, DC, USA, 2017.

Related Journal Papers

1. T. Sakamoto, S. Okumura, R. Imanishi, H. Taki, T. Sato, M. Yoshioka, K. Inoue, T. Fukuda, and H. Sakai, "Remote heartbeat monitoring from human soles using 60-GHz ultra-wideband radar," *IEICE Electronics Express*, **12**(**21**), 20150786, 2015.

2. S. Okumura, T. Sakamoto, T. Sato, M. Yoshioka, K. Inoue, T. Fukuda, and H. Sakai, "Comparison of clutter rejection techniques for measurement of small displacements of body surface using radar," *Electronics Letters*, **52**(**19**), 1635–1637, 2016.

3. M. Anabuki, S. Okumura, T. Sakamoto, K. Saho, T. Sato, M. Yoshioka, K. Inoue, T. Fukuda, and H. Sakai, "Ultra-wideband radar imaging using adaptive array and Doppler separation," *IEEE Transactions on Aerospace and Electronic Systems*, **53**(**1**), 190–200, 2017.